Generation and Reconstruction of Propagating Quantum Microwaves

Dissertation

Ling Zhong

August 2015

Advisor: Prof. Dr. Rudolf Gross

Fakultät für Physik

Technische Universität München

TECHNISCHE UNIVERSITÄT MÜNCHEN

Fakultät für Physik
Lehrstuhl E23 für Technische Physik

Walther-Meißner-Institut für Tieftemperaturforschung
der Bayerischen Akademie der Wissenschaften

Generation and Reconstruction of Propagating Quantum Microwaves

Ling Zhong

Vollständiger Abdruck der von der Fakultät für Physik der Technischen Universität München zur Erlangung des akademischen Grades eines

Doktors der Naturwissenschaften

genehmigten Dissertation.

Vorsitzender:		Univ.-Prof. Dr. Alessio Zaccone
Prüfer der Dissertation:	1.	Univ.-Prof. Dr. Rudolf Gross
	2.	Univ.-Prof. Jonathan J. Finley, Ph.D.

Die Dissertation wurde am 3. August 2015 bei der
Technischen Universität München eingereicht und durch
die Fakultät für Physik am 17. August 2015 angenommen.

Abstract

Propagating quantum microwaves are a key ingredient for quantum communication. A particular form of such quantum microwaves is squeezed states. In this work, we investigate squeezed states generated by Josephson parametric amplifiers (JPAs) with a dual-path setup. Squeezed coherent states can be generated by sending coherent states into a JPA. Alternatively, displacement operations can be performed using a directional coupler. We discuss our results in the context of remote state preparation and quantum teleportation.

Kurzzusammenfassung

Propagierende Quantenmikrowellen sind Schlüsselbausteine für die Quantenkommunikation. Wir untersuchen gequetschte Zustände, die mit Josephson parametrischen Verstärkern (JPA) erzeugt werden, mit der Zweipfadmethode zur Zustandsrekonstruktion. Gequetschte kohärente Zustände können sowohl durch Einsenden eines kohärenten Signals in den JPA, als auch durch Anwenden einer Verschiebungsoperation auf einen gequestschten Vakuumzustand, generiert werden. Wir diskutieren unsere Ergebnisse im Rahmen von ferngesteuerter Zustandspräparation und Quantenteleportation.

Contents

1 Introduction **1**

2 Microwave signals and circuit QED systems **7**
2.1 Classical representation of electromagnetic fields 7
2.2 Quantum representation of electromagnetic fields 8
2.2.1 Density operator 8
2.2.2 P-representation 9
2.2.3 Wigner function 9
2.3 Displacement 11
2.4 Squeezing 14
2.4.1 Squeezed vacuum states 15
2.4.2 Squeezed coherent states 16
2.5 Microwave transmission line 18
2.6 Microwave resonator 19
2.7 Josephson junction 21
2.8 Dc-SQUID 22
2.9 Flux-driven JPA 23

3 Quantum communication with propagating microwaves **25**
3.1 Two-mode squeezed vacuum state 25
3.2 Correlation functions 27
3.2.1 Dual-path method 27
3.2.2 Correlation functions of two-mode squeezed states 30
3.3 Quantum teleportation 31
3.4 Remote state preparation 33

4 Experimental techniques **43**
4.1 Cryogenic setups 43
4.1.1 Input lines 45
4.1.2 Sample preparation 48
4.1.3 Millikelvin stage 50
4.1.4 Output lines 51
4.1.5 DC lines 53
4.2 Room temperature setups 53
4.2.1 Dual-path receiver 54

4.2.2 IQ cross-correlation detector . . . 57
4.2.3 Acqiris card based data acquisition and processing . . . 58
4.3 Phase stabilization . . . 59

5 JPA characterization 63
5.1 Q600 JPA . . . 63
5.1.1 Flux dependence of the resonance frequency . . . 63
5.1.2 Multi-wave mixing . . . 69
5.2 Q200 JPA . . . 70
5.2.1 Flux dependence of the resonance frequency . . . 70
5.2.2 Non-degenerate gain . . . 71
5.2.3 1 dB-compression point . . . 73
5.2.4 Noise properties in the non-degenerate mode . . . 74

6 Displacement 77
6.1 Squeezed coherent states (Q300 JPA) . . . 78
6.1.1 Photon number conversion factor (PNCF) calibration . . . 78
6.1.2 Measurement sequence . . . 79
6.1.3 Displacement of squeezed coherent states . . . 80
6.1.4 Photon numbers of squeezed coherent states . . . 82
6.1.5 State statistics . . . 83
6.2 Coherent squeezed states (Q200 JPA) . . . 84
6.2.1 PNCF calibration . . . 84
6.2.2 Squeezed vacuum states . . . 85
6.2.3 Displaced squeezed vacuum states . . . 87
6.2.4 Squeezing versus displacement . . . 89
6.3 Coherent squeezed states (new JPA) . . . 92

7 Summary and outlook 97

A FPGA based dual-path setup 101

B Acqiris card based dual-path receiver 103

C Gaussianity and higher order cumulants 105

D Dual-path state reconstruction 107

E Negativity 109

Bibliography 111

List of publications 121

Acknowledgement 123

List of Figures

2.1 Wigner function of a vacuum state, a coherent state and a squeezed state. . . . 12
2.2 Directional coupler 13
2.3 Squeezed coherent states and coherent squeezed states 16
2.4 CPW resonator 18
2.5 Josephson junction 21
2.6 Dc-SQUID 22
2.7 Flux driven JPA 24

3.1 Schematic of setups for the dual-path method and reference state method 27
3.2 Schematic of a quantum teleportation protocol with propagating microwaves 32
3.3 Schematic of a setup for remote state preparation 34
3.4 Effect of different parameters on remote state preparation 39
3.5 Effect of the EPR-JPAs angle error on remote state preparation 40
3.6 Effect of setup losses on remote state preparation 41

4.1 Photograph of the cryogenic setup 44
4.2 Schematic of the cryogenic setup 46
4.3 Input lines 47
4.4 Sample layout 48
4.5 Photograph of Q200 JPA in a side-mounted sample box 49
4.6 Photograph of Q600 JPA in a top-mounted sample box 49
4.7 Sample rod 50
4.8 NbTi/NbTi superconducting cable losses 52
4.9 DC wires 53
4.10 Schematics of the room temperature setup for Q600 JPA 54
4.11 Schematics of the room temperature setup for Q200 JPA 55
4.12 A simplified schematic of the dual-path receiver 56
4.13 Schematic of an IQ mixer 57
4.14 Sketch of data acquisition and processing of the Acqiris card based dual-path setup for one cycle 60
4.15 Phase drifts of SGS source 61

5.1 JPA reflection measurement scheme with a VNA 64

5.2 Reflection spectra of Q600 JPA as a function of the applied external flux with pump off 64
5.3 Color plots of the two-dimensional potential for a dc-SQUID 66
5.4 The SQUID potential versus $(\varphi_1 + \varphi_2)/2\pi$ with $\beta = 0.5$, and $(\varphi_1 - \varphi_2)/2 = 0$ 68
5.5 Fitting results of resonance frequency versus external magnetic flux for Q600 JPA 69
5.6 Power spectra at different pump powers for Q600 JPA 70
5.7 Flux dependence of the resonance frequency for Q200 JPA 71
5.8 Signal and idler gains for Q200 JPA 71
5.9 Reflection of Q200 JPA with different pump powers and pump frequencies 72
5.10 1-dB compression point for Q200 JPA 73
5.11 Noise properties of Q200 JPA in non-degenerate mode 74

6.1 PNCF measurements for Q300 JPA 80
6.2 Time trace of squeezed coherent states measurements 81
6.3 Experimental displacement for squeezed vacuum states, coherent states and squeezed coherent states 82
6.4 Experimental photon numbers for squeezed vacuum states, coherent states and squeezed coherent states 83
6.5 PNCF measurements for Q200 JPA 84
6.6 Experimental squeezed vacuum states 86
6.7 Experimental coherent squeezed states 88
6.8 Comparison between squeezed coherent states and coherent squeezed states including thermal photons 89
6.9 Simulations of coherent squeezed states and coherent states as a function of displacement in the presence of phase noise 90
6.10 Squeezing level versus displacement for experimental coherent squeezed states and coherent states 92
6.11 Squeezing level versus displacement for experimental coherent squeezed states and coherent states with different scaling factors y for PNCFs of chain 2 93
6.12 PNCF measurements for new JPA 94
6.13 Experimental squeezing level and photon number as a function of the signal gain for new JPA sample 95
6.14 Squeezing level of experimental coherent squeezed states and coherent states as a function of displacement for the new JPA sample 95
6.15 Negativity kernel of the hybrid output state as a function of displacement based on dual-path method for the new JPA sample 96

A.1 Simplified schematic of the dual-path setup for measurements with Q300 JPA 101

B.1 Schematic of the Acqiris card based dual-path receiver for measurements with Q200 JPA 104

List of Tables

3.1 Comparison of the squeezing level between the hybrid ring input states and the final output states for remote state preparation 38

4.1 Summary of different types of SMA connectors on NbTi/NbTi cables 52

6.1 Number of noise photons in the two detection chains calculated from PNCF fitting and dual-path reconstruction for Q300 JPA 79
6.2 Comparison between squeezed coherent states and squeezed vacuum states 84
6.3 Number of noise photons in the two detection chains calculated from PNCF fitting and dual-path reconstruction for Q200 JPA 85
6.4 Simulations of the squeezing level (dB) of coherent squeezed states and coherent states versus displacement in the presence of phase noise 91

Chapter 1

Introduction

Over the past decades, modern computers and telecommunication networks, which can be described on the basis of classical physics, have been rapidly developing, and the information processing, transfer and storage efficiency have been continuously improving. As the size of computer components scales down to the atomic level, scientists and engineers were thinking about using resources of quantum mechanics, such as superposition of states and entanglement, for the realization of quantum computation and communication systems. The discipline which deals with computation and communication based on quantum mechanics is quantum information science. Quantum computers consist quantum two-level systems, which for example can be realized by atoms and molecules, for data storage and computational tasks. In quantum communication systems information usually is transferred by individual photons.

All operations in a classical computer are based on binary bits, which can be in either of two states. The fundamental unit of a quantum computer, a quantum bit or qubit, can be in any superposition state $\alpha|0\rangle + \beta|1\rangle$ of the eigenstates, $|0\rangle$ and $|1\rangle$, where $|\alpha|^2$ and $|\beta|^2$ are the probability of the qubit in state $|0\rangle$ and $|1\rangle$, respectively. This feature enables a quantum computer to evaluate certain functions with all the possible input values simultaneously. In 1985, D. Deutsch termed this effect "quantum parallelism" [1]. Later on, quantum parallelism found its applications in the Deutsch-Jozsa algorithm [2], the Shor algorithm [3], etc., where quantum computers can provide exponential speedup of certain problems.

Since the 1960s, scientists started to apply fundamental principles of quantum mechanics to communication systems [4, 5]. The basic problem to solve in quantum communication is to transfer an arbitrary quantum state from one location to another. Traditionally, the sender is called Alice and the receiver Bob. There are several ways to transfer a quantum state. One possible solution is to map a qubit state in Alice's station to a nonclassical photon state, and transmit the photon to Bob, where the information stored in the photon is retrieved by a qubit in Bob's station [6, 7]. With this method, the quantum information is transferred directly from Alice to Bob. However, if the communication channel between Alice and Bob is too lossy for the quantum state to be transferred, this method is not a good option.

When the superposition principle applies to correlated states of multiple subsystems, entanglement could be observed. This is what Einstein called "spooky action at a distance". As one of the most counterintuitive characteristics in quantum mechanics, entanglement makes another intriguing form of quantum communication, quantum teleportation, possible. Quantum teleportation, which was first proposed by C. H. Bennett et al. in 1993 [8], uses a classical channel and a quantum channel. The classical channel is for communication of classical information (two classical bits), whereas the quantum channel is for distributing entanglement in the form of an Einstein-Podolsky-Rosen (EPR) pair [9]. An EPR pair is distributed to Alice and Bob. The state to be teleported is unknown to both Alice and Bob. In Alice's station, a Bell state measurement is performed on the state to be teleported and half of the EPR pair. This measurement destroys the state to be teleported, and generates two classical bits. Then, Alice communicates the measurement results, two bits of information, to Bob via the classical channel. This classical communication is also called feed-forward. Based on the classical information received by Bob, he applies a linear transformation on his half of the EPR pair. The state after linear transformation is guaranteed to be identical to the original state to be teleported.

The first experimental realization of quantum teleportation [10, 11] was achieved in 1997 by making use of the photon polarization. These experiments have shown that even with experimental errors the teleportation fidelity, which characterizes the similarity between the input and output states, has exceeded the classical threshold. Besides quantum teleportation of discrete variables, the scheme for continuous variables has been studied theoretically [12, 13] and experimentally. For continuous variables, information is embedded into the position and momentum, the two quadratures of a propagating electromagnetic field. In 1998, A. Furusawa et al. [14] have demonstrated quantum teleportation of optical coherent states with active feed-forward. In 2011, nonclassical wave packets of optical photons have been successfully teleported [15]. In this experiment, the fragile nonclassical properties of the input state was preserved after teleportation. Based on the achieved progress, quantum teleportation in the optical domain has also been demonstrated in free space [16–18], and it is presently being developed towards satellite based quantum teleportation. Here the question arises about the present experimental status of quantum teleportation in the microwave regime?

Since the first demonstration of strong coupling between microwave photons and qubits based on superconducting circuits [19, 20], circuit Quantum ElectroDynamics (QED) systems are considered to be a promising physical realization of the basic elements required for quantum information processing. In contrast to the optical domain, where natural atoms or molecules are supposed to be the fundamental units in a quantum computer, in the microwave domain macroscopic superconducting circuits act as qubits. Since these superconducting qubits can be considered as artificial atoms, there is a lot of flexibility to design the relevant parameters. Also, strong and even ultrastrong coupling [21] between superconducting qubits and microwave photons are relatively easy to achieve. At the same time, these superconducting qubits have transitions frequencies of the order of 10 GHz corresponding to about 500 mK and interact strongly with the environment. Therefore, cryogenic temperatures are needed to bring the superconducting circuits into a regime where quantum effects dominate the thermal noise from environments. First, the environment temperature should be well below the critical temperature of the superconducting materials to suppress the effect of quasiparticles. Second the energy of thermal excitations should be well below the qubit transition energy and the excitation energy of resonators.

Due to the low single microwave photon energy, which is typically five orders of magnitude lower than that of optical photons, single microwave photon detectors do not exist yet. So far the measurement of such signals make use of signal averaging techniques which are based on amplification of the weak microwave signals. For a long time, phase-insensitive High Electron Mobility Transistor (HMET) amplifiers have been used for this purpose. They have a broad operation bandwidth and high gain, but 5-20 noise photons [22, 23] are added to the input signal. Recently, with the application of Josephson Parametric Amplifiers (JPAs) [24–34], the number of added noise photons has been significantly reduced. In the phase-insensitive or non-degenerate operation mode, the JPA noise temperatures approach the standard quantum limit set by the Heisenberg uncertainty relation [31–33, 35–37]. In phase-sensitive or degenerate operation mode, JPAs can amplify a signal quadrature with a noise temperature even below the standard quantum limit [22, 32]. With JPAs as low noise pre-amplifiers followed by HEMT amplifiers, quantum teleportation in the microwave domain with superconducting circuits has been realized [38] in 2013. In this experiment, a qubit state has been teleported to another qubit which was 6 mm away.

Operating JPAs in the phase-sensitive mode, one quadrature can be amplified while the conjugate quadrature is squeezed. If the quadrature fluctuations are squeezed below the vacuum fluctuations, a single mode squeezed state is generated [32,34,39]. Sending squeezed states into a beam splitter, the state at the beam splitter outputs is a two-mode squeezed state [39, 40], which can be utilized as an EPR pair in a quantum teleportation protocol based on continuous variables. With our current progress of dual-path state reconstruction method [40–43], JPA-based low noise amplification [32], and path entanglement [39], the goal of this work is quantum teleportation of propagating microwave signals.

The quantum teleportation protocol contains several building blocks: EPR pair generation, Bell state measurement, classical communication and linear transformation of an arbitrary quantum state. The linear transformation for continuous variables corresponds to a displacement operation, which is the main topic of this thesis. An asymmetric beam splitter, whose transmissivity is close to unity, with a coherent state at the second input performs a displacement operation on the state at the first input. A JPA, operating in the phase-sensitive mode, applies a squeeze operator to the input state. By sending a coherent state into a JPA, effectively a displacement operator followed by a squeeze operator are applied to a vacuum state. By sending a squeezed vacuum state into an asymmetric beam splitter, effectively a squeeze operator followed by a displacement operator is applied to a vacuum state. In this way, we can study the effect of the displacement operator and squeeze operator applied to a vacuum state. Due to the fact that these two operators do not commute, different sequences lead to different states.

The teleportation of an unknown qubit state requires two classical bits of information (two bits) as the classical resource and an EPR pair, which is called one "ebit" as the quantum resource. There is no trade-off between the classical and quantum resources. When the state to be transferred is known to the sender, this case is called remote state preparation. In the extreme case without entanglement, Alice can communicate to Bob an infinite number of classical bits, which fully describe the state, and Bob prepares the state locally. In the other extreme case, the minimal amount of classical bits required is one, which is set by causality. Between these two extreme cases, there is a trade-off among classical and quantum resources. Quantum teleportation is a special case of remote state preparation with two classical bits and one ebit.

The displacement operation, which has been studied in this work, is also an important building block in remote state preparation. We develop a protocol to remotely prepare a squeezed state. Alice and Bob share an EPR pair in the form of a two-mode squeezed state. Alice performs a projective measurement on her half of the EPR pair. Then, Alice communicates the result, which is one bit, to Bob. Bob performs a linear transformation on his half of the EPR pair based on Alice's result. The final state obtained by Bob is a squeezed state.

This thesis is structured as follows. In Chapter 2, we introduce the basics of quantum microwave signals and circuit QED systems. This includes classical and quantum representations of electromagnetic fields. We discuss the displacement operators in the context of coherent states, and the squeeze operators in the context of squeezed states. Important building blocks of circuit QED systems, such as microwave resonators, Josephson junctions, dc-Superconducting QUantum Interference Devices (dc-SQUIDs) and flux-driven JPAs are discussed. In Chapter 3, the treatment of quantum communication with propagating microwaves is presented. We focus on two-mode squeezed vacuum states, correlation functions, and we also describe quantum teleportation and remote state preparation protocols with propagating microwave signals in more detail. In Chapter 4, experimental techniques, including cryogenic and room temperature setups, data acquisition and phase stabilization methods, are presented. In Chapter 5, the JPA characterization including gain measurements, 1 dB-compression point measurements, etc. is presented. We also explain in detail a theoretical method to describe the flux-dependence of the JPA resonance frequency. In Chapter 6, we apply displacement and squeeze operators to vacuum states in different sequences, and reconstruct the states with the dual-path reconstruction method. We discuss the rich physics behind the squeezed coherent states and coherent squeezed states. In Chapter 7, we conclude the work and give a brief outlook.

Chapter 2

Microwave signals and circuit QED systems

In this chapter, the basics of circuit Quantum ElectroDynamics (QED) are introduced. We start with classical and quantum representations of electromagnetic fields. Then displacement and squeeze operations are introduced. Also, the basic building blocks for circuit QED systems, including microwave transmission lines, resonators, Josephson junctions and dc-SQUIDs, are discussed. Finally, the working principle of a Josephson Parametric Amplifier (JPA) is introduced.

2.1 Classical representation of electromagnetic fields

Maxwell's equations provide the basis for the classical description of electromagnetic waves. A monochromatic wave in a linear medium propagating along direction $\vec{r}$ can be presented as

$$S\left(\vec{r}, t\right) = A\mathrm{e}^{\mathrm{i}\left(\omega t - \vec{k}\vec{r}\right)} \,. \tag{2.1}$$

Here, ω is the angular frequency, and $\vec{k}$ is the wavevector. For a fixed $\vec{r}$, Eq. (2.1) can be written as

$$\begin{aligned} S(t) &= A\mathrm{e}^{\mathrm{i}(\omega t + \phi)} \\ &= [\underbrace{A\cos\left(\phi\right)}_{I} + \mathrm{i}\underbrace{A\sin\left(\phi\right)}_{Q}]\mathrm{e}^{\mathrm{i}\omega t} \\ &= \left[I + \mathrm{i}Q\right]\mathrm{e}^{\mathrm{i}\omega t}, \end{aligned} \tag{2.2}$$

where I and Q are called in-phase and out-of-phase components of the signal, respectively, and ϕ is the phase of the signal. In microwave engineering, the notations I and Q are used. In a quantum mechanical treatment, the quadratures $\hat{p}$ and $\hat{q}$ are used.

In general, microwave signals have frequencies $f = \omega/2\pi$ between 300 MHz and 300 GHz [44]. Different frequency ranges correspond to different applications. For example, 2.45 GHz microwave radiation is used for heating in microwave ovens. GPS satellites broadcast on two carrier frequencies: 1575.42 MHz and 1227.60 MHz. WiFi refers to 2.4 GHz and 5 GHz signals. In our case, we are interested in signals in the frequency range from 4 to 20 GHz propagating in free space, transmission lines or CoPlanar Waveguides (CPW).

2.2 Quantum representation of electromagnetic fields

2.2.1 Density operator

The classical description of electromagnetic fields does not include the Heisenberg uncertainty relation. To fully describe electromagnetic fields, one needs to use quantum statistical method. Electromagnetic fields typically have a certain bandwidth in frequency, corresponding to an infinite number of frequency modes. However, each mode requires an independent Hilbert space, and a distribution function to describe the probability distribution of all the possible values of a certain property of the field. In the following, we restrict our discussion to single mode fields. The product of probability distribution functions of individual modes represents the entire field. A quantum mechanical state, both for pure states and mixed states, for discrete variables and continuous variables, is completely described by its density operator. It is defined as

$$\hat{\rho} = \sum_{\mathrm{j}} P_{\mathrm{j}} |\Psi_{\mathrm{j}}\rangle\langle\Psi_{\mathrm{j}}| \,, \tag{2.3}$$

where $P_{\mathrm{j}} \geqslant 0$, and $\sum_{\mathrm{j}} P_{\mathrm{j}} = 1$. P_{j} indicates the probability of finding the system in state $|\Psi_{\mathrm{j}}\rangle$. The states $|\Psi_{\mathrm{j}}\rangle$ are normalized, and do not have to be orthogonal. Referring the density operator to a basis $\{|\phi_{\mathrm{n}}\rangle\}$, the density matrix,

$$\rho_{\mathrm{nm}} = \sum_{\mathrm{j}} P_{\mathrm{j}} \langle\phi_{\mathrm{n}}|\Psi_{\mathrm{j}}\rangle\langle\Psi_{\mathrm{j}}|\phi_{\mathrm{m}}\rangle \,, \tag{2.4}$$

is obtained. The expectation value of an operator $\hat{O}$ is given by

$$\langle \hat{O} \rangle = \sum_{\mathrm{j}} P_{\mathrm{j}} \langle \Psi_{\mathrm{j}} | \hat{O} | \Psi_{\mathrm{j}} \rangle = \mathrm{Tr}(\hat{O}\hat{\rho}) \,. \tag{2.5}$$

2.2.2 P-representation

Depending on the chosen basis, a density operator can have different representations. For example, the P-representation is obtained by expanding the density operator in terms of coherent states. We introduce $\hat{a}$ and $\hat{a}^\dagger$ as annihilation and creation operators, obeying the bosonic commutator relation $\left[\hat{a}, \hat{a}^\dagger\right] = 1$. The wave function of a coherent state is written as $|\alpha\rangle = \exp\left(\alpha\hat{a}^\dagger - \alpha^*\hat{a}\right)|0\rangle = \hat{D}(\alpha)|0\rangle$, where $|0\rangle$ is the vacuum state, and $\hat{D}(\alpha)$ is the so-called displacement operator with a complex amplitude, α. Coherent states $|\alpha\rangle$ form a complete set of non-orthogonal states. Therefore, the diagonal expansion of the density operator in coherent states becomes

$$\hat{\rho} = \int P(\alpha)|\alpha\rangle\langle\alpha|\mathrm{d}^2\alpha \,. \tag{2.6}$$

$P(\alpha)$ is called Glauber-Sudarshan P-representation [45, 46]. Since the projection operation $|\alpha\rangle\langle\alpha|$ is onto non-orthogonal states, $P(\alpha)$ is not a real probability distribution for the system. Therefore, it is called a quasi-probability distribution.

A normally ordered characteristic function $\xi_{\mathrm{N}}(\eta) = \mathrm{Tr}\{\hat{\rho}\mathrm{e}^{\eta\hat{a}^\dagger}\mathrm{e}^{-\eta^*\hat{a}}\}$ is often used to evaluate the P-function. $P(\alpha)$ is the Fourier transform of $\xi_{\mathrm{N}}(\eta)$,

$$P(\alpha) = \frac{1}{\pi^2}\int \exp(\eta^*\alpha - \eta\alpha^*)\xi_{\mathrm{N}}(\eta)\,\mathrm{d}^2\eta \,. \tag{2.7}$$

For more details, we refer to Ref. [47].

2.2.3 Wigner function

Another widely used quasi-probability distribution function is the Wigner function [48]. We define a characteristic function $\xi(\eta) = \mathrm{Tr}\{\hat{\rho}\hat{D}(\eta)\} = \mathrm{Tr}\{\hat{\rho}\mathrm{e}^{\eta\hat{a}^\dagger - \eta^*\hat{a}}\} = \xi_{\mathrm{N}}(\eta)\mathrm{e}^{-\frac{1}{2}|\eta|^2}$. The Wigner function is defined as the Fourier transform of this characteristic function,

$$W(\alpha) = \frac{1}{\pi^2}\int \exp(\eta^*\alpha - \eta\alpha^*)\xi(\eta)\,\mathrm{d}^2\eta \,. \tag{2.8}$$

Next we show that the moment matrix, $\left\langle (\hat{a}^\dagger)^m \hat{a}^n \right\rangle$ with $m, n \in \mathbb{N}_0$, contains the same information as the Wigner function [49,50]. The antinormally ordered moments are related to the normally ordered moments by

$$\hat{a}^m (\hat{a}^\dagger)^n = \sum_{j=0}^{\min(m,n)} \binom{m}{j} \binom{n}{j} j! (\hat{a}^\dagger)^{n-j} \hat{a}^{m-j} \,. \tag{2.9}$$

The characteristic function $\xi(\eta)$ becomes

$$\xi(\eta) = e^{-|\eta|^2/2} \sum_{m,n} \frac{\left\langle (\hat{a}^\dagger)^m \hat{a}^n \right\rangle}{m!\, n!} \eta^m \left(-\eta^*\right)^n \,. \tag{2.10}$$

Inserting the characteristic function $\xi(\eta)$ into Eq. (2.8) gives

$$W(\alpha) = \sum_{m,n} \frac{\left\langle (\hat{a}^\dagger)^m \hat{a}^n \right\rangle}{\pi^2\, m!\, n!} \int \eta^m \left(-\eta^*\right)^n \exp\left(-\frac{|\eta|^2}{2} + \alpha\eta^* - \alpha^*\eta \right) \mathrm{d}^2\eta \,. \tag{2.11}$$

Based on the complete moment matrix, we can obtain the Wigner function of an arbitrary state. Ref. [51] demonstrated that at least up to fourth order moments are needed to evaluate the negativity of a Wigner function. In our experiments, the limited detection efficiency only allows us to detect up to fourth order moments, $0 < m + n \leqslant 4$. For Gaussian states, on which we concentrate in this work, the Wigner function is fully described by the first two moments.

A Wigner function is often expressed in phase space. To this end, we introduce the quadrature operators $\hat{p}$ and $\hat{q}$, which are analogues to the position and momentum operators,

$$\hat{p} = \frac{1}{2\mathrm{i}} \left(\hat{a} - \hat{a}^\dagger\right) , \quad \hat{q} = \frac{1}{2} \left(\hat{a} + \hat{a}^\dagger\right) , \quad [\hat{q}, \hat{p}] = \frac{\mathrm{i}}{2}. \tag{2.12}$$

Here, i is the imaginary unit. This implies the Heisenberg inequality relation

$$(\Delta\hat{p})^2 (\Delta\hat{q})^2 \geqslant 1/16 \,. \tag{2.13}$$

In this thesis, for any operator A, we use $(\Delta\hat{A})^2$ to denote its variance,

$$(\Delta\hat{A})^2 \equiv \langle (\Delta\hat{A})^2 \rangle \equiv \langle \hat{A}^2 \rangle - \langle \hat{A} \rangle^2 \,. \tag{2.14}$$

A generalized quadrature operator is written as

$$\hat{X}_\delta = \hat{q}\cos\delta + \hat{p}\sin\delta\,, \tag{2.15}$$

where δ is the angle between $\hat{X}_\delta$ and $\hat{q}$. In Eq. (2.8), one needs to substitute α by $(q + \mathrm{i}p)$ to obtain the phase space expression. An alternative definition of the Wigner function is based on the Wigner-Weyl transform [52],

$$W(q,p) = \frac{1}{2\pi}\int \langle q - \zeta/2|\hat{\rho}|q + \zeta/2\rangle \mathrm{e}^{\mathrm{i}p\zeta}\mathrm{d}\zeta\,. \tag{2.16}$$

Ref. [53] has shown both definitions to be identical. Integration of the Wigner function over p, $\int W(q,p)\mathrm{d}p$ gives the probability distribution of q, and integration over q, $\int W(q,p)\mathrm{d}q$ gives the probability distribution of p.

In this work, we use Wigner functions to describe microwave states, such as vacuum states, coherent states, squeezed states, etc. All the Wigner function presented are unit-less and normalized to one. In Sec. 2.3 and Sec. 2.4, further discussions about Wigner functions of coherent states and squeezed states, respectively, are presented. In Chapter 6, the discussion of displacement operations are based on Wigner function reconstructions of various microwave states.

Besides the P-function and Wigner function discussed above, the Q-function is the Fourier transform of antinormally ordered characteristic function,

$$\xi_\mathrm{A}(\eta) = \mathrm{Tr}\{\hat{\rho}\mathrm{e}^{-\eta^*\hat{a}}\mathrm{e}^{\eta\hat{a}^\dagger}\}\,. \tag{2.17}$$

For more details, we refer to Ref. [47].

2.3 Displacement

Classically, an electromagnetic field has a well-defined phase and magnitude. But this is not the case when we consider the field quantum mechanically. In Sec. 2.2.3, we have introduced two conjugate quadrature operators $\hat{p}$ and $\hat{q}$ in Eq. (2.12). The fluctuations of the quadratures need to fulfill the Heisenberg uncertainty relation (Eq. (2.13)). When the field is in a vacuum state, the quadrature fluctuations are minimal, and the equal sign in the Heisenberg uncertainty relation (Eq. (2.13)) holds. In phase space, the vacuum state is located at the origin and its Wigner function is symmetric in all phase directions (Fig. 2.1 (a,d)). If we apply a displacement operator $\hat{D}(\alpha) = \exp\left(\alpha\hat{a}^\dagger - \alpha^*\hat{a}\right)$, which has been introduced in Sec. 2.2.2, to the

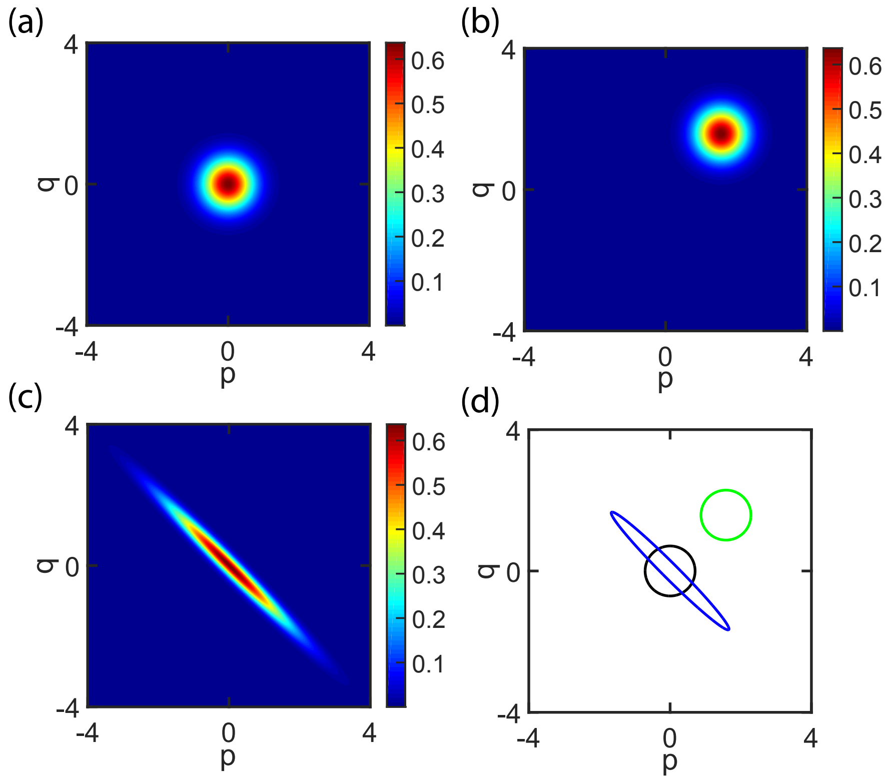

Figure 2.1: (a) Wigner function of the vacuum state. (b) Wigner function of a coherent state with $n = 5$. (c) Wigner function of a squeezed vacuum state with $r = 1.2$, and $n = 5$. Squeezed states are introduced in Sec. 2.4. (d) $1/\mathrm{e}$-contours of the Wigner function in (a)-black, (b)-green and (c)-blue.

vacuum state, the Wigner function is shifted by α, keeping its shape unchanged (Fig. 2.1 (a,b,d)). Here, $\alpha = |\alpha| \exp\left[\mathrm{i}\pi\left(90^\circ - \theta\right)/180^\circ\right]$. We define the coherent phase θ as the angle between the displacement direction and the p-axis. Therefore, we get coherent states $|\alpha\rangle = \hat{D}(\alpha)|0\rangle$. The coherent state $|\alpha\rangle$ is an eigenstate of $\hat{a}$,

$$\begin{aligned}\hat{a}|\alpha\rangle &= \alpha|\alpha\rangle\,,\\ \langle\alpha|\hat{a}^\dagger &= \alpha^*\langle\alpha|\,.\end{aligned} \tag{2.18}$$

The quadrature fluctuations in all directions are of the same size as for the vacuum state. The expectation value of the photon number operator is $\langle\alpha|\hat{n}|\alpha\rangle = \langle\alpha|\hat{a}^\dagger\hat{a}|\alpha\rangle = |\alpha|^2 \equiv n$. The Wigner function for a coherent state $|\alpha\rangle = |Q + iP\rangle$ is

$$W(q,p) = \frac{2}{\pi}\exp\left[-2\big((q-Q)^2 + (p-P)^2\big)\right], \tag{2.19}$$

and the $1/e$-contour is

$$(q - Q)^2 + (p - P)^2 = \frac{1}{2}\,. \tag{2.20}$$

The moment matrix reads $\langle\alpha|(\hat{a}^\dagger)^m \hat{a}^n|\alpha\rangle{=}(\alpha^*)^m\alpha^n$.

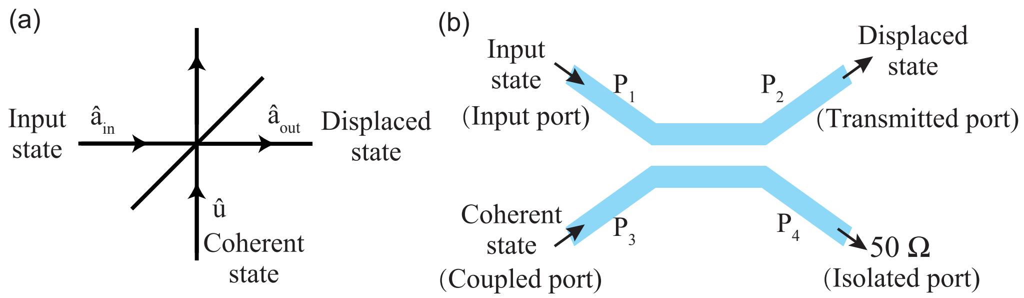

Figure 2.2: (a) Schematic of an antisymmetric beam splitter. (b) Schematic of a microstrip line directional coupler (not to the scale). P_i with $i = 1$, 2 , 3 and 4 , denotes the power of the signal at port i .

The field generated by a well stabilized microwave source is a coherent state, which is equivalent to a displaced vacuum state. In principle, a displacement operator $\hat{D}(\alpha)$ can be applied to any electromagnetic field. Experimentally, this can be realized with an antisymmetric beam splitter biased with a highly excited coherent state. Using $\hat{a}_{\text{in}}$ and $\hat{u}$ to denote the annihilation operators of the input state and the coherent state, respectively, as shown in Fig. 2.2(a), the beam splitter relation gives

$$\hat{a}_{\text{out}} = \sqrt{\tau}\hat{a}_{\text{in}} + \sqrt{\nu}\hat{u}\,, \tag{2.21}$$

where τ and ν are the power linear transmissivity and reflectivity, respectively, and $\hat{a}_{\text{out}}$ is the annihilation operator of the output state. The operator $\hat{u}$ applies on a coherent state $|\Phi_{\text{c}}\rangle$, which means $\hat{u}|\Phi_{\text{c}}\rangle = \tilde{u}|\Phi_{\text{c}}\rangle$, with $\tilde{u}$ as the eigenvalue. If $\tau \to 1$, Eq. (2.21) becomes

$$\hat{a}_{\text{out}} = \hat{a}_{\text{in}} + \sqrt{\nu}\tilde{u}\,. \tag{2.22}$$

This is analog to

$$\hat{D}^\dagger(\hat{\alpha})a^\dagger_{\text{in}}\hat{D}(\alpha) = \hat{a}_{\text{in}} + \alpha, \tag{2.23}$$

where $\alpha = \sqrt{\nu}\tilde{u}$. Therefore, the input state is displaced by α . For detailed theoretical treatment, we refer to Ref. [54]. In the microwave domain, a directional coupler (Fig. 2.2(b)) is an antisymmetric beam splitter. A low insertion loss from the input port to the transmitted port gives a high transmissivity for the input signal,

$$\text{Insertion loss(dB)} = 10\lg\frac{P_1}{P_2} = 10\lg\frac{1}{\tau}\,. \tag{2.24}$$

A low coupling factor indicates a low reflectivity,

$$\text{Coupling(dB)} = 10\lg\frac{P_2}{P_3} = 10\lg\nu\,. \tag{2.25}$$

Here, P_i with $i = 1\,,\ 2\,,\ 3$ and $4\,$, denotes power of the signal at port $i\,$.

2.4 Squeezing

Quadrature fluctuations of coherent states are equal to vacuum fluctuations,

$$(\Delta\hat{X}_\delta)^2 = \frac{1}{4}\,, \tag{2.26}$$

with δ the angle between $\hat{X}_\delta$ and $\hat{q}\,$. The relation in Eq. (2.26) applies to all quadratures with $0^\circ < \delta < 180^\circ\,$. If a state has a certain quadrature with

$$(\Delta\hat{X}_{\delta_{\mathrm{sq}}})^2 < \frac{1}{4}\,, \tag{2.27}$$

this state is a squeezed state, and the value δ_{sq} is the phase of the squeezed quadrature. In the following, we use $\hat{X}_{\mathrm{sq}}$ to denote the squeezed quadrature. To fulfill the Heisenberg uncertainty, the variance of the conjugate quadrature has to be larger than the vacuum fluctuations. The conjugate quadrature of $\hat{X}_{\mathrm{sq}}$ is called anti-squeezed quadrature, and denoted by $\hat{X}_{\mathrm{anti}}\,$.

Squeezed states can be generated by many nonlinear photon mixing processes. The parametric down conversion process, which also provides the basis for our JPA samples, is a three-wave mixing between the pump photons [32,37,39,55], the signal and idler photons. Due to a second-order nonlinear interaction, a pump photon splits into a signal and idler pair forming a squeezed state with $f_{\mathrm{pump}} = f_{\mathrm{signal}} + f_{\mathrm{idler}}\,$. When the signal and idler photons are emitted into the same mode, $f_{\mathrm{signal}} = f_{\mathrm{idler}}$, a single-mode squeezed state is generated. When $f_{\mathrm{signal}} \neq f_{\mathrm{idler}}$, a two-mode squeezed state is generated. Similarly, in the optical domain, fibers and nonlinear crystals in a cavity are often used to generate squeezed states [56–58]. In four-wave mixing, due to a third-order nonlinear process two pump photons produce a photon pair in a squeezed state [29], $2f_{\mathrm{pump}} = f_{\mathrm{signal}} + f_{\mathrm{idler}}\,$. Four-wave mixing is also a typical mechanism to generate squeezed states with atomic assembles in optical cavities [59]. Because of the unique properties of squeezed states, they have become primary building blocks in many applications based on propagating variables, such as low noise amplification [25, 27, 28, 30, 32, 34], quantum state engineering, quantum key distribution, quantum teleportation [14, 15], etc.

To define the squeezing level $\mathcal{S}$ in decibel, we compare the variance of the squeezed quadrature $(\Delta X_{\mathrm{sq}})^2$ with the vacuum fluctuations, obtaining

$$\mathcal{S} = -10\lg\left[(\Delta X_{\mathrm{sq}})^2/0.25\right] . \tag{2.28}$$

We note that $(\Delta X_{\mathrm{sq}})^2 < 0.25$ indicates squeezing and $\mathcal{S}$ is positive. Larger $\mathcal{S}$ corresponds to a higher squeezing level. $(\Delta X_{\mathrm{sq}})^2 \geq 0.25$ means no squeezing and $\mathcal{S} < 0$. We still use $\mathcal{S}$ to evaluate the quadrature variances of a state if the state is not squeezed below vacuum ($\mathcal{S} < 0$). In this work we use the nomenclature that the term "squeezing" is equivalent to "squeezing below the vacuum level".

2.4.1 Squeezed vacuum states

To describe squeezed states mathematically, we introduce a squeeze operator

$$\hat{S}(\xi) = \exp\left(\frac{1}{2}\xi^*\hat{a}^2 - \frac{1}{2}\xi(\hat{a}^\dagger)^2\right) , \tag{2.29}$$

where ξ denotes the complex squeeze parameter $\xi = r\mathrm{e}^{\mathrm{i}\tilde{\varphi}}$ with squeeze factor $r \geq 0$ and squeezing angle $\tilde{\varphi}$. Here, $\tilde{\varphi}/2$ is the angle between the squeezed quadrature and the q-axis. Very often, the anti-squeezed angle $\gamma = -\tilde{\varphi}/2$ as the angle between the anti-squeezed quadrature and the p-axis is used. Applying the squeeze operator to vacuum states $\hat{S}(\xi)|0\rangle$, we get squeezed vacuum states; to thermal states, we get squeezed thermal states; to coherent states, we get squeezed coherent states.

The Wigner function of a squeezed vacuum state $\hat{S}(\xi)|0\rangle$ is

$$\begin{aligned} W(q,p) =& \frac{2}{\pi}\exp\Big[-(\mathrm{e}^{2r}+\mathrm{e}^{-2r})|q+\mathrm{i}p|^2 - \frac{1}{2}(\mathrm{e}^{2r}-\mathrm{e}^{-2r})\mathrm{e}^{-\mathrm{i}\tilde{\varphi}}(q+\mathrm{i}p)^2 \\ & -\frac{1}{2}(\mathrm{e}^{2r}-\mathrm{e}^{-2r})\mathrm{e}^{i\tilde{\varphi}}(q-\mathrm{i}p)^2\Big] , \end{aligned} \tag{2.30}$$

and the $1/e$-contour is an ellipse,

$$\frac{\left(q\cos\frac{\tilde{\varphi}}{2} + p\sin\frac{\tilde{\varphi}}{2}\right)^2}{\mathrm{e}^{-2r}} + \frac{\left(p\cos\frac{\tilde{\varphi}}{2} - q\sin\frac{\tilde{\varphi}}{2}\right)^2}{\mathrm{e}^{2r}} = \frac{1}{2} . \tag{2.31}$$

The length of the major axis is $\mathrm{e}^r/\sqrt{2}$, and the minor axis $\mathrm{e}^{-r}/\sqrt{2}$. The uncertainty of the squeezed and the anti-squeezed quadratures are $\mathrm{e}^{-2r}/4$ and $\mathrm{e}^{2r}/4$, respectively. The number of photons in the state is $\langle\hat{n}\rangle = \sinh^2 r$. Fig. 2.1(c) shows the Wigner function of a squeezed vacuum state with $r = 1.2$, and photon number $n = 5$.

2.4.2 Squeezed coherent states

There are two ways to obtain a squeezed coherent state. First, one can apply a displacement operator to a vacuum state $\hat{D}(\alpha)|0\rangle$, and subsequently squeeze this displaced vacuum $\hat{S}(\xi)\hat{D}(\alpha)|0\rangle$. Second, one can squeeze the vacuum state $\hat{S}(\xi)|0\rangle$ and apply a displacement operator $\hat{D}(\alpha)\hat{S}(\xi)|0\rangle$. To distinguish between these states, we call the states generated with the first method squeezed coherent states, and those obtained with the second method coherent squeezed states. We illustrate the difference of the two methods in Fig. 2.3. For the former method, the displacement of the squeezed coherent state depends on both the displacement and squeeze operations. When the anti-squeezed quadrature is parallel to the displacement direction of the coherent state $\hat{D}(\alpha)|0\rangle$, the final displacement of the squeezed coherent state is maximal (Fig. 2.3(a)). Contrary, the final displacement reaches its

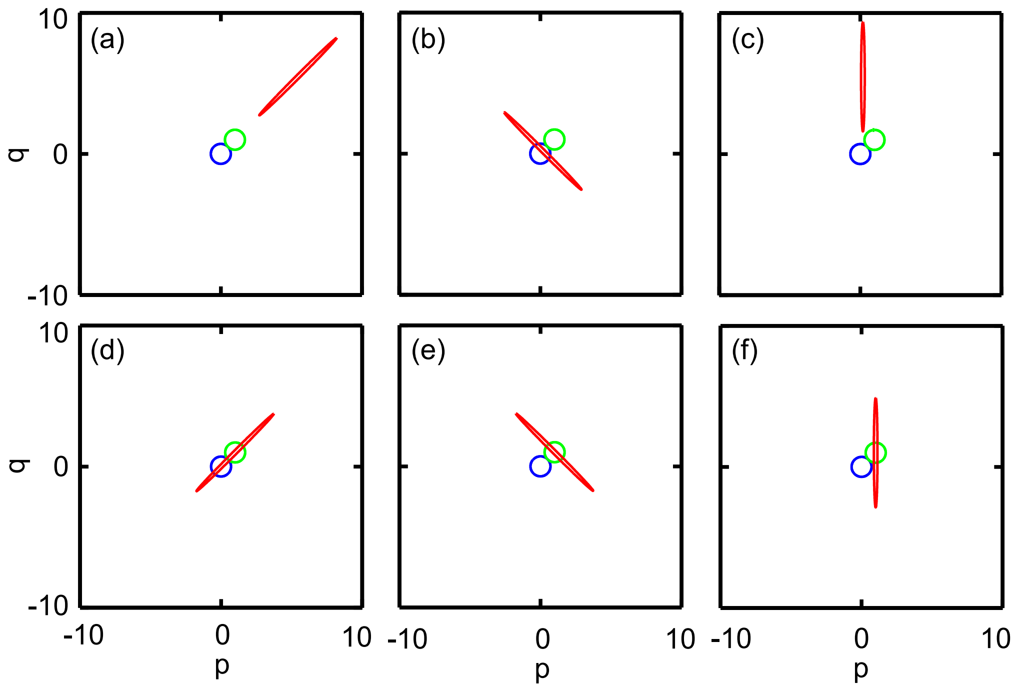

Figure 2.3: Sketch of $1/e$ contours of the ideal vacuum (blue), the coherent state (green), the squeezed coherent state (red) for (a-c) and the coherent squeezed states (red) for (d-f) with $r = 1.7$, $\theta = 45°$ and $|\alpha|^2 = 2$. p and q are dimensionless quadrature variables spanning the phase space. (a)–(c) Displace the vacuum first, then squeeze. (d)–(f) Squeeze the vacuum state first, then displace. The anti-squeezed angle γ is $45°$ in (a) and (d), $135°$ in (b) and (e) and $90°$ in (c) and (f). Reprinted figure from Ref. [32].

minimal value when the anti-squeezed quadrature is perpendicular to the displacement direction of the coherent state (Fig. 2.3(b)). However, the final displacement of the coherent squeezed state obtained from the second method only depends on the displacement operation and is independent of the squeeze factor r (Fig. 2.3(d)–(f)). The difference can be seen from the moment matrix. The displacement operation does not change the shape of the Wigner function. It only makes a linear displacement in phase space. The experimental implementations of both squeezed coherent states and coherent squeezed states are discussed in Chapter 6.

For a squeezed coherent state, the moments (up to second order) are [47]

$$\langle\hat{a}\rangle = \alpha\cosh r - \alpha^* \mathrm{e}^{\mathrm{i}\tilde{\varphi}}\sinh r\,, \tag{2.32}$$

$$\begin{aligned}\langle\hat{a}^2\rangle &= \alpha^2\cosh^2 r + (\alpha^*)^2\mathrm{e}^{2\mathrm{i}\tilde{\varphi}}\sinh^2 r \\ &\quad - 2|\alpha|^2\mathrm{e}^{\mathrm{i}\tilde{\varphi}}\sinh r\cosh r - \mathrm{e}^{\mathrm{i}\tilde{\varphi}}\sinh r\cosh r\,,\end{aligned} \tag{2.33}$$

$$\begin{aligned}\langle\hat{a}^\dagger\hat{a}\rangle &= |\alpha|^2(\cosh^2 r + \sinh^2 r) - (\alpha^*)^2\mathrm{e}^{\mathrm{i}\tilde{\varphi}}\sinh r\cosh r \\ &\quad - \alpha^2\mathrm{e}^{-\mathrm{i}\tilde{\varphi}}\sinh r\cosh r + \sinh^2 r\,.\end{aligned} \tag{2.34}$$

For a coherent squeezed state, the moments (up to fourth order) are

$$\langle\hat{a}\rangle = \alpha\,, \tag{2.35}$$

$$\langle\hat{a}^2\rangle = \alpha^2 - \mathrm{e}^{\mathrm{i}\tilde{\varphi}}\sinh r\cosh r\,, \tag{2.36}$$

$$\langle\hat{a}^\dagger\hat{a}\rangle = |\alpha|^2 + \sinh^2 r\,, \tag{2.37}$$

$$\langle\hat{a}^3\rangle = \alpha^3 - 3\alpha\mathrm{e}^{\mathrm{i}\tilde{\varphi}}\sinh r\cosh r\,, \tag{2.38}$$

$$\langle\hat{a}^\dagger\hat{a}^2\rangle = |\alpha|^2\alpha + 2\alpha\sinh^2 r - \alpha^*\mathrm{e}^{\mathrm{i}\tilde{\varphi}}\sinh r\cosh r\,, \tag{2.39}$$

$$\langle\hat{a}^4\rangle = \alpha^4 - 6\alpha^2\mathrm{e}^{\mathrm{i}\tilde{\varphi}}\sinh r\cosh r + 3\mathrm{e}^{2\mathrm{i}\tilde{\varphi}}\sinh^2 r\cosh^2 r\,, \tag{2.40}$$

$$\langle\hat{a}^\dagger\hat{a}^3\rangle = |\alpha|^2\alpha^2 + 3\alpha^2\sinh^2 r - 3|\alpha|^2\mathrm{e}^{\mathrm{i}\tilde{\varphi}}\sinh r\cosh r - 3\mathrm{e}^{\mathrm{i}\tilde{\varphi}}\sinh^3 r\cosh r\,, \tag{2.41}$$

$$\begin{aligned}\langle\hat{a}^{\dagger 2}\hat{a}^2\rangle &= |\alpha|^4 - \alpha^2\mathrm{e}^{-\mathrm{i}\tilde{\varphi}}\sinh r\cosh r - \alpha^{*2}\mathrm{e}^{\mathrm{i}\tilde{\varphi}}\sinh r\cosh r \\ &\quad + 4|\alpha|^2\sinh^2 r + \sinh^2 r\cosh^2 r\,.\end{aligned} \tag{2.42}$$

Here, $\alpha = |\alpha|\exp\left[\mathrm{i}\pi\left(90^\circ - \theta\right)/180^\circ\right]$, and $n = |\alpha|^2$. The equalities $\langle\hat{a}^\dagger\rangle = \langle\hat{a}\rangle^*$, $\langle(\hat{a}^\dagger)^2\rangle = \langle\hat{a}^2\rangle^*$, $\langle\hat{a}^{\dagger 3}\rangle = \langle\hat{a}^3\rangle^*$, $\langle\hat{a}^{\dagger 2}\hat{a}\rangle = \langle\hat{a}^\dagger\hat{a}^2\rangle^*$, $\langle\hat{a}^{\dagger 4}\rangle = \langle\hat{a}^4\rangle^*$ and $\langle\hat{a}^{\dagger 3}\hat{a}\rangle = \langle\hat{a}^\dagger\hat{a}^3\rangle^*$ are valid for both cases.

2.5 Microwave transmission line

A transmission line for electromagnetic waves usually is modeled using distributed circuit elements, which means the circuit network length is comparable to or larger than the wavelength of the electromagnetic signal. Thus, voltages and currents vary in space. For a lossless transmission line, the characteristic impedance (Z) is determined by the inductance and capacitance per unit length, denoted as L' and C' , respectively,

$$Z = \sqrt{\frac{L'}{C'}}. \tag{2.43}$$

When a wave travels from a transmission line with a characteristic impedance Z_1 to another transmission line with a characteristic impedance Z_2, and $Z_2 \neq Z_1$, the wave is partially reflected and partially transmitted. The amplitude reflection coefficient Γ is

$$\Gamma = \frac{Z_2 - Z_1}{Z_2 + Z_1}, \tag{2.44}$$

and the amplitude transmission coefficient $T = 1 + \Gamma$. Transmission lines in our applications have a characteristic impedance of about $50\,\Omega$ to comply with standard microwave devices.

In circuit QED systems, superconducting CoPlanar Waveguides (CPWs) are

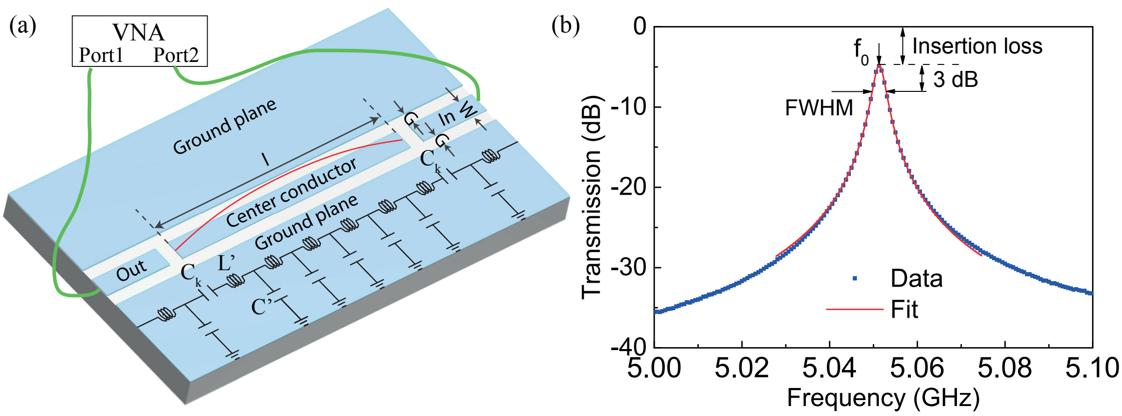

Figure 2.4: (a) Schematic of a CPW resonator on a substrate (not to the scale). A lossless CPW resonator is modeled as a chain of LC oscillators with L' and C' as the inductance and capacitance per unit length, and it is coupled to the feed line via coupling capacitors C_k. Green lines indicate microwave cables which connect VNA to the resonator input and output ports. The red curve indicates the fundamental current mode. (b) A typical transmission spectrum of a Nb CPW resonator on Si substrate measured at $4\,\mathrm{K}$. The red line is a Lorentzian fit, and the blue squares denote measurement data. f_0 represents the resonant frequency of the fundamental mode, and FWHM means Full Width at Half Maximum.

widely used as microwave transmission lines. A CPW consists of ground planes, a center conductor, gaps which separate the center conductor from the ground planes (Fig. 2.4). CPWs have several advantages. First, it is easy to design and fabricate a desired characteristic impedance by adjusting the width of the center conductor (W) and the widths of the gaps G (Fig. 2.4). Second, it is convenient to integrate circuits based on Josephson junctions, which are introduced in Sec. 2.7, into the CPWs based on modern integrated circuit technology. Third, the typically small lateral dimensions of CPWs provide large vacuum fields, which is very important for experiments studying the fundamental light-matter interaction.

2.6 Microwave resonator

The two gaps interrupting the center conductor of a transmission line act as reflecting mirrors and can be modeled as two capacitors. Standing waves are formed between the two mirrors with current nodes at the capacitors. In this case the resonator length is half the wavelength of the fundamental mode, therefore this type of resonator is called $\lambda/2$ resonator. Different boundary conditions give different types of resonators. When one coupling capacitor is replaced by a short, which means the center conductor is connected to a ground plane, a $\lambda/4$ resonator is formed.

Fig. 2.4(a) shows a schematic of a $\lambda/2$ CPW resonator. The two coupling capacitors, marked with C_{k}, couple signals into the resonator and also couple the resonator to feed lines for measurements. The characteristic impedance of $50\,\Omega$ is realized by adjusting the center conductor width W and the gap width G. The red curve indicates the fundamental current mode, the wavelength of which is twice the resonator length l. By connecting the input and output ports, which are marked with "in" and "out", respectively, to a Vector Network Analyzer (VNA), transmission and reflection measurements can be performed. Fig. 2.4(b) shows a typical experimental transmission curve of a Nb resonator on a Si substrate measured with a VNA at $4\,\mathrm{K}$. The transmission shows a Lorenzian peak.

There are three important parameters to describe a resonator: resonance frequencies, internal quality factors Q_{int} and external quality factors Q_{ext}. At resonance the resonator can be simply modeled by a parallel LC circuit, if the resistive part due to the resonator losses is ignored. The stored energy oscillates between the capacitor and the inductor without external excitation. The resonance frequencies of the different modes can be written as

$$\omega_{\mathrm{m}} \equiv 2\pi f_{\mathrm{m}} = \frac{c}{\sqrt{\epsilon_{\mathrm{eff}}}}\frac{\pi}{l} = m\frac{1}{\sqrt{L'C'}}\frac{\pi}{l}\,, \tag{2.45}$$

where ϵ_{eff} is the effective dielectric constant of the CPW, l is the resonator length, L' and C' are the inductance and capacitance per unit length, respectively, c is the speed of light, and m is the mode number $m = 1, 2, 3\ldots$ The fundamental mode corresponds to $m = 1$. Very often, f_0 is used to denote the fundamental mode. The internal (Q_{int}) and the external quality factor (Q_{ext}) together determine the total loaded quality factor Q by

$$\frac{1}{Q} = \frac{1}{Q_{\mathrm{int}}} + \frac{1}{Q_{\mathrm{ext}}}\,. \tag{2.46}$$

Q characterizes the energy loss rate, and for each mode it is defined as

$$Q_{\mathrm{m}} = 2\pi\frac{\text{energy stored}}{\text{energy lost per cycle}} = \frac{f_{\mathrm{m}}}{\mathrm{FWHM}}\,. \tag{2.47}$$

Here, the Full Width at Half Maximum (FWHM) characterizes the linewidth of the resonant mode m. The loss channel induced by the coupling to external circuits via C_k determines the external quality factor Q_{ext}. The internal quality factor Q_{int} characterizes intrinsic losses in the resonator. For a superconducting CPW resonator, the internal losses include the dielectric loss due to two-level systems, the quasiparticle loss due to a finite temperature, and the radiation loss.

Similar to a mechanical oscillator, the quantum mechanical treatment of a harmonic oscillator also applies to an electromagnetic resonator. The Hamiltonian is

$$\hat{H} = \hbar\omega\left(\hat{a}^{\dagger}\hat{a} + \frac{1}{2}\right)\,, \tag{2.48}$$

and the energy eigenvalues are

$$E_{\tilde{m}} = \hbar\omega\left(\tilde{m} + \frac{1}{2}\right)\,. \tag{2.49}$$

Here, $\hat{a}$ and $\hat{a}^{\dagger}$ are the annihilation and creation operators, respectively, and ω is the angular resonance frequency. We point out that Eqs. (2.48)-(2.49) describe a single resonant mode. The characteristic energy $\hbar\omega$ is the energy quantum of the electromagnetic field, which is the energy of a single photon. Even in the vacuum state, i.e. in the absence of any photon $\tilde{m} = 0$, the energy is $\hbar\omega/2$, which is called zero-point energy.

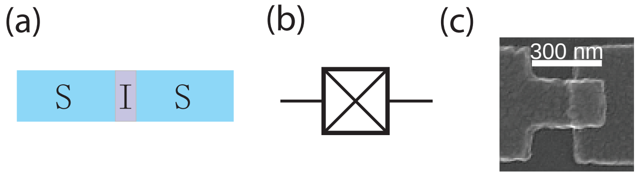

Figure 2.5: (a) Schematic of a JJ consisting of two superconductors (S) and an isolator (I). Dimensions are not to the scale. (b) Circuit symbol of a JJ. (c) Scanning electron micrograph of a typical Al-AlO_x-Al JJ. Reprinted figure from Ref. [60].

2.7 Josephson junction

Josephson Junctions (JJs) are fundamental building blocks in circuit QED systems due to their non-linear transport properties. A JJ consists of two weakly coupled superconductors. Such weak coupling can be established by a weak link, a normal metal layer or a thin isolating layer (Fig. 2.5 (a)). We use Al-AlO_x-Al junctions (Fig. 2.5 (c)) fabricated by shadow evaporation [61]. Here, we only consider the case where the supercurrent density is uniform in the area perpendicular to the current flow and the junction width and length are smaller than the Josephson penetration depth. In this case (quasi zero-dimensional junction), the current-phase relation and the voltage-phase relation are

$$I(\varphi) = I_{\mathrm{c}} \sin\varphi \,, \qquad \frac{\partial \varphi}{\partial t} = \frac{2\pi}{\Phi_0} V(t) \,, \tag{2.50}$$

respectively. Here, $\Phi_0 = h/2e$ is the magnetic flux quantum with h the Planck constant and e the electron charge, I_c is the junction critical current, φ is the phase difference between the two superconductors, and I (V) is the current (voltage) across the junction. According to these two relations, a constant dc current with $-I_{\mathrm{c}} \leq I \leq I_{\mathrm{c}}$ can flow as a supercurrent through the JJ without a voltage drop, and a constant dc voltage across the JJ leads to an oscillating current.

There are two characteristic energies of a JJ, the Josephson coupling energy E_{J}

$$E_{\mathrm{J}} = \frac{\Phi_0 I_{\mathrm{c}}}{2\pi}(1 - \cos\varphi) \tag{2.51}$$

and the charging energy E_{c}

$$E_{\mathrm{c}} = \frac{1}{2}\frac{(2e)^2}{C_{\mathrm{J}}} \,. \tag{2.52}$$

Here, E_{J} describes the binding energy of the two superconductors due to the overlap of their wave functions, and E_{c} corresponds to the charge energy of a single Cooper

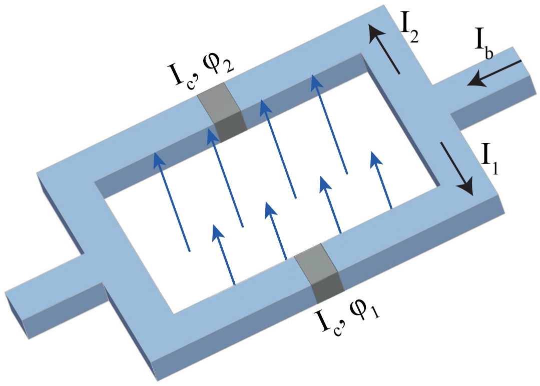

Figure 2.6: Schematic of a dc-SQUID. Dimensions are not to the scale. Two JJs have the critical current I_c, and phase differences $\varphi_{1,2}$. The currents through the two junctions are denoted by $I_{1,2}$, and the total dc bias current through the SQUID is denoted with I_b. Blue arrows indicate external magnetic flux through the SQUID loop.

pair on the Josephson capacitor C_J.

2.8 Dc-SQUID

When two JJs are combined in parallel as shown in Fig. 2.6, we get a direct current Superconducting QUantum Interference Device (dc-SQUID). In the following, the two JJs are assumed to be identical. The flux quantization implies [62]

$$\varphi_1 - \varphi_2 = 2\pi\frac{\Phi}{\Phi_0} + 2\pi n\,, \tag{2.53}$$

with $n \in \mathbb{Z}$. Therefore, the total current I_b through the SQUID is

$$\begin{aligned} I_\mathrm{b} &= I_\mathrm{c}\sin\varphi_1 + I_c\sin\varphi_2 \\ &= 2I_c\cos\left(\pi\frac{\Phi}{\Phi_0} + n\pi\right)\sin\left(\varphi_2 + \pi\frac{\Phi}{\Phi_0} + n\pi\right)\,. \end{aligned} \tag{2.54}$$

Here, $\varphi_{1,2}$ are the phase differences for each junction. The total magnetic flux threading the loop Φ is determined by an external applied magnetic flux Φ_ext and the flux generated by the circulating current $I_\mathrm{cir} = \frac{I_1 - I_2}{2}$,

$$\Phi = \Phi_\mathrm{ext} - L_\mathrm{loop}I_\mathrm{cir}\,, \tag{2.55}$$

where L_{loop} is the loop inductance. We introduce a screening parameter $\beta \equiv \frac{2L_{\mathrm{loop}}I_{\mathrm{c}}}{\Phi_0}$. If $\beta = 0$, the second term in Eq. (2.55) is zero, and $\Phi = \Phi_{\mathrm{ext}}$. Eq 2.54 is rewritten as

$$I_{\mathrm{b}} = 2I_{\mathrm{c}} \cos\left(\pi\frac{\Phi_{\mathrm{ext}}}{\Phi_0} + n\pi\right) \sin\left(\varphi_2 + \pi\frac{\Phi_{\mathrm{ext}}}{\Phi_0} + n\pi\right) . \tag{2.56}$$

At a fixed Φ_{ext}, φ_2 has a value which gives the maximum supercurrent through the loop,

$$I_{\mathrm{squid}} = 2I_{\mathrm{c}} \left|\cos\left(\pi\frac{\Phi_{\mathrm{ext}}}{\Phi_0}\right)\right| . \tag{2.57}$$

We can assign the inductance L_{squid} to the SQUID which depends on its critical current I_{squid},

$$L_{\mathrm{squid}} = \frac{\Phi_0}{2\pi I_{\mathrm{squid}}} . \tag{2.58}$$

We conclude that a dc-SQUID can be considered as a flux dependent inductor. In this work, the inductance of a dc-SQUID is modulated by modulating the flux through the SQUID. Since SQUIDs are very sensitive to magnetic flux, they are widely used to detect any signal that can be converted to a magnetic flux, such as voltage, current and gravity. Therefore, it allows for a broad range of applications in many areas, such as biomagnetic imaging, microscopy, etc [62].

2.9 Flux-driven JPA

A parametric amplifier is an oscillator whose resonant frequency ω_{r} is modulated periodically in time, $\omega_{\mathrm{r}} \to \omega_{\mathrm{r}}[1 + \delta_{\mathrm{p}}\cos(\omega_{\mathrm{p}}t)]$, with the modulation frequency ω_{p} and the modulation magnitude δ_{p}. Neglecting the δ_{p}^2 terms, the Hamiltonian of the parametric amplifier becomes

$$\hat{H} = \hbar\omega_{\mathrm{r}}\left(\hat{a}^\dagger\hat{a} + 2\delta_{\mathrm{p}}\cos(\omega_{\mathrm{p}}t)(\hat{a} + \hat{a}^\dagger)^2 + \frac{1}{2}\right) . \tag{2.59}$$

A detailed theoretical treatment is given in Ref. [64]. In the case of a JPA, the oscillating system is a $\lambda/4$ CPW resonator whose resonant frequency is determined by its capacitance and inductance (see Fig. 2.7(a)). The latter can be tuned by a dc-SQUID. The external magnetic flux through the dc-SQUID, Φ_{ext}, contains two parts: Φ_{dc} and Φ_{rf}. The dc flux Φ_{dc} is generated by a magnetic field coil and the ac flux Φ_{rf} comes from a radio frequency pump tone. By modifying Φ_{dc}, the resonant frequency can be adjusted. Fig. 2.7(b) shows the flux dependence of the resonance frequency of one JPA sample, which is labeled as Q300 JPA. By fitting

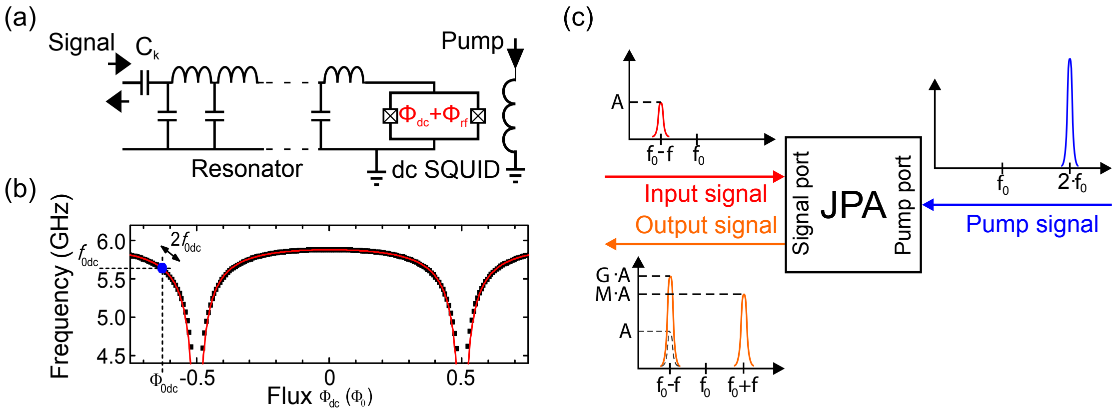

Figure 2.7: Flux driven JPA. (a) Circuit diagram. The transmission line resonator is terminated by a dc-SQUID (loop with crosses symbolizing Josephson junctions) at one end. A magnetic flux $\Phi_{\mathrm{dc}} + \Phi_{\mathrm{rf}}$ penetrating the dc-SQUID modulates the resonant frequency. (b) Dependence of the resonant frequency on the dc flux Φ_{dc}. The red line is a fit of a distributed circuit model [63] to the data (black square). Blue dot indicates the operation point for Q300 JPA in our experiments. (c) Schematic of the operating principle of the JPA (see text for details). Reprinted figure from Ref. [32].

a theoretical model [63] to the experimental data (black squares), we can estimate a Josephson coupling energy $E_{\mathrm{J}} = h \times 1305\,\mathrm{GHz}$ for each junction, where h is the Planck constant.

Periodically varying the resonant frequency with an ac flux Φ_{rf} at $2f_0$, where f_0 is the operation point frequency, results in parametric amplification: A signal at $f_0 - f$ incident at the signal port is amplified by the signal gain G and reflected back to the signal port. At the same time, an idler mode at $f_0 + f$ is created, whose amplitude is determined by the intermodulation gain M. This operation principle is depicted in Fig. 2.7(c). If the incoming signal consists of vacuum fluctuations, this process is the analogue of parametric down-conversion in optics, where a pump photon splits into a signal and an idler photon. Energy and momentum are conserved during this process. Energy conservation requires $f_{\mathrm{pump}} = f_{\mathrm{signal}} + f_{\mathrm{idler}}$, while momentum conservation establishes phase correlations between the signal, idler and pump modes. The destructive interference between signal and idler modes leads to squeezing.

Chapter 3

Quantum communication with propagating microwaves

Entanglement is a unique property of a composite quantum system. Due to the correlations between the subsystems, a measurement on one subsystem projects the other subsystems into a specific state. Since the subsystems can be spatially separated, entanglement becomes an important resource for quantum teleportation, quantum computing, quantum communication, etc. In this chapter, we first describe a two-mode squeezed vacuum state, which is a representative of an entangled state containing two subsystems. Then we discuss its $G^{(2)}$ correlation function, which is an important quantity for the protocol of quantum teleportation. We also explain a quantum teleportation protocol based on propagating microwave photons. In the end, a remote state preparation protocol used to benchmark all the building blocks for quantum teleportation is presented.

3.1 Two-mode squeezed vacuum state

In Sec. 2.4, we have discussed single-mode squeezed states which can be generated by a JPA operating in the degenerate mode. When the JPA is operated in the non-degenerate mode, which means that the signal and idler modes have different frequencies, the correlations between the signal and idler modes establish a two-mode squeezed state [36, 58]. Alternatively, a two-mode squeezed state formed by two spatially separated modes with the same frequency can be generated by a balanced beam splitter with two squeezed states at the inputs [35, 39]. Two-mode squeezed states generated by various methods have the same mathematical representation, and different applications. The second method has been widely used in quantum teleportation [14, 15] to generate EPR pairs.

In analogy with the single-mode squeeze operator (Eq. (2.4.1)), we introduce a two-mode squeeze operator,

$$\hat{S}_{(a,b)}(\xi) = \exp\left(\xi^* \hat{a}\hat{b} - \xi \hat{a}^\dagger \hat{b}^\dagger\right) . \tag{3.1}$$

Similar to single-mode squeezing, $\xi = r\exp(i\tilde{\varphi}_{(a,b)})$, and $\hat{a}$, $\hat{b}$, $\hat{a}^\dagger$ and $\hat{b}^\dagger$ are the operators of the two photonic modes. We notice that $\hat{S}_{(a,b)}$ is not the product of two single-mode operators. A two-mode squeezed vacuum state is obtained by applying $\hat{S}_{(\mathrm{a,b})}(\xi)$ onto a two-mode vacuum $|0,0\rangle$,

$$\hat{S}_{(\mathrm{a,b})}(\xi)|0,0\rangle = \exp\left(\xi^* \hat{a}\hat{b} - \xi \hat{a}^\dagger \hat{b}^\dagger\right)|0,0\rangle . \tag{3.2}$$

The two-mode squeezed vacuum state is not a product of two squeezed vacuum states. It is an entangled state containing correlations between two modes. Each mode itself is a thermal state with a photon number $\langle \hat{n}_\mathrm{a}\rangle = \langle \hat{n}_\mathrm{b}\rangle = \sinh^2 r \equiv n$. Also, the quadrature fluctuations are identical for all phase angles, $(\Delta\hat{p}_x)^2 = (\Delta\hat{q}_x)^2 = \frac{1}{4}\cosh 2r = \frac{1}{2}n + \frac{1}{4}$ with $x = a, b$. Therefore, the squeezing does not exist in the individual modes, but in the superposition of two modes. We introduce the superposition quadrature operators $\hat{P}_{(a,b)}$ and $\hat{Q}_{(a,b)}$,

$$\hat{P}_{(\mathrm{a,b})} = \frac{1}{\sqrt{2}}\left(\hat{p}_\mathrm{a} + \hat{p}_\mathrm{b}\right) , \quad \hat{Q}_{(\mathrm{a,b})} = \frac{1}{\sqrt{2}}\left(\hat{q}_\mathrm{a} + \hat{q}_\mathrm{b}\right) , \quad [\hat{Q}, \hat{P}] = \frac{\mathrm{i}}{2} , \tag{3.3}$$

where $\hat{p}_\mathrm{a,b}$ and $\hat{q}_\mathrm{a,b}$ are quadrature operators defined in Eq. (2.12). The variance of the superposition quadratures depends on the squeezing angle $\tilde{\varphi}_{(\mathrm{a,b})}$. The variances of the squeezed and anti-squeezed superposition quadratures are $\mathrm{e}^{-2r}/4$ and $\mathrm{e}^{2r}/4$, respectively. These expressions are the same as for the single-mode squeezed vacuum state in Sec. 2.4. The Wigner function of a two-mode squeezed vacuum state [65] is [1]

$$W_{(\mathrm{a,b})}(p_\mathrm{a}, q_\mathrm{a}, p_\mathrm{b}, q_\mathrm{b}) = \\ \frac{4}{\pi^2}\exp\left\{-e^{-2r}[(p_\mathrm{a}-p_\mathrm{b})^2 + (q_\mathrm{a}+q_\mathrm{b})^2] - e^{2r}[(p_\mathrm{a}+p_\mathrm{b})^2 + (q_\mathrm{a}-q_\mathrm{b})^2]\right\} . \tag{3.4}$$

[1] To simplify the expresson, the coordinate system is rotated until $\hat{P}_{(\mathrm{a,b})}$ is the squeezed quadrature.

In the limit of infinite squeezing, $r \to \infty$, the Wigner function becomes

$$W_{(\mathrm{a,b})}(p_\mathrm{a}, q_\mathrm{a}, p_\mathrm{b}, q_\mathrm{b}) = \begin{cases} 1 & \text{if} \quad p_\mathrm{a} + p_\mathrm{b} = 0 \quad \text{and} \quad q_\mathrm{a} - q_\mathrm{b} = 0 \\ 0 & \text{if} \quad p_\mathrm{a} + p_\mathrm{b} \neq 0 \quad \text{or} \quad q_\mathrm{a} - q_\mathrm{b} \neq 0 \end{cases} \tag{3.5}$$

This relation implies

$$\hat{p}_\mathrm{a} + \hat{p}_\mathrm{b} = 0 \quad \text{and} \quad \hat{q}_\mathrm{a} - \hat{q}_\mathrm{b} = 0 \tag{3.6}$$

for ideal two-mode squeezed vacuum states.

3.2 Correlation functions

Correlation functions are widely used in the characterization of radiation fields [66, 67]. To measure the correlation functions, single-photon detectors are used in the optical domain. In the microwave domain, due to the lack of single microwave photon detectors, linear amplifiers together with quadrature-based detection techniques turn out to be efficient tools to detect quasi-distribution functions of microwaves [39, 41, 43], as well as temporal correlations of propagating microwave signals [68].

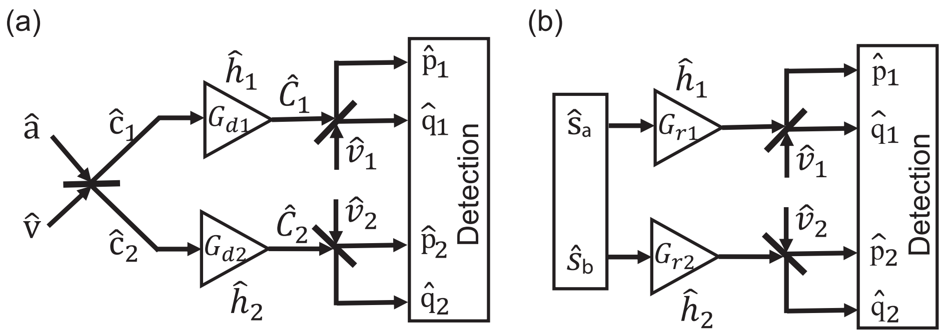

Figure 3.1: (a) Schematic of a setup for the dual-path method. (b) Schematic of a setup for the reference state method.

3.2.1 Dual-path method

First we discuss how to calculate correlation functions using a dual-path setup [39, 41, 43]. In the following, we use subscripts "1, 2" to indicate two different detection chains, and the subscript "d" to denote the dual-path method and "r" the reference state method. As shown in Fig. 3.1(a), the beam splitter relates the input and output modes as

$$\hat{c}_1 = \frac{1}{\sqrt{2}}\left(\hat{a}+\hat{v}\right) , \tag{3.7}$$

$$\hat{c}_2 = \frac{1}{\sqrt{2}}\left(-\hat{a}+\hat{v}\right) , \tag{3.8}$$

where $\hat{a}$ is the bosonic annihilation operator of the signal under study, and $\hat{v}$ is the bosonic annihilation operator of a reference mode. We choose the vacuum state as the reference mode. $\hat{c}_{1,2}$ denote the bosonic operators of the output modes. Then, $\hat{c}_{1,2}$ are amplified by the detection chains with effective gains G_{d1} and G_{d2}. The noise added during amplification is represented by the bosonic operators $\hat{h}_{1,2}$ and $\hat{h}^\dagger_{1,2}$ [22]. This process can be written as

$$\hat{C}_{1,2} = \sqrt{G_{\mathrm{d1,d2}}}\,\hat{c}_{1,2} + \sqrt{G_{\mathrm{d1,d2}}-1}\,\hat{h}^\dagger_{1,2} \,. \tag{3.9}$$

Subsequently, using room temperature IQ-mixers we get access to the quadrature components, $\hat{p}_{1,2}$ and $\hat{q}_{1,2}$, which are digitized by Analogy-to-Digital Converters (ADCs). We define a complex envelope operator as $\hat{\xi}_{1,2} \equiv \hat{p}_{1,2} + \mathrm{i}\hat{q}_{1,2}$. The IQ mixers fulfill the relation

$$\hat{\xi}_{1,2} = \hat{C}_{1,2} + \hat{v}^\dagger_{1,2} \,, \tag{3.10}$$

where $\hat{v}_{1,2}$ are the annihilation operators of the added noise by the IQ-mixers. By combining the Eqs. (3.7)-(3.10), the detected signals are

$$\hat{\xi}_1 = \sqrt{\frac{G_{\mathrm{d1}}}{2}}(+\hat{a}+\hat{v}) + \sqrt{G_{\mathrm{d1}}-1}\hat{h}^\dagger_1 + \hat{v}^\dagger_1 \,, \tag{3.11}$$

$$\hat{\xi}_2 = \sqrt{\frac{G_{\mathrm{d2}}}{2}}(-\hat{a}+\hat{v}) + \sqrt{G_{\mathrm{d2}}-1}\hat{h}^\dagger_2 + \hat{v}^\dagger_2 \,. \tag{3.12}$$

We define the operators

$$\hat{V}_{1,2} \equiv \sqrt{\frac{2}{G_{\mathrm{d1,2}}}}\left(\sqrt{G_{\mathrm{d1,2}}-1}\,\hat{h}_{1,2} + \hat{v}_{1,2}\right) , \tag{3.13}$$

$$\hat{S}_{1,2} \equiv \sqrt{\frac{2}{G_{\mathrm{d1,2}}}}\hat{\xi}_{1,2} \,, \tag{3.14}$$

to simplify Eqs. (3.11)-(3.12) to

$$\hat{S}_1 = +\hat{a} + \hat{v} + \hat{V}_1^\dagger\,, \tag{3.15}$$
$$\hat{S}_2 = -\hat{a} + \hat{v} + \hat{V}_2^\dagger\,. \tag{3.16}$$

We note that the following calculations in this section are based on private discussions with Roberto Di Candia from the University of the Basque Country UPV/EHU, Spain. So far we have not included any time dependence in the expressions. To describe the dynamics of field $\hat{a}$, we define the temporal correlation functions $G^{(1)}$ and $G^{(2)}$ as

$$G^{(1)}(t, t+\tau) \equiv \langle \hat{a}^\dagger(t)\hat{a}(t+\tau)\rangle\,, \tag{3.17}$$
$$G^{(2)}(t, t+\tau) \equiv \langle \hat{a}^\dagger(t)\hat{a}^\dagger(t+\tau)\hat{a}(t+\tau)\hat{a}(t)\rangle\,. \tag{3.18}$$

Based on the fact that the first moments of the added noise are zero $\langle \hat{V}_1\rangle = \langle \hat{V}_2\rangle = 0$ and $\hat{v}$ represents a vacuum state, it is easy to get

$$G^{(1)}(t, t+\tau) = -\langle \hat{S}_1^\dagger(t)\hat{S}_2(t+\tau)\rangle + \langle \hat{V}_1(t)\hat{V}_2^\dagger(t+\tau)\rangle \tag{3.19}$$
$$= +\langle \hat{S}_1^\dagger(t)\hat{S}_1(t+\tau)\rangle - \langle \hat{V}_1(t)\hat{V}_1^\dagger(t+\tau)\rangle \tag{3.20}$$
$$= +\langle \hat{S}_2^\dagger(t)\hat{S}_2(t+\tau)\rangle - \langle \hat{V}_2(t)\hat{V}_2^\dagger(t+\tau)\rangle\,. \tag{3.21}$$

The method for calculating $G^{(2)}(t, t+\tau)$ is similar. Since this procedure is lengthy, the final expressions will not be listed here. It turns out that 160 moments of the form $\langle I_1^{j'}(t+\delta)I_2^{k'}(t+\delta)Q_1^{m'}(t+\delta)Q_2^{n'}(t+\delta)\rangle$, where $j', k', m', n' \in \mathbb{N}_0$, $0 < j'+k'+m'+n' \leq 4$, and $\delta = 0$ or τ, are needed to include all the expressions of $G^{(2)}(t, t{+}\tau)$. As already mentioned in Sec. 2.1, for a quantum mechanical treatment, the notations $\hat{p}$ and $\hat{q}$ are used to denote in-phase and out-of-phase components of a signal, while for microwave engineering the notations I and Q are used. $I_{1,2}$ and $Q_{1,2}$ are measured quantities of the operators $\hat{p}_{1,2}$ and $\hat{q}_{1,2}$. Compared to the reference state method, which is discussed in the next section, this method does not require a reference measurement. Instead, it requires the knowledge of the beam splitter relations. The dual-path method allows to characterize the properties of the beam splitter input states, whilst the reference state method describes the beam splitter output states.

3.2.2 Correlation functions of two-mode squeezed states

Next, we calculate the correlation functions which characterize the quantum correlations of the EPR pair when a time offset exists between two modes. The correlation function is a crucial parameter in quantum teleportation (Sec. 3.3) and remote state preparation (Sec. 3.4) protocols, because it sets the delay threshold before the linear transformation in Bob's side.

Two modes with bosonic annihilation operators $\hat{s}_{\mathrm{a,b}}$ pass the detection chains with effective gain $G_{\mathrm{r1,r2}}$(Fig. 3.1(b)). Based on the amplifier relation (Eq (3.9)) and IQ-mixer relation (Eq. (3.10)), the detected quadrature components, $\hat{p}_{1,2}$ and $\hat{q}_{1,2}$, in the form of complex envelope operators, $\hat{\xi}_{1,2} \equiv \hat{p}_{1,2} + \mathrm{i}\hat{q}_{1,2}$, are written as

$$\hat{\xi}_1(t) = \sqrt{G_{\mathrm{r1}}}\hat{s}_{\mathrm{a}}(t) + \sqrt{G_{\mathrm{r1}} - 1}\hat{h}_1^\dagger(t) + \hat{v}_1^\dagger(t)\,, \tag{3.22}$$

$$\hat{\xi}_2(t) = \sqrt{G_{\mathrm{r2}}}\hat{s}_{\mathrm{b}}(t) + \sqrt{G_{\mathrm{r2}} - 1}\hat{h}_2^\dagger(t) + \hat{v}_2^\dagger(t)\,, \tag{3.23}$$

where $\hat{h}_{1,2}^\dagger$ and $\hat{v}_{1,2}^\dagger$ are creation operators of the noise added by the amplifiers and IQ-mixers, respectively. In the case of a two-mode squeezed state generated by a beam splitter, $\hat{s}_{\mathrm{a,b}}$ represent the output modes of the beam splitter. To simplify the equations, we define

$$\hat{V}_{1,2}(t) \equiv \sqrt{\frac{1}{G_{\mathrm{r1,2}}}}\left(\sqrt{G_{\mathrm{r1,2}} - 1}\,\hat{h}_{1,2}(t) + \hat{v}_{1,2}(t)\right)\,, \tag{3.24}$$

$$\hat{S}_{1,2}(t) \equiv \sqrt{\frac{1}{G_{\mathrm{r1,2}}}}\hat{\xi}_{1,2}(t)\,. \tag{3.25}$$

With these definitions, Eqs. (3.22)-(3.23) read as

$$\hat{S}_1(t) = \hat{s}_{\mathrm{a}}(t) + \hat{V}_1^\dagger(t)\,, \tag{3.26}$$

$$\hat{S}_2(t) = \hat{s}_{\mathrm{b}}(t) + \hat{V}_2^\dagger(t)\,. \tag{3.27}$$

Since $\langle \hat{V}_1 \rangle = \langle \hat{V}_2 \rangle = 0$, the first moments are

$$\langle \hat{s}_{\mathrm{a}}(t) \rangle = \langle \hat{S}_1(t) \rangle\,, \tag{3.28}$$

$$\langle \hat{s}_{\mathrm{b}}(t) \rangle = \langle \hat{S}_2(t) \rangle\,, \tag{3.29}$$

and the second moments are

$$\langle \hat{s}_{\rm a}(t)\hat{s}_{\rm b}(t+\tau)\rangle = \langle \hat{S}_1(t)\hat{S}_2(t+\tau)\rangle - \langle \hat{V}_1^\dagger(t)\hat{V}_2^\dagger(t+\tau)\rangle\,, \tag{3.30}$$

$$\langle \hat{s}^2_{\rm a,b}(t)\rangle = \langle \hat{S}^2_{1,2}(t)\rangle - \langle \hat{V}^{\dagger 2}_{1,2}(t)\rangle\,, \tag{3.31}$$

$$\langle \hat{s}^\dagger_{\rm a,b}(t)\hat{s}_{\rm a,b}(t)\rangle = \langle \hat{S}^\dagger_{1,2}(t)\hat{S}_{1,2}(t)\rangle - \langle \hat{V}_{1,2}(t)\hat{V}^\dagger_{1,2}(t)\rangle\,, \tag{3.32}$$

$$\langle \hat{s}^\dagger_{\rm a,b}(t+\tau)\hat{s}_{\rm a,b}(t+\tau)\rangle = \langle \hat{S}^\dagger_{1,2}(t+\tau)\hat{S}_{1,2}(t+\tau)\rangle - \langle \hat{V}_{1,2}(t+\tau)\hat{V}^\dagger_{1,2}(t+\tau)\rangle\,. \tag{3.33}$$

The conjugate terms have a similar form. For two-mode squeezed vacuum states, the variances of the superposition quadrature operators (Eq. (3.3)) characterize quantum correlations. Here, we need to add a time offset τ in one chain. The variances of superposition quadrature operators of the modes under study become

$$\left(\Delta[\hat{Q}_{(\rm a,b)}(t,t+\tau)]\right)^2 = \left(\Delta\left[\frac{1}{\sqrt{2}}\left(\hat{q}_{\rm a}(t)+\hat{q}_{\rm b}(t+\tau)\right)\right]\right)^2\,, \tag{3.34}$$

$$\left(\Delta[\hat{P}_{(\rm a,b)}(t,t+\tau)]\right)^2 = \left(\Delta\left[\frac{1}{\sqrt{2}}\left(\hat{p}_{\rm a}(t)+\hat{p}_{\rm b}(t+\tau)\right)\right]\right)^2\,. \tag{3.35}$$

Here, $\hat{p}_{\rm a,b}$ and $\hat{q}_{\rm a,b}$ are the quadratures of the $\hat{s}_{\rm a,b}$, and they fulfill

$$\hat{p}_{\rm a,b} = \frac{1}{2{\rm i}}\left(\hat{s}_{\rm a,b} - \hat{s}^\dagger_{\rm a,b}\right) \quad \text{and} \quad \hat{q}_{\rm a,b} = \frac{1}{2}\left(\hat{s}_{\rm a,b} + \hat{s}^\dagger_{\rm a,b}\right)\,. \tag{3.36}$$

The noise moments are calculated from a reference measurement which requires uncorrelated vacuum states at the beam splitter outputs. This can be easily realized by sending vacuum states into the beam splitter. This method does not rely on the beam splitter relation and treats the beam splitter as a black box.

3.3 Quantum teleportation

In 1993, C. H. Bennett et al. [8] proposed a teleportation protocol for discrete variables based on a classical communication channel and an EPR channel. This proposal has triggered lots of investigations. In 1997, the first experimental realizations [10, 11] of quantum teleportation succeeded in teleporting an optical photon polarization state. Theoretical protocols on how to teleport a quantum state of a system with continuous variables were proposed by L. Vaidman [12] and S. L. Braunstein et al. [13]. This protocol was also generalized to teleport multimode continuous variables [69]. Teleportation of coherent states in the optical domain was demonstrated in 1998 [14]. There were also other experiments on teleporting nonclassical wave packets [15] and teleportation network [70]. The rapid improvement of techniques in the optical domain makes the quantum teleportation in free space [16–18] a reality. There are also reports on quantum teleportation for cold atoms [71–73]. Because of the technical difficulties in the microwave domain, such as the lack of single microwave photon detector, so far only quantum teleportation of discrete variables has been demonstrated [38]. Quantum teleportation with continuous variables in the microwave domain has not yet been realized. In this section, we present a quantum teleportation protocol for propagating microwave signals [74].

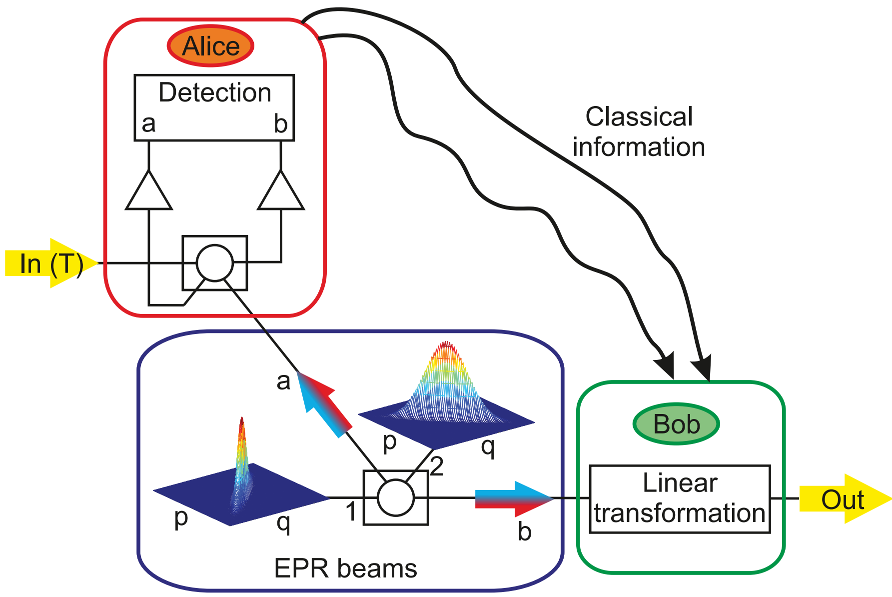

Figure 3.2: Schematic of a quantum teleportation protocol with propagating microwaves. An EPR pair (a, b) is generated by sending two squeezed state $(1, 2)$ into a $50/50$ beam splitter. The EPR pair (a, b) is distributed to Alice and Bob. Alice performs a Bell state measurement on the state to be teleported (T) and half of the EPR pair (a), and classical results a, b are obtained. Then, Alice communicates the classical results to Bob by classical communication. Bob applies a linear transformation on his half of the EPR pair (b). The output state is identical to the input state.

The protocol is schematized in Fig. 3.2. Alice and Bob are spatially separated stations. They share an EPR pair, which is, in our case, a two-mode squeezed state following relations Eq. (3.6). Half of the EPR pair is distributed to Alice, and the other half to Bob. The EPR pair is generated by sending two squeezed states into a balanced beam splitter. We emphasize that the quadrature operators $\hat{p}_{\mathrm{a,b}}$ and $\hat{q}_{\mathrm{a,b}}$ denote the beam splitter output states, and $\hat{p}_{1,2}$ and $\hat{q}_{1,2}$ the beam splitter input states. Alice wants to send an unknown quantum state, which is characterized by $\hat{p}_{\mathrm{T}}$ and $\hat{q}_{\mathrm{T}}$, to Bob. Alice first performs a Bell measurement on state T and her half of the EPR pair, and reads out a and b,

$$\hat{p}_{\mathrm{T}} + \hat{p}_{\mathrm{a}} = a \quad \text{and} \quad \hat{q}_{\mathrm{T}} - \hat{q}_{\mathrm{a}} = b\,. \tag{3.37}$$

Here, Alice only performs a local operation, and the measurement outcomes do not contain any information on the state T. After this measurement, the other half of the EPR pair in Bob's station collapses into

$$\hat{p}'_{\mathrm{b}} = \hat{p}_{\mathrm{T}} - a \quad \text{and} \quad \hat{q}'_{\mathrm{b}} = \hat{q}_{\mathrm{T}} - b\,. \tag{3.38}$$

Next, Alice communicates her measurement results, a and b, to Bob via a classical channel, and Bob applies a linear transformation to his state based on the classical information. In phase space this means, Bob displaces his state by $a + \mathrm{i}b$. In the end, the state at Bob's station is identical to the initial state to be teleported. In this protocol, the state T disappears at Alice's station and is recovered at Bob's station. This does not violate the no-cloning theorem. In reality, one needs to consider the imperfection of the EPR pair, the setup losses, the noise added by the detector, the detector efficiency, the linear transformation efficiency, the temporal mode matching, etc. Therefore, the final state at the end of the protocol is not identical to the input state. A fidelity $\mathcal{F} \equiv \langle \mathrm{in}|\hat{\rho}_{\mathrm{out}}|\mathrm{in}\rangle$ [75], which describes the similarity of the input and output states, is used to verify the protocol. Here, $\hat{\rho}_{\mathrm{out}}$ is the density operator of the output state. The maximum that can be achieved for continuous variables without any entanglement channel is $\mathcal{F} = 1/2$ [76]. A successful quantum teleportation requires $\mathcal{F} > 1/2$.

3.4 Remote state preparation

In the quantum teleportation protocol, which is discussed in the last section, Alice has no knowledge about the input state. To teleport a qubit state, the protocol requires one bit of entanglement, which is also called "ebit", and two classical bits. Both quantum and classical resources are needed, and there is no trade-off between them. If the input state is known to Alice, the protocol is called remote state preparation. In this case, there is a trade-off between the quantum and classical resources. In one limiting case, Alice encodes the input state fully into classical bits and sends them to Bob, and Bob reconstructs the state on his side. This case

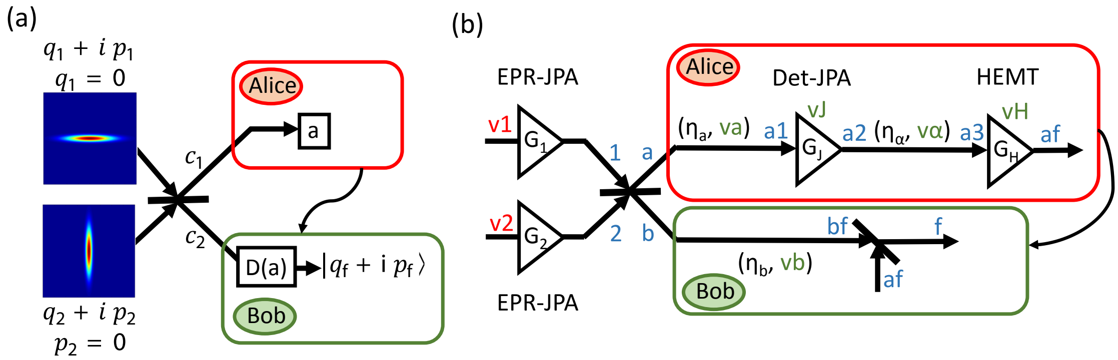

Figure 3.3: (a) Schematic of an ideal setup for remote state preparation. No loss is taken into account. Detection efficiency is one. (b) Schematic of a realistic setup for remote state preparation. Triangles represent JPAs and HEMT amplifiers. $G_{1,2}$ are the degenerate gains of the EPR-JPAs. G_J is the degenerate gain of the detection-JPA (det-JPA), and G_H is the HEMT gain. $\eta_{\mathrm{a,b},\alpha}$ denote the transmissivity of corresponding cables and connectors, and $1-\eta_{\mathrm{a,b},\alpha}$ are connection losses. All the losses and gains are in linear power units. Blue symbols are the subscripts of the states at different stages of the setup. $v1$ and $v2$ are the subscripts of the vacuum states at the inputs of the EPR-JPAs. Green symbols denote the noise added by the connection losses, det-JPA and HEMT amplifiers.

requires no entanglement resource but an infinite number of classical bits. The other extreme case is set by causality: the information transfer speed can not exceed the speed of light. Therefore, the minimal amount of classical bits needed is one. A thorough theoretical study [77] has shown that at least 3.79 ebits per qubit are required to remotely prepare a qubit state with one classical bit. Teleportation could be considered as a special case of remote state preparation. In Ref. [78], A. K. Pati has pointed out that the resources can be cut down if the input state is restricted to an ensemble of special pure qubit states. For example, an equatorial qubit state on a Bloch sphere can be remotely prepared with one classical bit and one entanglement bit. The discrete variables remote state preparation has been extended to continuous variables [79, 80]. Ref. [81] proposed a scheme to remotely prepare a squeezed state based on homodyne detection.

In this section, we present a scheme to remotely prepare a squeezed state which is compatible with microwave technology. This protocol is based on private discussions with Roberto Di Candia from the University of the Basque Country UPV/EHU, Spain. From an experimental point of view, this protocol requires the same building blocks as the quantum teleportation protocol: EPR pair generation, classical communication and linear transformation. In the teleportation protocol, a Bell measurement is needed in Alice's station, but here only a projective measurement on one quadrature is required. This significantly reduces the experimental requirements.

The protocol is sketched in Fig. 3.3. To simplify the explanation, we first consider the ideal case (Fig. 3.3(a)). This means the EPR state is an ideal two-mode squeezed vacuum state, there is no loss in the setup, and the detection efficiency is one. Therefore, no amplifier is needed in the setup for detection purposes. An ideal two-mode squeezed vacuum state is generated by sending two orthogonally squeezed states with infinite squeezing into a 50/50 beam splitter. The two input states are represented by quadrature operators $\hat{p}_{1,2}$ and $\hat{q}_{1,2}$, with $\hat{q}_1 = \hat{p}_2 = 0$. Based on the beam splitter relations (Eqs. (3.7)-(3.8)) and quadrature definitions (Eq. (2.12)), the EPR state is

$$\hat{c}_1 = \hat{q}_\mathrm{a} + \mathrm{i}\hat{p}_\mathrm{a} = \frac{1}{\sqrt{2}}[+\hat{q}_1 + \hat{q}_2 + \mathrm{i}(+\hat{p}_1 + \hat{p}_2)] = \frac{1}{\sqrt{2}}(\hat{q}_2 + \mathrm{i}\hat{p}_1)\,, \tag{3.39}$$

$$\hat{c}_2 = \hat{q}_\mathrm{b} + \mathrm{i}\hat{p}_\mathrm{b} = \frac{1}{\sqrt{2}}[-\hat{q}_1 + \hat{q}_2 + \mathrm{i}(-\hat{p}_1 + \hat{p}_2)] = \frac{1}{\sqrt{2}}(\hat{q}_2 - \mathrm{i}\hat{p}_1)\,, \tag{3.40}$$

satisfying Eq. (3.6). Alice makes a projective measurement on the p-quadrature with the result a. Now on Bob's side the state becomes $\frac{1}{\sqrt{2}}(\hat{q}_2 - \mathrm{i}a)$. Alice communicates the result to Bob, and Bob applies a displacement operator $D(\mathrm{i}a)$. In the end, Bob has $\hat{q}_\mathrm{f} + \mathrm{i}\hat{p}_\mathrm{f} = \hat{q}_2/\sqrt{2}$ on his side. At the end of the protocol, Alice has remotely prepared a state with infinite squeezing along the p-quadrature at Bob's station.

In reality, the setup is much more complicated (Fig. 3.3 (b)). According to our quadrature definitions in Eq. (2.12), the quadrature variance of a vacuum state is 0.25 (Eq. (2.26)). A two-mode squeezed vacuum state, acting as the EPR pair, is generated by a beam splitter with two squeezed states at the inputs. In experiments, a hybrid ring, which is a 50/50 beam splitter, is used to generate the EPR pair. The two squeezed states are generated using two JPAs, which are noted as EPR-JPAs in short, with degenerate power gains G_1 and G_2. If the EPR-JPAs do not add noise during amplification, the quadratures of the output states are written as

$$\hat{p_1} = \sqrt{G_1}\hat{p}_\mathrm{v1} \quad \text{and} \quad \hat{q_1} = \frac{1}{\sqrt{G_1}}\hat{q}_\mathrm{v1}\,, \tag{3.41}$$

$$\hat{p_2} = \frac{1}{\sqrt{G_2}}\hat{p}_\mathrm{v2} \quad \text{and} \quad \hat{q_2} = \sqrt{G_2}\hat{q}_\mathrm{v2}\,, \tag{3.42}$$

and the squeezed and anti-squeezed quadrature variances are $0.25/G_{1,2}$ and $0.25 \times G_{1,2}$, respectively. The operators $\hat{p}_{1,2}$ and $\hat{q}_{1,2}$ denote the EPR-JPAs' output states, which are also the squeezed states at the hybrid ring inputs. Due to the JPA losses and the connection losses between the EPR-JPAs and the hybrid ring, the quadrature variances of the squeezed states at the hybrid inputs in reality always differ from the ideal case. To include the EPR-JPAs losses and the connection losses, we use experimental quadrature variances $(\Delta X_{\mathrm{sq}})^2$ and $(\Delta X_{\mathrm{anti}})^2$, rather than $0.25/G_{1,2}$ and $0.25 \times G_{1,2}$. After the hybrid ring, the states become

$$\hat{p}_{\mathrm{a}} = \frac{\hat{p}_1 + \hat{p}_2}{\sqrt{2}}\,, \tag{3.43}$$

$$\hat{p}_{\mathrm{b}} = \frac{-\hat{p}_1 + \hat{p}_2}{\sqrt{2}}\,. \tag{3.44}$$

In the rest of the calculations, we only consider the p-quadrature, and the q-quadrature is obtained with the same method. At Alice's side, the state passes through cables, connectors and circulators with total power loss of $1 - \eta_{\mathrm{a}}$, which is included in the protocol with the beam splitter model. The state becomes

$$\hat{p}_{\mathrm{a1}} = \sqrt{\eta_{\mathrm{a}}}\hat{p}_{\mathrm{a}} + \sqrt{1 - \eta_{\mathrm{a}}}\hat{p}_{\mathrm{va}}\,. \tag{3.45}$$

Here, $\hat{p}_{\mathrm{va}}$ represents the noise added by the connection losses. Afterward, the state is projected by a detection JPA (det-JPA) with a degenerate power gain G_{J}. Here a det-JPA is used to realize low noise amplification. The state after the det-JPA becomes

$$\hat{p}_{\mathrm{a2}} = \sqrt{G_{\mathrm{J}}}\hat{p}_{\mathrm{a1}} + \sqrt{k_{\mathrm{J}}}\hat{p}_{\mathrm{vJ}}\,. \tag{3.46}$$

The term k_{J} denotes the number of noise photons added by the det-JPA at the JPA output, and $\hat{p}_{\mathrm{vJ}}$ is the quadrature operator of the noise mode. Again the state experiences a connection loss $1 - \eta_{\alpha}$ with noise term $\hat{p}_{\mathrm{v}\alpha}$,

$$\hat{p}_{\mathrm{a3}} = \sqrt{\eta_{\alpha}}\hat{p}_{\mathrm{a2}} + \sqrt{1 - \eta_{\alpha}}\hat{p}_{\mathrm{v}\alpha}\,. \tag{3.47}$$

Then a HEMT amplifier with a linear power gain G_{H} and noise $\hat{p}_{\mathrm{vH}}$ is used to further amplify the signal,

$$\hat{p}_{\mathrm{af}} = \sqrt{G_{\mathrm{H}}}\hat{p}_{\mathrm{a3}} + \sqrt{G_{\mathrm{H}} - 1}\hat{p}_{\mathrm{vH}}\,. \tag{3.48}$$

So far the state has been amplified a lot. Also a certain amount of noise has been added to the state. Now Alice measures the p-quadrature value p_{af} and communicates the result to Bob.

At Bob's side, the other half of the EPR pair travels through a cable with connection loss $1-\eta_{\mathrm{b}}$ and noise $\hat{p}_{\mathrm{vb}}$,

$$\hat{p}_{\mathrm{bf}} = \sqrt{\eta_{\mathrm{b}}}\hat{p}_{\mathrm{b}} + \sqrt{1-\eta_{\mathrm{b}}}\hat{p}_{\mathrm{vb}} \,. \tag{3.49}$$

Finally, Bob displaces the state based on the classical information from Alice. This is realized with a high transmissivity (τ) beam splitter, which is a directional coupler (Sec 2.3). Similar to Eq. (2.21), the output state is written as

$$\hat{p}_{\mathrm{f}} = \sqrt{\tau}\hat{p}_{\mathrm{bf}} + \sqrt{1-\tau}\hat{p}_{\mathrm{af}} \,. \tag{3.50}$$

If the protocol works, a state squeezed along p-quadrature is prepared at Bob's station. We use the variance of $\hat{p}_{\mathrm{f}}$ to evaluate the squeezing level of the output state. If $(\Delta\hat{p}_{\mathrm{f}}) < 0.25$, the protocol works.

$$\begin{aligned}
(\Delta\hat{p}_{\mathrm{f}})^2 =& \frac{1}{8}\tau\eta_{\mathrm{b}}\left(\frac{1}{G_2}+G_1\right) + \frac{1}{8}\left(1-\tau\right)G_{\mathrm{H}}G_{\mathrm{J}}\eta_\alpha\eta_{\mathrm{a}}\left(\frac{1}{G_2}+G_1\right) \\
&+ \frac{1}{4}\left(1-\tau\right)G_{\mathrm{H}}G_{\mathrm{J}}\eta_\alpha\left(1-\eta_{\mathrm{a}}\right) + \frac{1}{4}\left(1-\tau\right)G_{\mathrm{H}}\eta_\alpha k_{\mathrm{J}} + \frac{1}{4}\tau\left(1-\eta_{\mathrm{b}}\right) \\
&+ \frac{1}{2}(1-\tau)G_{\mathrm{H}}(1-\eta_\alpha)\left(n_\alpha+\frac{1}{2}\right) + \frac{1}{2}(1-\tau)(G_{\mathrm{H}}-1)\left(n_{\mathrm{H}}+\frac{1}{2}\right) \\
&+ \frac{1}{4}\sqrt{\tau(1-\tau)}\left(\frac{1}{G_2}-G_1\right)\sqrt{\eta_{\mathrm{b}}G_{\mathrm{H}}G_{\mathrm{J}}\eta_\alpha\eta_{\mathrm{a}}} \,.
\end{aligned} \tag{3.51}$$

Since the EPR-JPAs, det-JPA, hybrid ring and directional coupler, including the circulators, connectors and cables connecting these components, are installed at the sample stage of the dilution refrigerator, and the temperature is smaller than 50 mK, which is well below the thermal excitation temperature at our working frequency $5-6\,\mathrm{GHz}$, the noise added by the beam splitter is approximately at the vacuum level. Here we only consider the thermal photons n_α introduced by the connection loss $1-\eta_\alpha$ from the det-JPA to the HEMT amplifier, n_{H} by the HEMT amplifier, and k_{J} by the det-JPA. We emphasize that the thermal photons added by the det-JPA are not only determined by the physical temperature, but mainly by the JPA losses.

With an ideal setup, which assumes no losses ($\eta_{\mathrm{a}} = \eta_{\mathrm{b}} = \eta_\alpha = 1$) and a detection efficiency of one ($G_{\mathrm{J}} = G_{\mathrm{H}} = 1$ and $k_{\mathrm{J}} = n_\alpha = n_{\mathrm{H}} = 0$), the output state has the same squeezing level as the squeezed states generated by the EPR-JPAs, assuming that the EPR pair is balanced, $G_1 = G_2$. As long as we need to amplify the state at Alice's station, the squeezing level of the final state decreases compared to the squeezed states generated by EPR-JPAs. Tab. 3.1 shows how much squeezing is lost

Table 3.1: Comparison of the squeezing level between the hybrid ring input states and the final output states. $G_1 = G_2$ are the linear power gains of the EPR-JPAs, and G_{J} is the linear power gain of the det-JPA, $G_{\mathrm{J}} = 100$. No loss is taken into account ($\eta_a = \eta_b = \eta_\alpha = 0$). $G_{\mathrm{H}} = 20000$ and $n_{\mathrm{H}} = 7.4$, corresponding to $43\,\mathrm{dB}$ gain and $2\,\mathrm{K}$ noise temperature, are realistic values for HEMT amplifiers in the frequency range of $5-6\,\mathrm{GHz}$.

G_1	Squeezing at the hybrid inputs (dB)	Squeezing of the output state (dB)
3	4.8	1.6
10	10	4.6
50	17	7.1
90	20	7.5
130	21	7.6

using this protocol. In this calculation, the det-JPA gain, the HEMT amplifier gain, and the HEMT amplifier noise are taken into account, while the connection losses, the EPR-JPA noise and the det-JPA noise are ignored.

Based on Eq. (3.51), we can investigate the effect of different parameters on the protocol. The main results are plotted in Figs. 3.4-3.6. In Figs. 3.4(a)-(d), the connection losses are ignored $\eta_{\mathrm{a}} = \eta_{\mathrm{b}} = \eta_\alpha = 1$. $G_{\mathrm{H}} = 20000$ and $n_{\mathrm{H}} = 7.4$ are realistic values for a HEMT. Fig. 3.4(a) shows the quadrature variance $(\Delta p_{\mathrm{f}})^2$ versus transmissivity of the directional coupler. The τ value, which could balance the gains and losses in Alice's side, gives the minimal quadrature variance, and the largest squeezing level. We consider the noise of the EPR-JPAs and the det-JPA by plugging in the parameters of Q300 JPA according to Refs. [32, 39]. It is clear from the figure that both the EPR-JPAs noise and the det-JPA noise are crucial for the protocol. In Fig. 3.4(b), the squeezing level of the output state is plotted as a function of G_{J} with the other parameters fixed except τ. We choose the τ value which leads to the minimal variance. The figures shows that the squeezing level saturates as G_{J} increases. Similarly, in Fig. 3.4(c), the squeezing level of the hybrid ring input states and the final output state is plotted versus G_1. The former increases fast, while the latter increases slowly and tends to saturate. Above, we suppose the two EPR-JPAs are gain balanced, $G_1 = G_2$. In real experiments, there can be some imbalance between them. Fig. 3.4(d) shows the influence of the EPR-JPA gain imbalance on the output state.

Ideally, the two squeezed states at the hybrid ring inputs should have the squeezed quadratures with $90\,^\circ$ phase difference. This means if one is squeezed along $\tilde{\varphi}/2$, the other is squeezed along $(\tilde{\varphi}/2 + 90)\,^\circ$. In experiments, temperature and pressure fluctuations in and outside the cryostat cause phase fluctuations of the

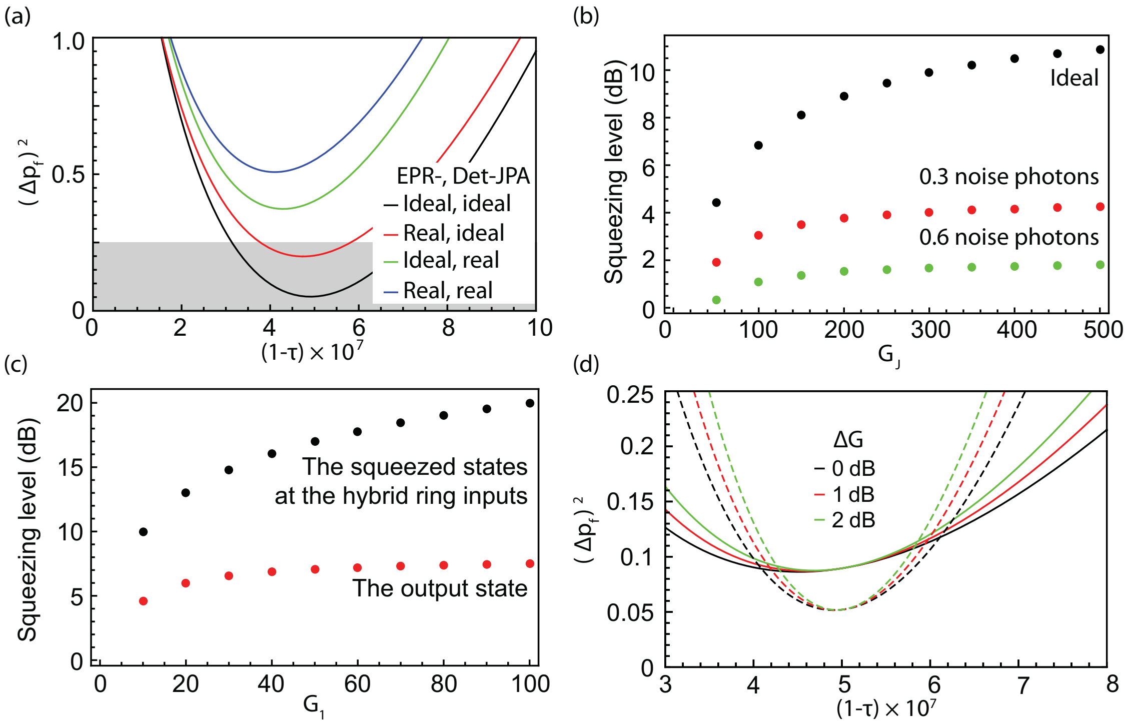

Figure 3.4: (a)-(d) $\eta_a = \eta_b = \eta_\alpha = 1$, $G_H = 20000$, and $n_H = 7.4$. (b)-(d) $n_\alpha = 4$. (a) The influence of the EPR-JPA noise and the det-JPA noise on the quadrature variance of the output state. $G_1 = G_2 = 39.8$, $G_J = 100$. "Real" stands for the cases with finite JPA noise photons, and "ideal" means zero JPA noise photons. $k_J = 140$ corresponds to 0.14 noise photons at the JPA input for anti-squeezed quadrature. $(\Delta X_{sq})^2 = 0.0813$ and $(\Delta X_{anti})^2 = 9.1378$ correspond to a degenerate gain of $G = 39.8$ on a linear scale and $10\,\mathrm{dB}$ signal gain. The values of k_J, $(\Delta X_{sq})^2$ and $(\Delta X_{anti})^2$ are from Refs. [32, 39]. The gray area indicates squeezing. (b) Squeezing level of the output state versus G_J with different det-JPA noise photons at the JPA input for the anti-squeezed quadrature. $G_1 = G_2 = 39.8$, and the EPR-JPA noise is disregarded. (c) The dependence of the squeezing level of the hybrid ring input state and the final output state on G_1. The EPR-JPAs are balanced ($G_1 = G_2$). $G_J = 100$ and $k_J = 0$. In (b) and (c), for each point the τ corresponds to a value which gives the minimal variance of the final output state. (d) The dependence of the quadrature variance of the output state on EPR-JPA gain imbalance. $G_J = 100$, $k_J = 0$ and $G_1 = G_2 + \Delta G$. $G_1 = 10$ for solid lines and $G_1 = 40$ for dashed lines.

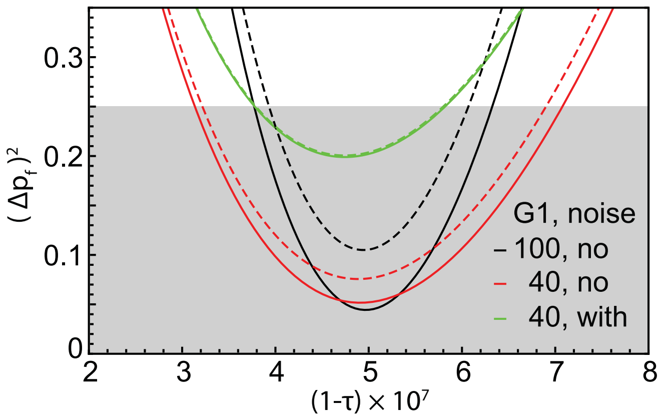

Figure 3.5: The effect of the EPR-JPAs angle error on the output state with different EPR-JPA gains G_1. $G_1 = G_2$. The angle error is 2° for the dashed lines and 0° for the solid lines. $G_\mathrm{J} = 100$. "With noise" means $\Delta X_\mathrm{sq} = 0.0813$ and $\Delta X_\mathrm{anti} = 9.1378$ for Q300 JPA with $10\,\mathrm{dB}$ signal gain [32, 39]. A degenerate gain $G = 23.4$ corresponds to $10\,\mathrm{dB}$ signal gain. $\eta_\mathrm{a} = \eta_\mathrm{b} = \eta_\alpha = 1$, $G_\mathrm{H} = 20000$, $n_\mathrm{H} = 7.4$ and $n_\alpha = 4$.

microwave signals. Also the microwave sources have phase drifts. All these instabilities can lead to a phase drift of the squeezed states, and result in an angle error of the EPR state. The angle error $\tilde{\theta}$ is used to express how much the phase difference deviates from 90°. We assume $\hat{p}_1$ is the reference and it fulfills Eq. (3.41). Then $\hat{p}_2$ becomes

$$\hat{p}_2 = \frac{\cos\tilde{\theta}}{\sqrt{G_2}}\hat{p}_{\mathrm{v}2\tilde{\theta}} - \sqrt{G_2}\hat{q}_{\mathrm{v}2\tilde{\theta}}\sin\tilde{\theta}\,, \tag{3.52}$$

where $\hat{p}_{\mathrm{v}2\tilde{\theta}}$ and $\hat{q}_{\mathrm{v}2\tilde{\theta}}$ are the quadrature operators of the vacuum state with the squeezed and anti-squeezed quadrature phase, respectively. Then, Eq. (3.51) becomes

$$\begin{aligned}(\Delta\hat{p}_\mathrm{f})^2 =& \frac{1}{8}\tau\eta_\mathrm{b}\left(\frac{\cos^2\tilde{\theta}}{G_2} + G_1 + G_2\sin^2\tilde{\theta}\right)\\ &+ \frac{1}{8}\left(1-\tau\right)G_\mathrm{H}G_\mathrm{J}\eta_\alpha\eta_a\left(\frac{\cos^2\tilde{\theta}}{G_2} + G_1 + G_2\sin^2\tilde{\theta}\right)\\ &+ \frac{1}{4}\left(1-\tau\right)G_\mathrm{H}G_\mathrm{J}\eta_\alpha\left(1-\eta_\mathrm{a}\right) + \frac{1}{4}\left(1-\tau\right)G_\mathrm{H}\eta_\alpha k_\mathrm{J} + \frac{1}{4}\tau\left(1-\eta_\mathrm{b}\right)\\ &+ \frac{1}{2}(1-\tau)G_\mathrm{H}(1-\eta_\alpha)\left(n_\alpha + \frac{1}{2}\right) + \frac{1}{2}(1-\tau)(G_\mathrm{H}-1)\left(n_\mathrm{H} + \frac{1}{2}\right)\\ &+ \frac{1}{4}\sqrt{\tau(1-\tau)}\left(\frac{\cos^2\tilde{\theta}}{G_2} - G_1 + G_2\sin^2\tilde{\theta}\right)\sqrt{\eta_\mathrm{b}G_\mathrm{H}G_\mathrm{J}\eta_\alpha\eta_\mathrm{a}}\,.\end{aligned} \tag{3.53}$$

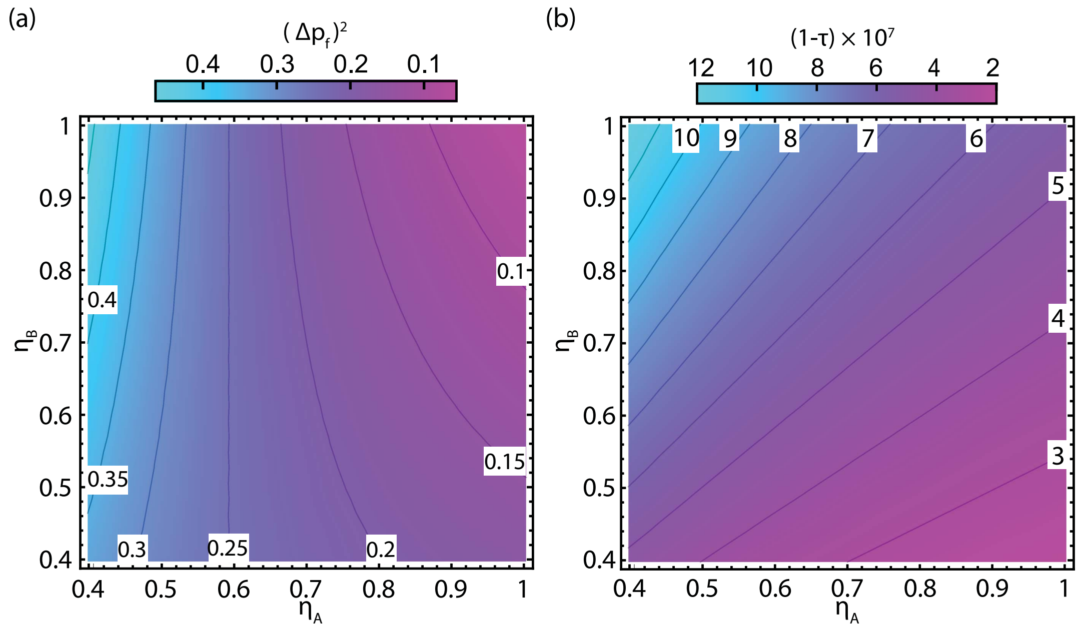

Figure 3.6: (a) Color plot of $(\Delta\hat{p}_\mathrm{f})^2$ versus η_A and η_B. (b) Color plot of $(1-\tau)\times 10^7$ of (a). The numbers on the plot are the values of $(\Delta\hat{p}_\mathrm{f})^2$ for (a) and $(1-\tau)\times 10^7$ for (b). $G_1 = G_2 = 40$, $G_\mathrm{J} = 100$, $\eta_\mathrm{a} = \eta_\mathrm{b} = \eta_\alpha = 1$, $G_\mathrm{H} = 20000$, $n_\mathrm{H} = 7.4$, $k_\mathrm{J} = 0$, $\eta_\alpha = 0.9$, and $n_\alpha = 4$.

In Fig. 3.5 the effect of the angle error of the squeezed state generated by EPR-JPAs is shown. For higher degenerate gains, which means more squeezing, the angle error becomes more problematic.

So far we have ignored the connection losses, assuming $\eta_\mathrm{a} = \eta_\mathrm{b} = \eta_\alpha = 1$. Now we investigate the influence of connection losses. Fig. 3.6(a) shows that mainly η_A determines the maximal squeezing level. When the parameters for the det-JPA (G_J, k_J), the HEMT amplifier (G_H, n_H), and other connection losses at Alice's side (η_α, n_α) are fixed, there is a threshold η_Ath for η_A. If $\eta_\mathrm{A} > \eta_\mathrm{Ath}$, which means less losses, the output state is squeezed for an optimum τ. When the losses at Bob's side are zero ($\eta_\mathrm{B} = 1$), the maximal squeezing level, which is set by η_A, is reached. More losses at Bob's side mean more vacuum state contributes to the final quantum state. As long as $\eta_\mathrm{B} \neq 0$, the state is still squeezed below vacuum. Larger η_B needs smaller τ to balance the magnitude of the quantum state and the coherent state. If $\eta_A < \eta_{Ath}$, the p-quadrature variance of the output state is always larger than 0.25. If $\eta_\mathrm{A} = \eta_\mathrm{Ath}$, the p-quadrature variance of the output state equals 0.25.

Chapter 4

Experimental techniques

In this work, we have investigated mainly 3 flux-driven JPAs, which are denoted as Q600 JPA, Q300 JPA and Q200 JPA [1]. In this chapter, the experimental setups and techniques are discussed. Here we describe the assembly of the cryogenic setup: microwave input and output lines, DC lines, sample preparation. Next, we discuss the room temperature setup, including IQ cross-correlation detection, data acquisition and processing methods used in the experiments.

4.1 Cryogenic setups

The frequency of the microwave signals we study in this work is around 6 GHz, corresponding to a temperature of 300 mK. To investigate the quantum properties of microwave signals, an environmental temperature well below 300 mK is required to suppress perturbations from thermal excitations. Also, the generation of quantum microwaves is performed using superconducting circuits. In our case, JPAs, which are based on Nb and Al thin films on a Si substrate, are used to generate squeezed states. Although the critical temperature of Nb and Al is 9.2 K and 1.2 K, respectively, a temperature well below the critical temperature reduces the amount of quasiparticles in superconductors. Therefore, we use ^{3}He/^{4}He-dilution refrigerators to reach the required temperatures of a few 10 mK. The experiments on Q300 JPA are conducted in a liquid helium precooled ^{3}He/^{4}He-dilution refrigerator [40]. In the following the cryogen-free ^{3}He/^{4}He-dilution refrigerator is described which

[1] The notation for the JPA samples are based on the designed external quality factors, not the measured $Q_{\rm ext}$. By simultaneous fitting of phase and magnitude of the transmission spectra to a theoretical model [64], the calculated $Q_{\rm ext}$ of Q600, Q300, Q200 JPAs are 12000, 300 and 280, respectively. The calculated internal quality factors $Q_{\rm int}$ of Q600 JPA is between 1000 and 1500, $Q_{\rm int}$ of Q300 JPA is between 5000 and 10000, and $Q_{\rm int}$ of Q200 JPA is between 1000 and 2000.

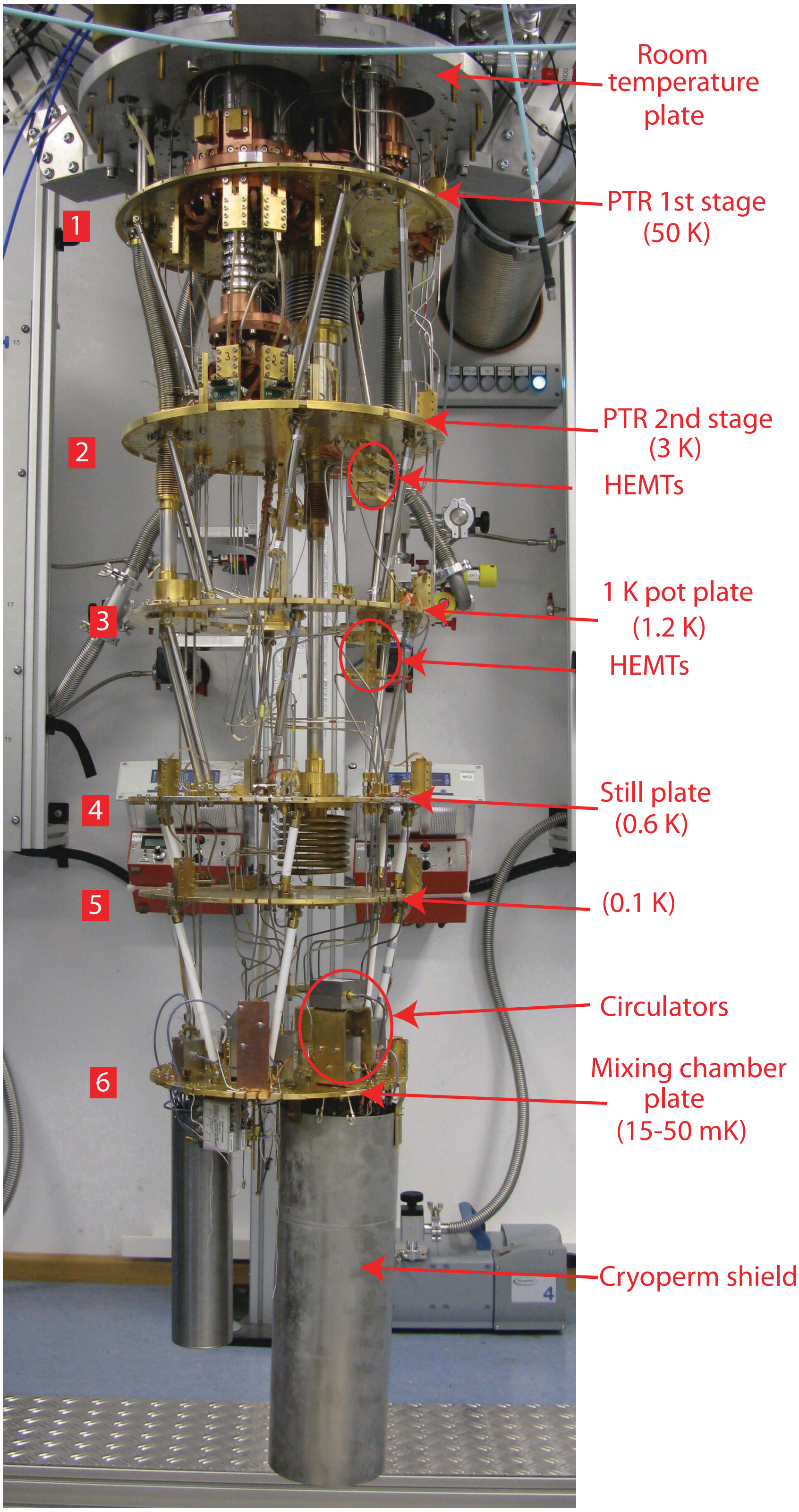

Figure 4.1: Photograph of the cryogenic setup for measurements with Q600 and Q200 JPAs. PTR: pulse tube refrigerator.

has been used for the experiments on the Q200 and Q600 samples.

This dilution refrigerator is designed and constructed at the Walther-Meißner-Institut by K. Uhlig, A. Marx, T. Brenninger, S. Höss, and our workshop team. There are 6 temperature stages (Fig. 4.1). A two-stage Pulse Tube Refrigerator (PTR) cools the first and second stages to 50 K and 3 K, respectively. To cool microwave components (e.g. cables, amplifiers and circulators), the dilution refrigerator is equipped with a separate ^{4}He-1 K loop which offers a cooling power up to 100 mW near 1 K at the third stage. The still chamber of the dilution refrigerator sets the temperature of the fourth stage to around 700 mK. Below the still stage, there are one continuous and two step heat exchangers. The first step exchanger is mounted to the fifth temperature stage at around 100 mK. The mixing chamber is bolted to a large copper plate which defines the lowest stage temperature. In the present setup, the dilution unit reaches a lowest temperature around 11 mK and the cooling power at 100 mK is about 300 μW. More details about the cryostat, can be found in Refs. [82, 83].

In the following, we discuss the input lines, the sample preparation, the millikelvin stage, the output and DC lines in detail. We present the most recent setups for the millikelvin stage and the output lines. However, not all the experimental results presented in Chapter 5 and Chapter 6 have been measured with the most recent setups. For example, some results are obtained with a setup without a cryoperm shield. The difference between the actual setup and the setup presented in this chapter is noted if this difference is essential for the discussion of the measurement results.

4.1.1 Input lines

Since the losses in the input losses are not crucial for the measurements, stainless steel cables manufactured by Coax Co., Ltd with a specified loss of 9.44 dB per meter at 5 GHz are used for the input lines. The SMA connectors are soldered manually to these cables. During the soldering process and the subsequent thermal circling inside the cryostat, the dielectric expands and shrinks, resulting in the movement of the inner conductors due to different thermal expansion coefficients of the dielectric and conductors. To prevent a potential damage of the SMA connectors, the cables are thermally cycled to liquid N_2 temperatures several times before soldering, and bended (Fig. 4.3(a)) to reduce movements of the inner conductors. They are connected to attenuators, which are mounted on top of the feedthroughs on the different temperature plates. In this way, both the inner and outer conductors of the cables

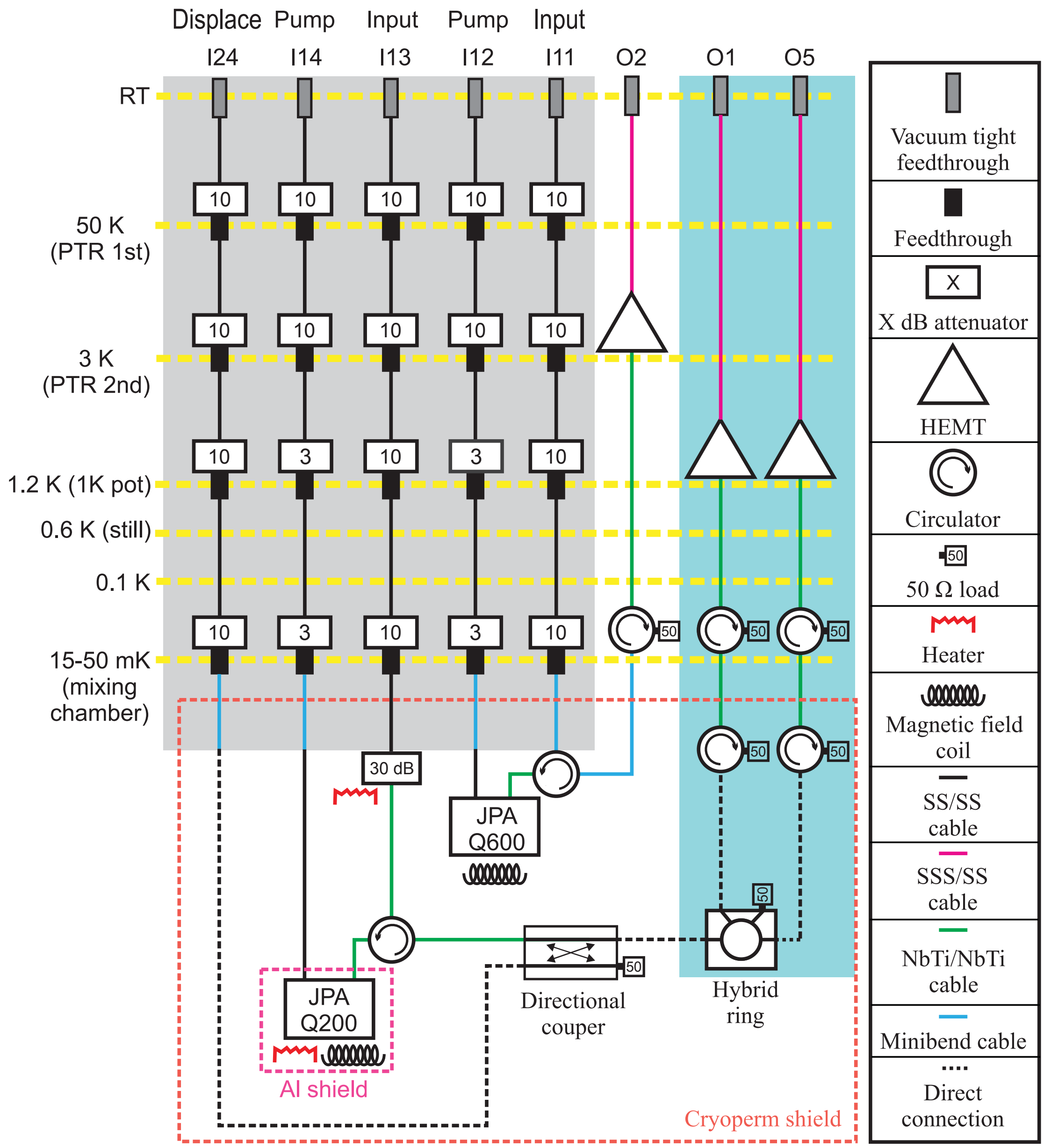

Figure 4.2: Schematic of the cryogenic setup for measurements with Q600 and Q200 JPAs. The blue region indicates the cryogenic part of the dual-path receiver (Sec 4.2.1). Losses of the input lines inside the gray area (from room temperature down to millikelven temperature) are shown in Fig. 4.3. RT: room temperature; SS: stainless steel, SSS: silver plated stainless steel. Minibend cables are ruggedized flexible coaxial cables with silver plated copper as an inner conductor, and stainless steel as an outer conductor. Female-female adapters between two cables are omitted. Input lines I14, I12 are for pump signals, I13, I11 are for input signals, and I24 is for displacement signals.

are thermalized.

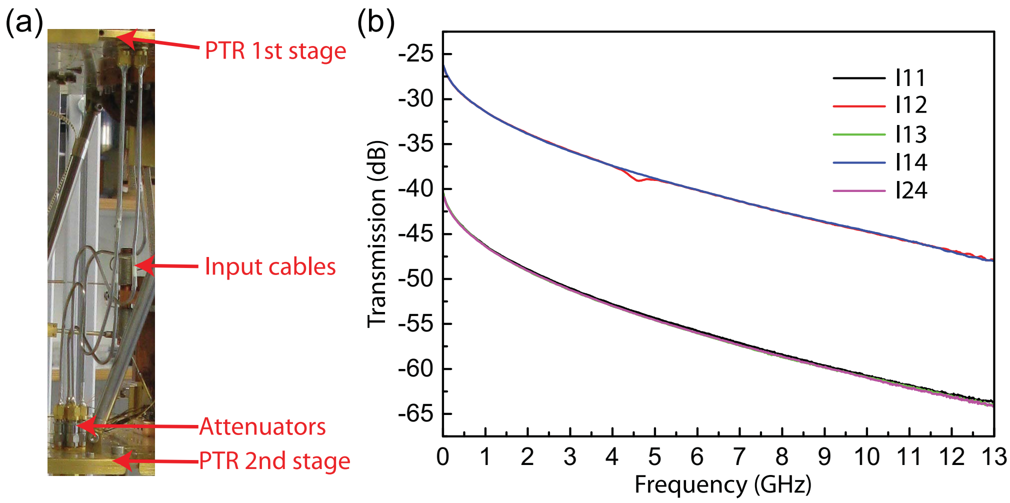

Figure 4.3: (a) Photograph of input cables between PTR 1st and 2nd stages. (b) Transmissions of input cables in the gray region in Fig. 4.2 measured at room temperature.

The losses of the input lines in the gray region in Fig. 4.2 measured at room temperature are shown in Fig. 4.3(b). The JPA pump lines (I11, I12) have 14 dB less attenuation than the other input lines, since the required power for the pump signal is much higher. Each JPA signal line (I13, I11) is connected to a measurement circulator, and the output signal which is reflected back from the JPA signal port is directed to the microwave outputs lines by the measurement circulator. Since the cable between the measurement circulators and the JPAs are also a part of the output lines, NbTi/NbTi-superconducting cables [2] are used to reduce the connection losses. At the Q200 JPA signal input, a 30 dB-attenuator is installed. Additionally, a heater and a silver wire, which is weakly coupled to the mixing chamber plate, are attached to this attenuator. Thus its temperature can be controlled over a wide range (50 – 800 mK) without heating up the rest of the mixing chamber components. By sweeping the temperature of the 30 dB-attenuator, we can calibrate the gain of the whole detection chains (Sec. 6.1.1, 6.2.1). To minimize the connection losses and thermal coupling between the 30 dB-attenuator and the JPA, a NbTi/NbTi-superconducting cable is used.

[2] NbTi/NbTi indicates the material of the inner and outer conductor.

4.1.2 Sample preparation

The JPA samples have been designed and fabricated by T. Yamamoto and K. Inomata in the group of Y. Nakamura at NEC Smart Energy Research Laboratories, Japan. An optical micrograph of the Q200 JPA is shown in Fig. 4.4. The resonator and antenna are patterned from a sputtered 50 nm thick Nb film. As substrate we use thermally oxidized (300 nm) silicon with a thickness of 300 µm. In the last step, the Al dc SQUID is fabricated using shadow evaporation [61]. Each Al electrode has a thickness of 50 nm. The sample layout for Q600 and Q200 JPA are the same. For Q300 JPA, 95 nm of gold is deposited on top of a 5 nm Ti bonding layer at the contacts. The optical micrograph of Q300 JPA is presented in Ref. [32].

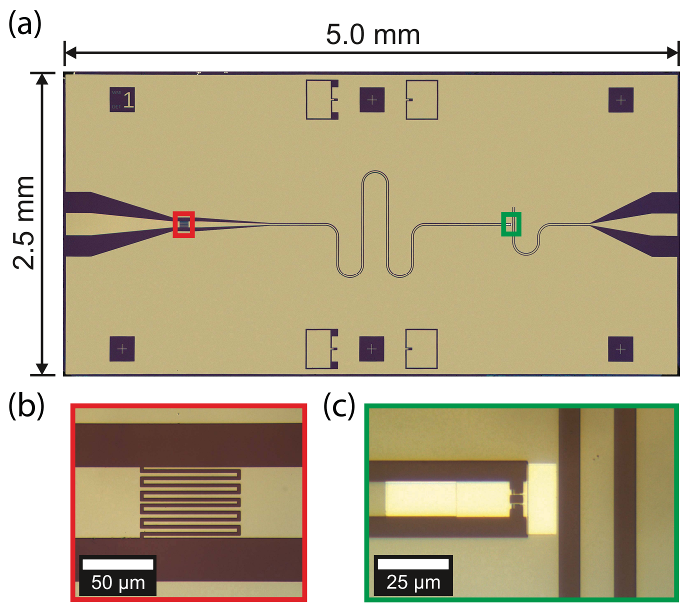

Figure 4.4: Flux driven JPA (Q200 JPA) used in our experiments. (a) Optical micrograph of the chip. Red rectangle: coupling capacitor. Green rectangle: dc SQUID and pump line. (b) Zoom-in of the coupling capacitor marked with the red rectangle in panel (a). (c) dc-SQUID and pump line in the region marked with the green rectangle in panel (a). The size of the SQUID loop is $4.2 \times 2.4\,\mu\mathrm{m}^2$.

The JPA samples are glued into the sample box with GE-vanish, and the sample ground planes are connected to the box and the Printed Circuit Boards (PCBs) by Al wires (Fig. 4.5(a)). The Al wires are pressed to the desired positions with an ultrasonic bonding machine. The PCBs, which transfer the coplanar to the coaxial configuration, contain a piece of CPW. One side of the CPW is connected to the sample by Al bonds, and the other side is soldered to the center pin of a glass bead (V-110) from Anritsu. The PCBs are grounded to the box by Al bonds. Male V-

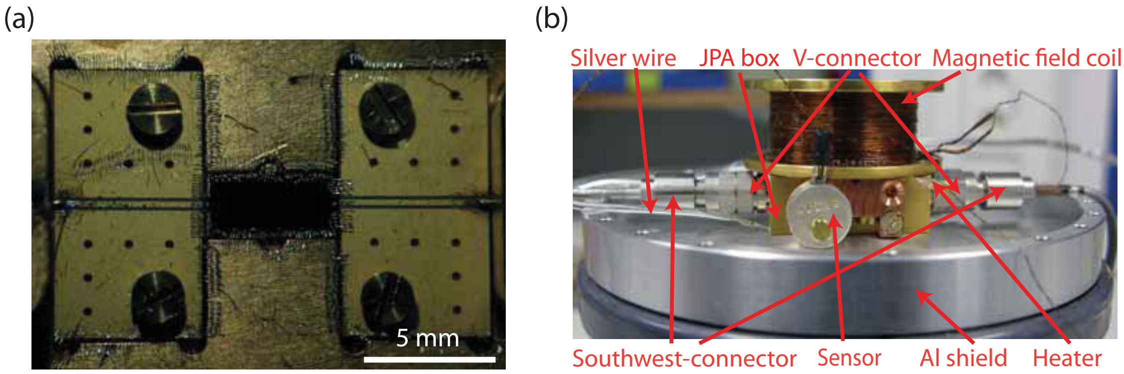

Figure 4.5: (a) Photograph of the Q200 JPA in a side-mounted sample box. The sample is bonded, using an ultrasonic bonding machine, with Al wires. (b) Photograph of the sample box for Q200 JPA inside an Al shield. The Al cover of the shield is not shown. A heater and a sensor are attached to the sample box. A magnetic field coil made of a NbTi wire is mounted on top of the sample box. Two silver wires thermally connect the sample box to a silver rod. SMA connectors ($2.4\,\mathrm{mm}$, from Southwest) match the V-connectors.

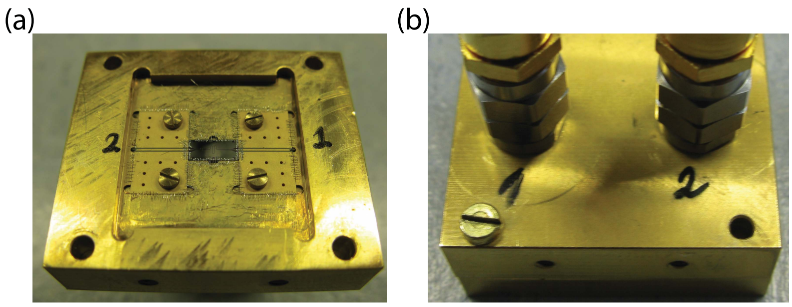

Figure 4.6: Photograph of Q600 JPA in a top-mounted sample box. (a) Top view. (b) Bottom view.

connectors (V102MR) from Anritsu are installed at the box to connect the glass beads. The Q200 JPA is mounted into a side-mounted sample box (Fig. 4.5), while the Q600 JPA is mounted into a top-mounted sample box (Fig. 4.6). Details on the PCBs, glass beads, V-connectors and sample boxes are given in Ref. [64].

As depicted in Fig. 4.5(b), a magnetic field coil is placed on top of the sample box to provide an external flux through the SQUID. A temperature sensor and heater are used for PID control of the sample temperature. Two silver wires provide thermal connection to a silver rod where the sample and most of the other microwave components are installed. This silver rod is thermally anchored to the mixing chamber plate. The sample box, magnetic field coil, heater and sensor are placed inside an Al shield to provide screening of external magnetic fields. The Al shield is placed inside a cryoperm shield (Fig. 4.1).

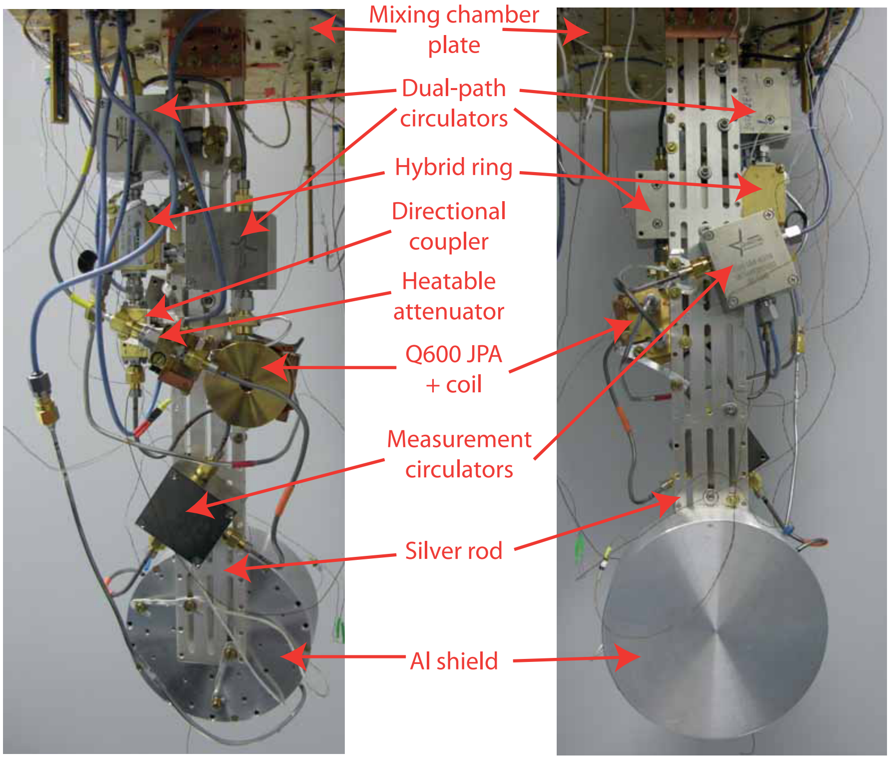

Figure 4.7: Front and rear views of the silver rod attached to the mixing chamber plate with the corresponding components.

4.1.3 Millikelvin stage

The JPA samples and most of the microwave components at the millikelvin stage are installed on a silver rod, which is fixed to the mixing chamber plate (see Fig. 4.7). The silver rod is additionally thermalized by silver wires to the mixing chamber plate. A circulator in front of each JPA sample is used to separate incoming from outgoing microwaves. We call this circulator the "measurement circulator" to distinguish it from other circulators in the setup. Since the Q600 JPA is not used for squeezing measurements, its measurement circulator is directly connected to the output line. Q200 JPA has been used for squeezing and displacement measurements, and it is connected to a dual-path receiver. Between the dual-path receiver and the measurement circulator a directional coupler is installed. The directional coupler acts as a transmission line with a vacuum signal incident at the coupled port, while it applies a displacement operation to the input signal with a coherent signal at the coupled port. The transmitted port of the directional coupler is connected to a customized hybrid ring. For details on hybrid rings, it is referred to Refs. [40, 84]. Compared with the hybrid ring used for measurements with Q300 JPA, which is described in Refs. [39, 40], the hybrid ring for Q200 JPA has a slightly different geometry. The connectors have the proper gender which directly matches the connecting parts of the directional coupler and circulators. The second input of the hybrid ring is terminated with a 50 Ω load, and this 50 Ω load can be connected directly to the hybrid ring without additional interconnects. The hybrid ring's two outputs are connected to the dual-path circulators and the outputs of the latter are further connected to the microwave output lines, as shown in Fig. 4.2 and Fig. 4.7.

The components are thermalized by firmly bolting them to the silver rod. For some free hanging components and 50 Ω loads, silver wires are used for thermal anchoring. To increase the thermal conductivity of the silver wires, we process them as follows. First, they are bent to the exact desired shape, and then annealed at 900 °C for one hour. In the end, they are installed without further bending.

4.1.4 Output lines

The losses between the JPA sample and the first amplifier, a HEMT amplifier in this case, can significantly reduce the signal-to-noise ratio. Therefore, NbTi/NbTi-superconducting cables are used for the corresponding connections. We have investigated several ways to mount SMA connectors on this kind of cable, and the main results are summarized in Tab. 4.1. Based on the mechanical stability, the impedance missmatch and the complexity to make connectors, we choose type-III connectors (crimped type) for most of our purposes. In Fig. 4.8 the losses of a thick (2.19 mm diameter) and thin (1.19 mm diameter) NbTi/NbTi cable of 1 m length with type-III and IV connectors, respectively, measured at 3 K are shown. As shown in Fig. 4.8(a), the cable is bent into circles to fit into the refrigerator. A five-port switch is used to calibrate the input and output lines. At position A of the switch a calibration is done, while at position B the cable is measured. The linear fits are used to estimate the losses. The thin cable has a larger loss (0.23 dB per meter at 6 GHz) than the thick cable (0.16 dB per meter at 6 GHz). The regularly spaced peaks with a separation of about 216 MHz are due to reflections at the connectors. The power of the peaks can be suppressed by reducing the impedance mismatch.

Unlike the input lines, where the cables are fixed and thermalized by attenuators, the cables in the output lines are fixed and thermalized by copper braids or silver wires at each temperature stage. To block thermal noise and microwave reflections coming from higher temperature stages, additional circulators are installed for each output line at the mixing chamber plate. They are fixed and thermalized by copper holders, and further thermalized by 50 Ω-loads at the unused ports. The cables are

Table 4.1: Summary of different types of SMA connectors on NbTi/NbTi cables.

	Model company	Outer diameter	Connection method	Machanical stability	Impedance miss-match	Complexity
I	SMA Huber+Suhner	2.19 mm	Soldered*	good	$> 2\,\Omega$	High
II	SMA Huber+Suhner	2.19 mm	ECCOBOND glued	bad	$> 2\,\Omega$	Low
III	SMA Radiall	2.19 mm	Crimped	good	$\approx 2\,\Omega$	Low
IV	SMA Southwest microwave	1.19 mm	Soldered*	good	$> 2\,\Omega$	High

(*): There are three main steps before soldering onto NbTi/NbTi cables.

1. Mechanical polishing.
2. 1-2 minutes cleaning in the mixture $HF/HNO_3/H_2O/CH_3COOH$ with a ratio $1:6:10:2$.
3. Electroplating for about 8 minutes in the mixture $H_2O/CuSO_4/H_2SO_4$ with a ratio $40:8:1$. Current is set to $60\,\mathrm{mA}$.

connected to the circulators and HEMT amplifiers, which also provide thermalization for the cables. HEMT amplifiers are installed onto the $3\,\mathrm{K}$ and $1.2\,\mathrm{K}$ plates. The amplification is based on high electron mobility transistors, and this process adds $5-20$ noise photons to the input signal [22, 23]. The power supply of the HEMT amplifiers is temperature stabilized within $\pm 0.2\,^\circ\mathrm{C}$.

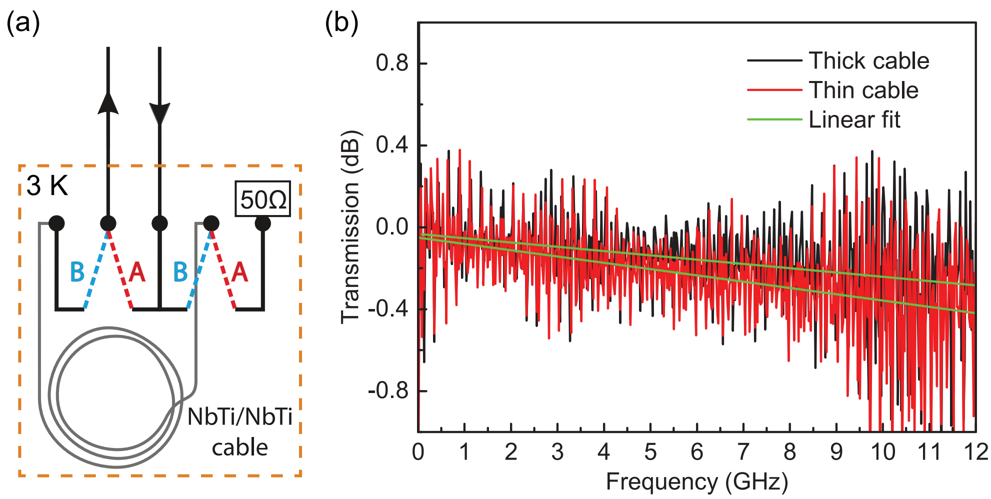

Figure 4.8: (a) Schematic of a cable loss measurement setup. When the microwave switch is at position A, a transmission calibration is performed. At position B, the NbTi/NbTi cable is measured. (b) The losses of one meter NbTi/NbTi cable with an outer diameter of $2.19\,\mathrm{mm}$ and type III connectors (crimp connectors), and one meter NbTi/NbTi cable with an outer diameter of $1.19\,\mathrm{mm}$ and type IV connectors (southwest connectors) measured at $3\,\mathrm{K}$.

4.1.5 DC lines

DC lines have been used for powering of the magnetic field coils, heaters, HEMT amplifiers and switches. At temperatures above 3 K , beryllium-copper looms are used. Below 3 K , superconducting NbTi wires have been used. The ends of the DC wires are fixed and thermalized to the plates by connectors as shown in Fig. 4.9(a). As the DC wires pass through each plate, they are pressed between two copper plates with thermal grease in between to enhance thermalization (Fig. 4.9(b)). Kapton foils are wrapped around the wires to avoid any damage from the copper plates.

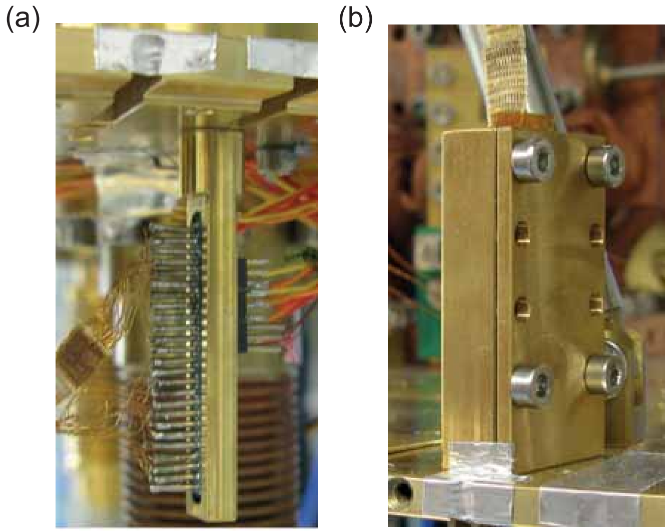

Figure 4.9: (a) Photograph of a connector for DC wires inside the refrigerator. (b) Photograph of the thermal anchor for DC wires at different temperature stages.

4.2 Room temperature setups

The room temperature setup for the Q600 JPA is shown in Fig. 4.10. A microwave source provides a pump signal at around 12 GHz . For microwave sources, whose base band frequency $f_{\text{pump}}/2$ for a pump signal is not properly filtered, filters are needed at the source output. The input signals are supplied by either a microwave source or a Vector Network Analyzer (VNA). The signals coming out of the cryostat are further amplified with room temperature amplifiers, whose temperature is stabilized by a peltier cooler and PID controller. Then the signal is detected by either a VNA or a spectrum analyzer.

In addition to the setup for Q600 JPA, the setups for Q200 and Q300 JPAs also contain dual-path receivers. The VNA and spectrum analyzer are used for character-

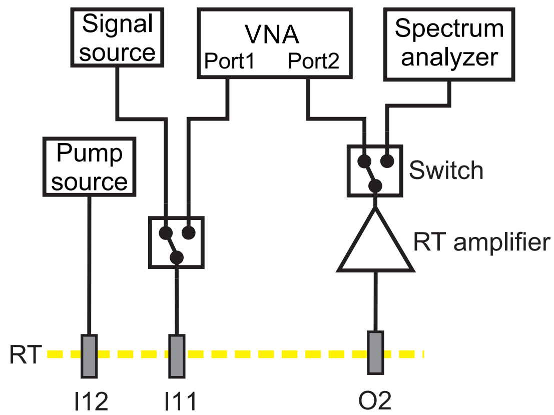

Figure 4.10: Schematics of the room temperature setup for Q600 JPA. RT: room temperature.

ization measurements, while the dual-path receiver is used for state reconstructions. A schematic of the setups for Q300 JPA is shown in Appendix A, and it is explained in Ref. [40]. Here mainly the setups of Q200 JPA are presented.

4.2.1 Dual-path receiver

The dual-path state reconstruction method is based on statistics and cross-correlation techniques. It consists of the cryogenic part (Fig. 4.2 marked in blue) and the room temperature part (Fig. 4.11 marked in magenta). A complete schematic of the dual-path receiver is presented in Appendix B. Fig. 4.12 shows a simplified schematic of a dual-path receiver. We split a signal under study described by bosonic annihilation and creation operators $\hat{a}$ and $\hat{a}^\dagger$ using a hybrid ring and feed them into two amplification and detection chains. In the splitting process vacuum fluctuations, represented by $\hat{v}$ and $\hat{v}^\dagger$, are added to the signals. In our case, the signal is a squeezed state emitted from the JPA samples, and the vacuum fluctuations are realized by terminating the second input port of the hybrid ring with a broadband $50\,\Omega$ load. At the two output ports, we first amplify the signals using cold HEMT amplifiers and room temperature amplifiers and then downconvert them from radio frequency (RF) to an intermediate frequency (IF) of 11 MHz using IQ-mixers. For the Q300 JPA measurements (see Appendix A), a Field Programmable Gate Array (FPGA) based receiver [32,39,40] is used. Here, the resulting orthogonal quadrature signals $I_{1,2}$ and $Q_{1,2}$ after the IQ-mixers are filtered, amplified and digitized by four Analog-Digital-Converters (ADCs), and processed in real time by an FPGA logic. For the experiments on Q200 JPA, an Acqiris card based receiver is used. Here, only

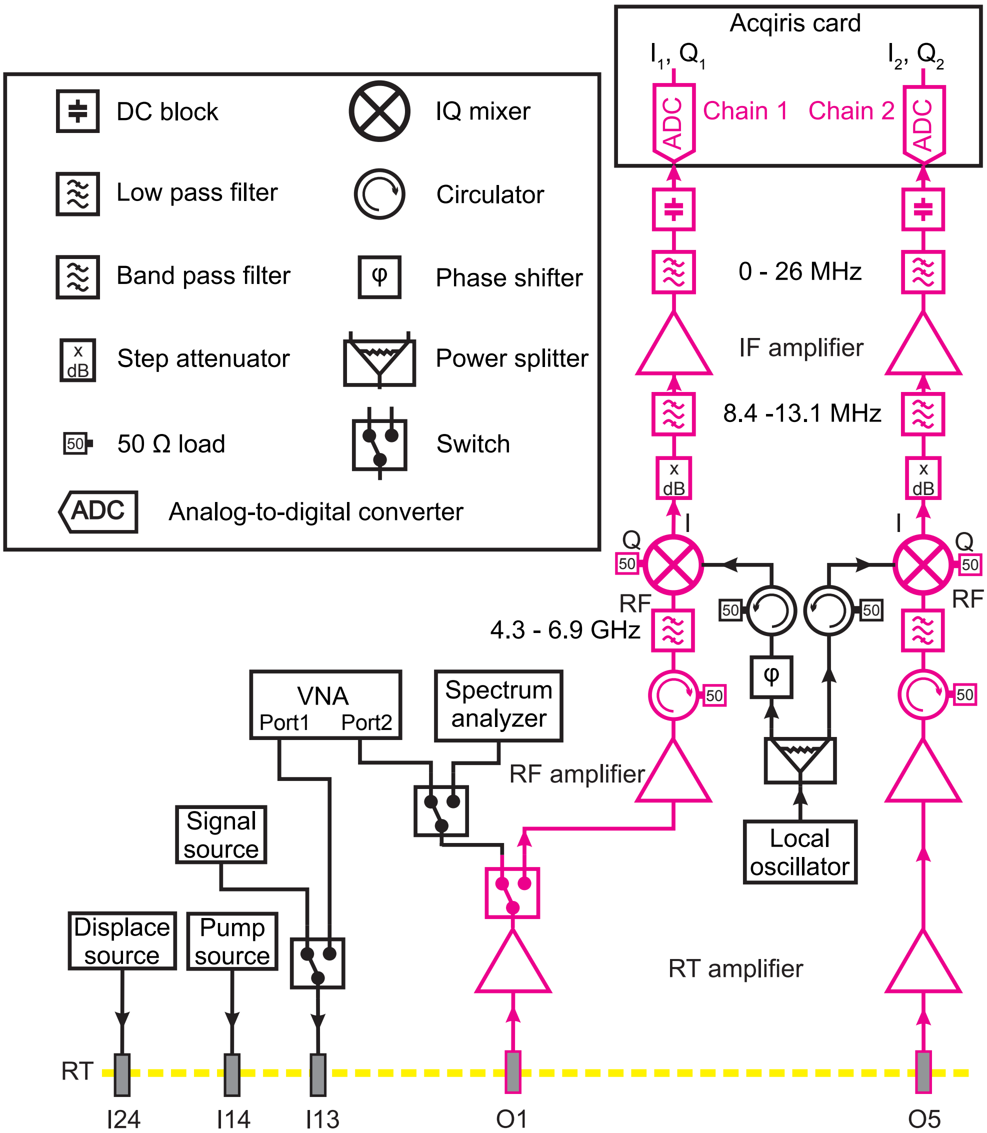

Figure 4.11: Schematics of the room temperature setup for Q200 JPA. The room temperature dual-path receiver, which is the extension of the cryogenic dual-path receiver (Fig. 4.2, marked in blue), is marked in magenta.

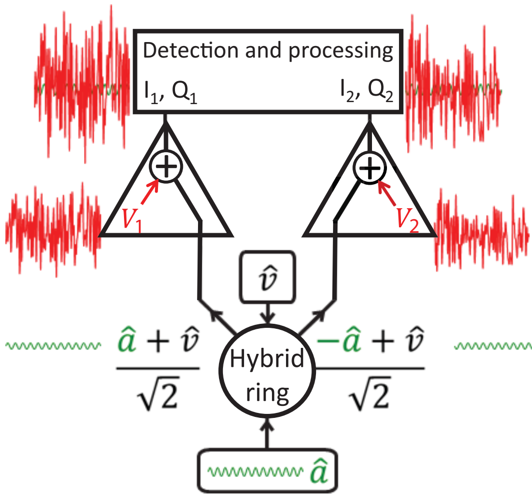

Figure 4.12: A simplified schematic of the dual-path receiver.

one output of each IQ mixer is used. The quadrature ($I_{1,2}$ and $Q_{1,2}$) calculations are performed by a conventional computer CPU after data acquisition.

Based on the beam splitter relations and the fact that the noise contributions from the two detection chains are statistically independent, we get access to all moments of signal and noises added by the two detection chains. In reality, we record the noisy quadrature moments $\langle I_1^{j'} I_2^{k'} Q_1^{m'} Q_2^{n'} \rangle$ up to fourth order $0 < j' + k' + m' + n' \leq 4$, and $j', k', m', n' \in \mathbb{N}_0$. The reconstructed signal and noise moments have the form of $\langle (\hat{a}^\dagger)^l \hat{a}^m \rangle$ and $\langle \hat{V}_{1,2}^r (\hat{V}_{1,2}^\dagger)^s \rangle$, respectively. Here, $\hat{V}_{1,2}$ and $\hat{V}_{1,2}^\dagger$ represent annihilation and creation operators of the noise modes in the detection chains, $0 < l + m \leq 4$, and $0 < r + s \leq 4$ with $l, m, r, s \in \mathbb{N}_0$. With the third and fourth order moments we calculate the third and fourth order cumulants, $\langle\langle (\hat{a}^\dagger)^l \hat{a}^m \rangle\rangle$ for $l + m = 3, 4$ and $l, m \in \mathbb{N}_0$, to verify the Gaussianity of the state [85, 86] (Appendix C). Furthermore, we use the first and second order moments to reconstruct the Wigner functions of the signal at the hybrid ring input and the noises added by the two detection chains. Analytical expressions of signal and noise moments, and the Wigner function construction are presented in Appendix D.

To make sure all the microwave devices are properly synchronized, they are connected to a 10 MHz reference supplied by a rubidium frequency standard. In the following, the IQ cross-correlation detector, which mainly contains the components after the IQ-mixers, is explained in detail. For the Acqiris card based setup, one IQ-mixer output is used, and the $I_{1,2}$ and $Q_{1,2}$ quadratures and moments calculations are performed after data acquisition. The details are presented in Sec. 4.2.3. The FPGA based setup for Q300 JPA uses both of the IQ-mixer outputs, and the quadratures

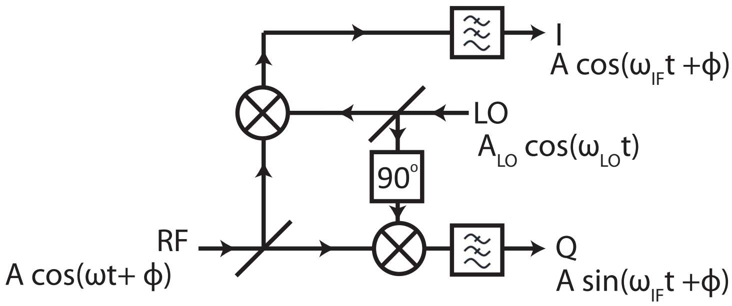

Figure 4.13: Schematic of an IQ mixer. LO: local oscillator, intermediate frequency $\omega_{\mathrm{IF}} = \omega_{\mathrm{LO}} - \omega$.

and moments calculations are performed in real time with the FPGA logic. For details, refer to Refs. [32, 39, 40].

4.2.2 IQ cross-correlation detector

As discussed in Sec. 2.1, a microwave signal is described by its magnitude and phase, A and $\phi(t)$ in Eq. (2.2). At the same time, the in-phase and out-of-phase components, $I(t)$ and $Q(t)$ also provide a complete description.

For the FPGA based dual-path receiver, both the I and Q outputs of IQ-mixers are used. An IQ-mixer(Fig. 4.13) is biased by a local oscillator, $A_{\mathrm{LO}}\cos(\omega_{\mathrm{LO}}t)$, with a frequency ω_{LO} and magnitude A_{LO}. After the IQ-mixer, the input RF signal $A\cos(\omega t+\phi)$ is converted into two components with frequencies $\omega_{\mathrm{LO}}\pm\omega$. The higher frequency terms are filtered away [87]. In the end, the two outputs of the IQ-mixer become

$$
\begin{aligned}
I_{\mathrm{IF}}(t) =& \frac{A_{\mathrm{LO}}}{2} A\cos(\omega_{\mathrm{IF}}t+\phi)\,, \\
Q_{\mathrm{IF}}(t) =& \frac{A_{\mathrm{LO}}}{2} A\sin(\omega_{\mathrm{IF}}t+\phi)\,,
\end{aligned} \tag{4.1}
$$

where, $\omega_{\mathrm{IF}} = \omega - \omega_{\mathrm{LO}}$. Inside the FPGA, digital down-conversion with a local oscillator $\cos(\omega_{\mathrm{IF}}t)$ is implemented to convert the IF signals into DC signals. Here we point out that during digital down-conversion $2\omega_{\mathrm{LO}}$ terms are generated. Digital filters are needed to filter out $2\omega_{\mathrm{LO}}$ terms. In the end, the DC signals become

$$
\begin{aligned}
I_{\mathrm{DC}} =& \frac{A_{\mathrm{LO}}}{4} A\cos(\phi)\,, \\
Q_{\mathrm{DC}} =& \frac{A_{\mathrm{LO}}}{4} A\sin(\phi)\,.
\end{aligned} \tag{4.2}
$$

For the Acqiris card based dual-path receiver, one output of each IQ-mixer is used. Let us suppose output I is used. After the IQ-mixer, the RF signal becomes $I_{\mathrm{IF}}(t) = \frac{A_{\mathrm{LO}}}{2} A\cos(\omega_{\mathrm{IF}} t + \phi)$. The I and Q terms are obtained by integrating over one period of the IF frequency,

$$I = \frac{\omega_{\mathrm{IF}}}{2\pi} \int_t^{t+2\pi/\omega_{\mathrm{IF}}} \cos(\omega_{\mathrm{IF}}\tau) I_{\mathrm{IF}}(\tau) d\tau = \frac{A_{\mathrm{LO}}}{4} A\cos(\phi) \tag{4.3}$$

$$Q = \frac{\omega_{\mathrm{IF}}}{2\pi} \int_t^{t+2\pi/\omega_{\mathrm{IF}}} \sin(\omega_{\mathrm{IF}}\tau) I_{\mathrm{IF}}(\tau) d\tau = \frac{A_{\mathrm{LO}}}{4} A\sin(\phi)\,. \tag{4.4}$$

These calculations are performed with a computer after data acquisition.

As shown in Fig. 4.11, in front of the IQ-mixers, RF amplifiers are used to further amplify the signals. Bandpass filters reduce the detection bandwidth to avoid the compression of the IF amplifiers induced by broadband noise. Next, IQ-mixers, which are biased with local oscillators with a frequency 11 MHz lower than the signal frequency, downconvert the RF signals to IF signals. The local oscillators for the two IQ mixers are supplied by splitting the signal from a single microwave source. A phase shifter is inserted into one of the local oscillator inputs to balance the phase of both chains. Before the IF amplifiers used for the amplification of the IF signals, step attenuators and IF bandpass filters are placed. The step attenuators adjust the amplitude of the IF signals to the detection range of the ADCs inside the Acqiris card or the FPGA, and pre-balance the signals in the detection chains. The band pass filters filter away the $(\omega + \omega_{\mathrm{LO}})$ signals generated by the IQ-mixers. After the IF amplifiers, low pass filters and DC blocks are installed. The low pass filters are use to reduce the noise bandwidth of the IF amplifiers, and the DC blocks are used to filter out the possible DC voltages induced by ground loops, which could damage the ADCs. Isolators are inserted to the setup to avoid possible spurious noise correlations. Finally, the IF signals are converted into digital signals by ADCs at a rate of 400 MHz. The data is transferred to a computer for the IQ quadrature calculations, digital filtering and moments calculations. For the FPGA based setup, the sampling rate is 150 MHz, and the digital down-conversion, digital filtering, and moments calculations are performed in real time with an FPGA logic [39, 40].

4.2.3 Acqiris card based data acquisition and processing

The IF signals are digitized using an Acqiris DC440 with 12-bit resolution and 400 MHz maximum sampling rate. The card has two ADC inputs. The input voltage ranges are from ±125 mV to ±5 V. In the experiments, ±1 V is usually used.

The card has 8×10^6 samples acquisition memory, which means 4×10^6 samples for each chain. This is insufficient for our measurement scheme. Therefore, when the memory is full, the data is transferred to a computer for further processing. Fig. 4.14 gives an overview of the data processing. First, the Acqiris card records samples until the required number of samples and segments is reached. The samples are stored in N segments. Each segment consists of M samples, and $M \times N \leq 4 \times 10^6$ for each chain. Then all the samples are transferred to a computer. Next, by integrating over the period of the IF frequency (Eqs. (4.3)-(4.4)), I and Q are computed. This is effectively a down-sampling procedure with a ratio of about 36. Digital FIR filters are implemented to filter out higher frequency terms from I and Q computation. In the third step, the moments up to fourth order are calculated for each sample. In the fourth step, the moments are averaged over segments. Now we get $M - 36$ samples [3] for each moment. By then, the first cycle is finished. After the step one (Fig. 4.14), data acquisition for the second cycle starts. The cycle is repeated until a desired number of cycles is reached. Every cycle is triggered by a high/low pulse generated by a Data Timing Generator (DTG). The DTG is synchronized with the other microwave sources by a 10 MHz reference. For details, refer to Ref. [42].

4.3 Phase stabilization

The dual-path method for state reconstruction is based on statistics of large number of the same events. This requires identical gain and phase of the setup to be constant during the measurement. In reality, there are always fluctuations, due to temperature drifts, stray magnetic fields, pressure fluctuations, instabilities of microwave sources, etc. Considerable efforts have been taken to reduce the effects of these environmental fluctuations on the measurements. The JPA temperature has been stabilized for squeezing and displacement measurements. The HEMT amplifier power supply and the room temperature amplifiers are temperature controlled. To stabilize the phase, a Labview based phase stabilization protocol has been implemented. We adjust the total number of samples for a measurement to fit within one minute. A squeezed state reconstruction is performed for this measurement. The phase drifts of the whole detection setup cause an offset between the reconstructed squeezed phase and the target squeezed phase. This can be corrected by adjusting the phase of the pump source. Then the measurement step, the corresponding state

[3] There are no complete integration windows for 1 to 18 and $M - 18$ to M samples for I and Q calculation, and this give minus 36.

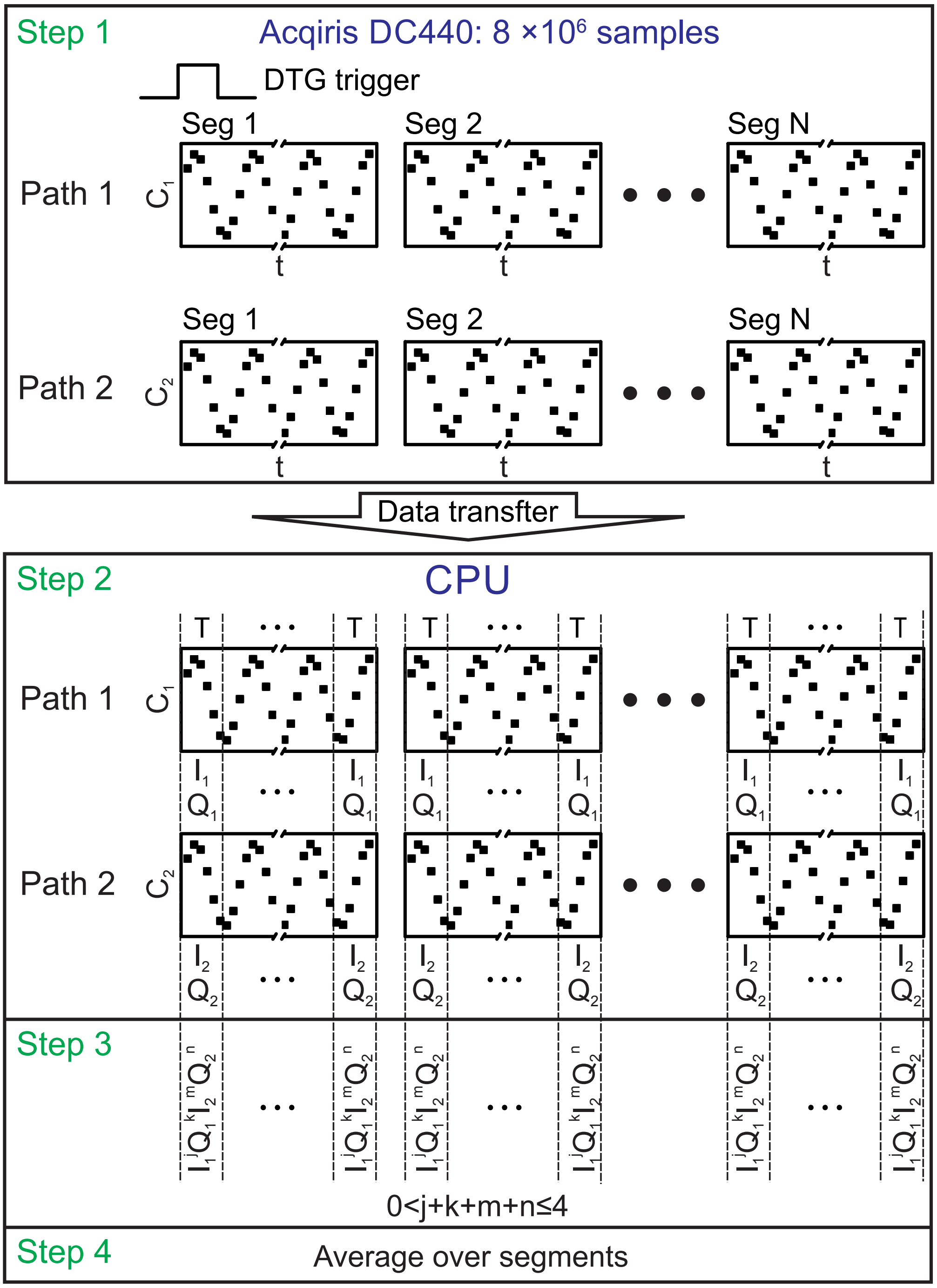

Figure 4.14: Sketch of data acquisition and processing of the Acqiris card based dual-path setup for one cycle. "T" denotes the period of the IF frequency. "Seg" denotes segment. The next cycle starts after step 1. The cycle average is performed by a computer after the required cycle number is reached.

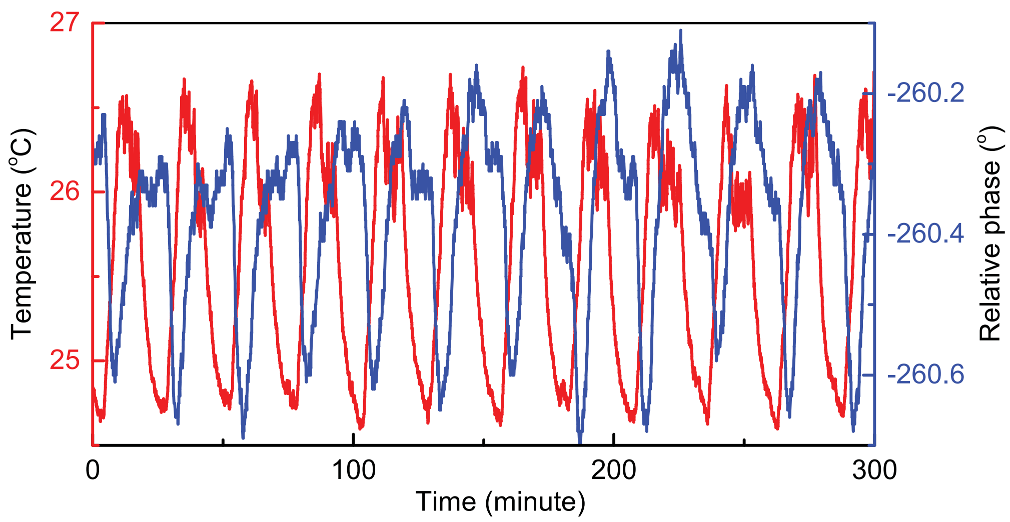

Figure 4.15: Red line shows SGS source temperature drifts over 300 minutes. Blue line depicts relative phase drifts between two SGS sources over 300 minutes. The two SGS sources are placed in an air-conditioner controlled room, and they generate RF signals at 12 GHz with a 6 GHz local oscillator connecting each other.

reconstruction and the phase correction are repeated until the desired total sample number is reached. In this way, the phase drift due to the microwave source and the output setup is corrected.

As discussed in Sec. 3.3-3.4, for remote state preparation three JPAs, and for quantum teleportation four JPAs are required. The three or four JPAs should operate in a phase-locked mode. We have studied SGS100A microwave sources from Rohde & Schwarz which could be operated in a daisy-chain configuration with local oscillators connecting all the units. With this option, the relative phase drifts between different units are minimized. Meanwhile, the IQ modulation of each unit allows the individual phase and magnitude adjustment.

Fig. 4.15 shows a stability test of two phase-locked SGS sources and their temperature. These two units are placed in an air-conditioner controlled room which gives a temperature stability within about 2 °C. It is clear that the temperature drift is the main reason for the phase drift of the sources. With a temperature control protocol [88], the temperature stability is improved to 0.2 °C. This temperature controlled phase stabilization protocol has not yet been used for the measurements in this thesis. However, it is going to be very crucial for future experiments of remote state preparation and quantum teleportation.

Chapter 5

JPA characterization

In this chapter, the characterization of Q600 and Q200 JPAs is discussed. We start with the flux dependence of the JPA resonance frequency. A strong hysteretic response is observed for Q600 JPA, which has a relative large screening parameter $\beta \equiv \frac{2L_{\mathrm{loop}}I_{\mathrm{c}}}{\Phi_0}$. A general approach has been developed to describe this hysteretic behavior. This approach is also valid for JPAs with small β . Then, a detailed study of non-degenerate amplification is presented. The characterization of the Q300 JPA which has been described in detail in Refs. [32, 40] , will not be presented here. For the measurements in this section, the JPA temperature is about 25 mK if no other value is specified.

5.1 Q600 JPA

5.1.1 Flux dependence of the resonance frequency

As already mentioned in Sec. 2.9, a magnetic flux Φ_{dc} , generated with an external coil, is used to tune the resonance frequency f_0 of a JPA to a desired value. At a fixed Φ_{dc}, a microwave pump tone provides high-frequency modulation of the magnetic flux through the SQUID, which generates high-frequency modulation of f_0 , which in turn leads to amplification. To measure the flux dependence of the resonance frequency, a Vector Network Analyzer (VNA) is used, as shown in Fig. 5.1. Since the JPA is a quarter-wavelength resonator, with one signal port, a reflection measurement scheme is needed. A measurement circulator is used to separate the JPA input signal and the signals reflected back from the JPA. Fig. 5.2 presents reflection spectroscopy measured on Q600 JPA when the external flux is swept from small to large values (Fig 5.2(a)) and from large to small values (Fig 5.2(b)). At a fixed flux value, the reflection spectrum shows a Lorentz dip in the magnitude and a 360° phase shift in the phase compared with the input wave at the JPA resonance frequency f_0. The resonance frequency f_0 shows a periodic dependence on the external flux. There are sudden jumps of f_0 (the dips of the spectra) at certain flux values. The flux up-sweep and down-sweep do not overlap over the whole range, and there is strong hysteresis.

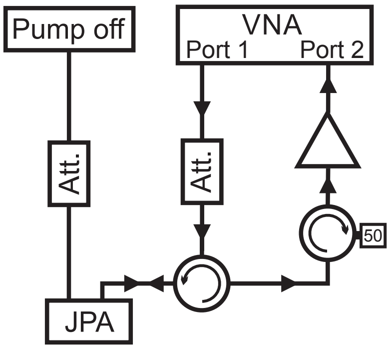

Figure 5.1: JPA reflection measurement scheme with a VNA. "Att." denotes attenuators.

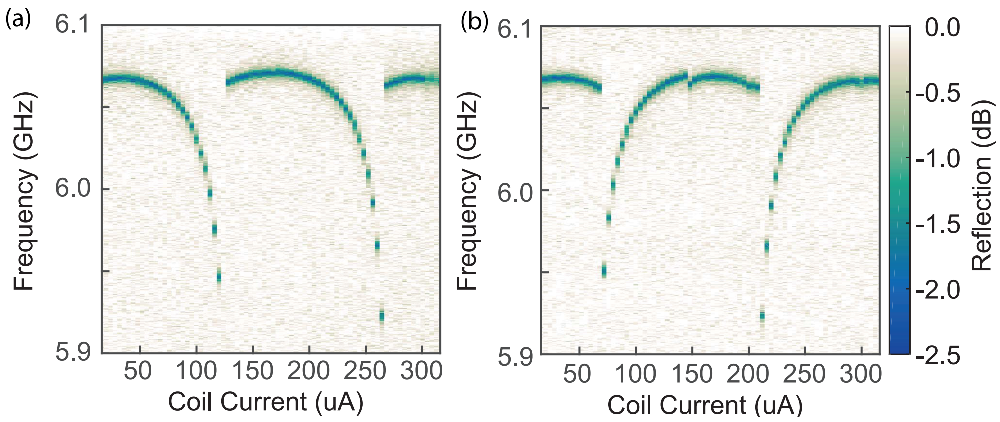

Figure 5.2: Reflection spectra of Q600 JPA as a function of the applied external flux with pump off. The coil current can be linearly mapped to flux threading the SQUID loop. (a): the coil current increases from $16\,\mu\mathrm{A}$ to $316\,\mu\mathrm{A}$. (b): the coil current decreases from $316\,\mu\mathrm{A}$ to $16\,\mu\mathrm{A}$.

Next we discuss a model to describe the observed behavior. The JPA resonance frequency f_0 depends on the cavity geometric capacitance and inductance, and on the SQUID inductance, which is flux dependent. Therefore we first calculate the SQUID inductance L_{squid}. From Eq. (2.58), we see that L_{squid} depends on the SQUID critical current I_{squid}. We assume the two junctions in the dc-SQUID to have identical critical current I_c (Fig. 2.6). According to the current-phase relation of a Josephson junction in Eq. (2.50), the superconducting currents through the two junctions are $I_1 = I_c \sin\varphi_1$ and $I_2 = I_c \sin\varphi_2$, respectively. Here, $\varphi_{1,2}$ are the phase differences across the two junctions. Therefore, the total current flowing through the SQUID I_b and the circulating current around the SQUID loop $I_{\rm cir}$ are written as

$$I_{\rm b} = I_1 + I_2 = 2I_c \sin\frac{\varphi_1+\varphi_2}{2}\cos\frac{\varphi_1-\varphi_2}{2} = 2I_c\sin\Phi_+\cos\Phi_-\,, \tag{5.1}$$

$$I_{\rm cir} = \frac{I_1 - I_2}{2} = I_c\cos\frac{\varphi_1+\varphi_2}{2}\sin\frac{\varphi_1-\varphi_2}{2} = I_c\cos\Phi_+\sin\Phi_-\,. \tag{5.2}$$

Here, we have defined

$$\Phi_+ \equiv \frac{\varphi_1+\varphi_2}{2}\,, \tag{5.3}$$

$$\Phi_- \equiv \frac{\varphi_1-\varphi_2}{2}\,, \tag{5.4}$$

to simplify the expressions. Following the flux quantization relation in Eq. (2.53), we get

$$\varphi_1 - \varphi_2 \equiv 2\Phi_- = 2\pi\frac{\Phi}{\Phi_0} + 2\pi n\,, \tag{5.5}$$

where $n \in \mathbb{Z}$, and Φ is the total magnetic flux through the SQUID (Eq. (2.55)), including the external flux $\Phi_{\rm ext}$ and the flux generated by $I_{\rm cir}$. For $\beta = 0$, we get $\Phi = \Phi_{\rm ext}$. In this case the maximum supercurrent of a SQUID $I_{\rm squid}$ follows the relation in Eq. (2.57).

For finite β, Eq. (2.57) is an approximation. For $\beta \ll 1$, this approximation is still reasonable to describe the flux dependence of both the SQUID inductance and the JPA resonance frequency. However, for Q600 JPA, this approximation is not applicable. We use the following method based on the resistively and capacitively shunted junctions model to describe a SQUID [62, 89],

$$\frac{1}{\omega_{\rm p1}^2}\ddot{\varphi}_1 + \frac{1}{\omega_{\rm c}}\dot{\varphi}_1 = -\sin\varphi_1 + j - \frac{1}{\pi\beta}(\varphi_1 - \varphi_2 - 2\pi\varphi_{\rm ext})\,, \tag{5.6}$$

$$\frac{1}{\omega_{\rm p2}^2}\ddot{\varphi}_2 + \frac{1}{\omega_{\rm c}}\dot{\varphi}_2 = -\sin\varphi_2 + j + \frac{1}{\pi\beta}(\varphi_1 - \varphi_2 - 2\pi\varphi_{\rm ext})\,. \tag{5.7}$$

Here, $j = I_{\rm b}/(2I_{\rm c})$ is the normalized bias current through the dc-SQUID, $\varphi_{\rm ext} = \Phi_{\rm ext}/\Phi_0$ is the normalized external flux, $\omega_{\rm p1,p2} = \sqrt{2eI_{\rm c}/\hbar C_{\rm j}}$ is the plasma frequency of each junction, and $\omega_{\rm c} = 2eR_{\rm j}I_{\rm c}/\hbar$ is the characteristic frequency of the junctions, with $R_{\rm j}$ and $C_{\rm j}$ the normal resistance and capacitance of each junction, and e the elementary charge.

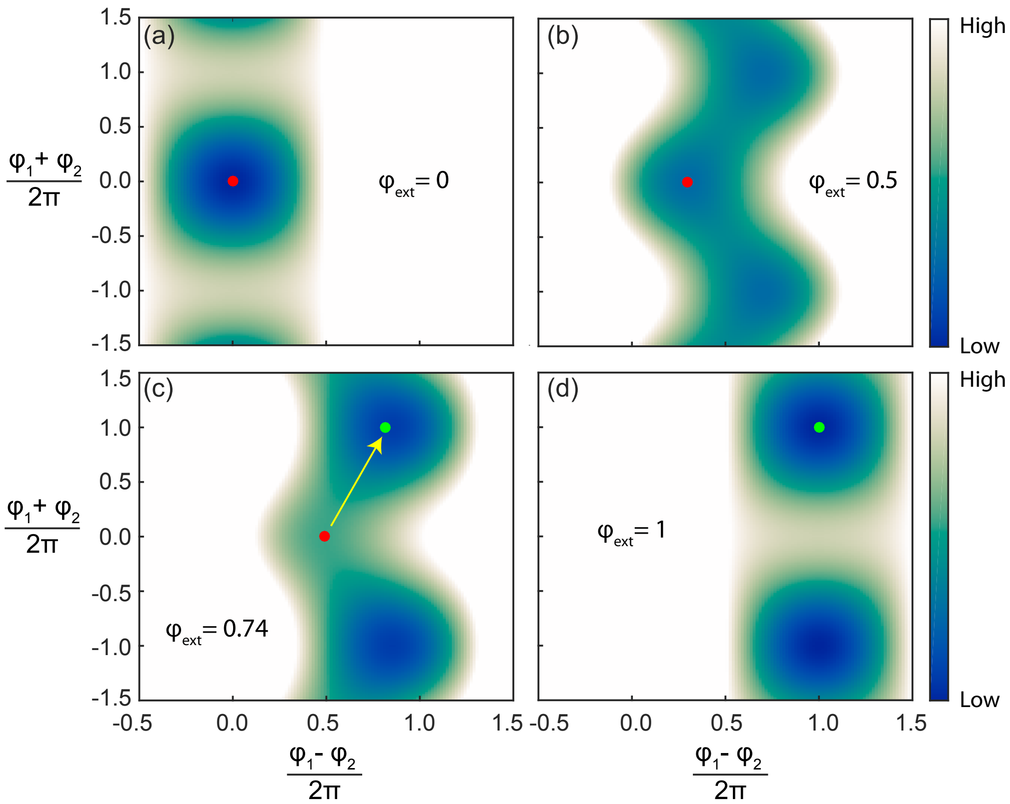

Figure 5.3: Color plots of the two-dimensional potential in Eq. (5.8) for different external flux values $\varphi_{\text{ext}} = \Phi_{\text{ext}}/\Phi_0$ and $\beta = 0.5$. The potential is 2π periodic versus $(\varphi_1+\varphi_2)/2$ and $(\varphi_1-\varphi_2)/2$ (not shown in the figure). The phase particle is initially located in a local minimum (red dot in (a)). When the external flux increases, the particle's position is preserved (b, c) until the barrier to the closest local minimum (green dot in (c)) disappears. Then the particle jumps to the position marked by the green dot (c).

Similar to a single Josephson junction, the motion of the SQUID "phase particle" with coordinates φ_1 and φ_2 is analogues to that of a particle with a certain mass moving in a two-dimensional washboard potential. The bias current I_{b} tilts the potential. This potential has the form,

$$v(\Phi_-, \Phi_+) = 2 - 2\cos(\Phi_+)\cos(\Phi_-) - 2j\Phi_+ + \frac{2}{\pi\beta}(\Phi_- - \pi\varphi_{\text{ext}})^2 \,. \tag{5.8}$$

Because of the flux quantization law (Eq. (5.5)), the Φ_- terms depend on the external flux. The potential is 2π periodic versus Φ_+ and Φ_-. When $\Phi_- = 2n\pi$, the local minima are located at $\Phi_+ = 2m\pi$ with $n, m \in \mathbb{Z}$. When $\Phi_- = (2n+1)\pi$, the local minima are at $\Phi_+ = (2m+1)\pi$. When Φ_- increases from $2n\pi$ to $(2n+1)\pi$, the local minima at $\Phi_+ = 2m\pi$ disappear and $(2m+1)\pi$ local minima appear. At a certain external flux value, the potential barrier between the $\Phi_+ = 2m\pi$ and $(2m+1)\pi$ local minima vanishes, and the phase particle jumps to the next local minimum. This jump leads to a discontinuity of the dependence of the SQUID critical current on the applied external flux and therefore a discontinuity of the dependence of the SQUID inductance L_{squid} on the applied external flux. In the end, the jumps of the phase particle correspond to the jumps of the resonance frequency of a JPA when the external flux is varied.

Four color plots of the SQUID potential for different external flux values $\varphi_{\text{ext}} = 0$, 0.5, 0.74, 1, and $\beta = 0.5$ are shown in Fig 5.3 to illustrate this process. We start with $\varphi = 0$ (Fig 5.3(a)). The phase particle is located at the position marked by the red dot with coordinates $\Phi_- = \Phi_+ = 0$. As φ_{ext} increases, the potential at the red dot gets shallower, and new local minima at $\Phi_+ = \pm\pi$ appear and get deeper. When $\varphi_{\text{ext}} = 0.74 \equiv \varphi_{\text{jump}}$, the potential barrier between the two nearest local minima (red and green dots) vanishes, and the phase particle jumps to the position marked by the green dot. Because of the periodicity along the Φ_+ direction, the phase particle jumps at $\varphi_{\text{ext}} = \varphi_{\text{jump}} + n$. When the flux sweep direction is reversed, which means Φ_- decreases, the phase particle jumps at $\varphi_{\text{ext}} = -\varphi_{\text{jump}} + n + 1$. In the flux window $-\varphi_{\text{jump}} + (n+1) < \varphi_{\text{ext}} < \varphi_{\text{jump}} + n$ the SQUID critical current I_{squid} has different values for flux up-sweep and down-sweep, which gives different L_{squid} and different resonance frequency f_0 of a JPA. In the flux window $\varphi_{\text{jump}} + n < \varphi_{\text{ext}} < -\varphi_{\text{jump}} + 2 + n$, the flux up-sweep and down-sweep lead to the same I_{squid} and thus to the same f_0. Altogether, this explains the hysteretic behavior of the flux dependence of the resonance frequency. When β approaches zero, φ_{jump} approaches 0.5, and the hysteresis window $-\varphi_{\text{jump}} + (n+1) < \varphi_{\text{ext}} < \varphi_{\text{jump}} + n$ gets narrower. Near $\varphi_{\text{ext}} = 0.5$, the JPA is very sensitive to even a small amount of flux noise. Here, it is experimentally difficult to detect the hysteretic dependence of the resonance frequency on the external magnetic flux. Our approach shows that the dependence of the critical current of a dc-SQUID on the external flux becomes hysteretic for $\beta \neq 0$. Usually one says that the internal (flux in the loop) versus externally applied flux characteristic becomes multi-valued for $\beta > 2/\pi$. This statement is still valid. The reason is that, in our case, the phase particle can jump between different Φ_+ values, whilst the textbook statement refers to the case when the phase particle is fixed to a constant Φ_+. The difference arises from different measurement schemes. In our case, the dependence of the critical current of a dc-SQUID on the external flux is deduced from the JPA reflection measurements. The textbook statement refers to a direct voltage-current measurement scheme.

The normalized dc-SQUID critical current ($j_\mathrm{c} = I_\mathrm{squid}/2I_c$) at a certain external flux value depends on the potential landscape. Fig 5.4 demonstrates how j_c is determined. The washboard potential becomes tilted when the bias current $j \neq 0$. At a fixed β and φ_ext, j is increased until all the local minima disappear. This j value is the normalized critical current j_c. The same calculation is done for different φ_ext at a fixed β. From Eq. (2.58), the SQUID inductance L_squid is obtained. The dependence of the JPA resonance frequency f_0 on L_squid can be written as [63],

$$\frac{\pi f_0}{2f_\mathrm{cav}} \tan \frac{\pi f_0}{2f_\mathrm{cav}} = \frac{L_\mathrm{cav}}{L_\mathrm{squid} + L_\mathrm{loop}} \,. \tag{5.9}$$

Here, L_cav and L_loop are the cavity and SQUID loop inductance, respectively, and f_cav is the cavity resonance frequency without a SQUID. Fitting Eq. (5.9) to the experimental data (Fig 5.5), we estimate $\beta = 0.59$, and the critical current of one junction $I_\mathrm{c} = 26\,\mu\mathrm{A}$, which gives a Josephson coupling energy $E_\mathrm{J} = h{\times}13{\times}10^3\,\mathrm{GHz}$. For fitting, the cavity inductance L_cav is fixed to $2\,\mathrm{nH}$.

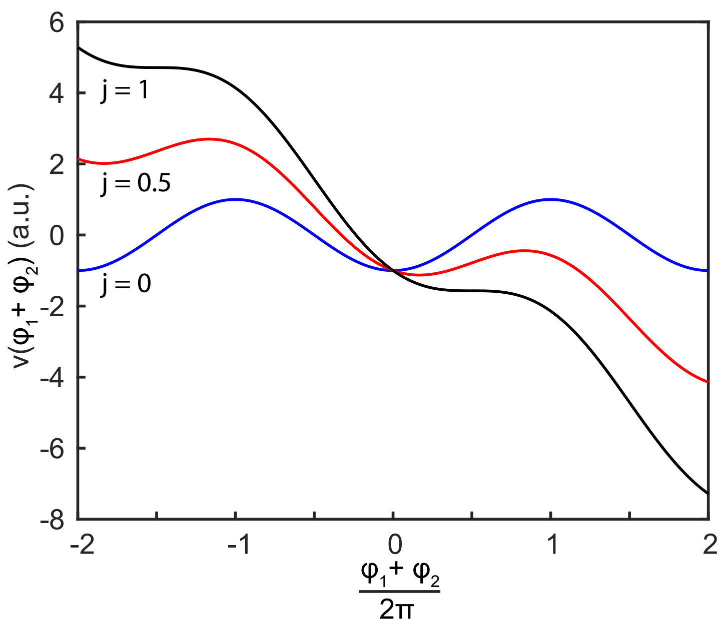

Figure 5.4: The SQUID potential in Eq. (5.8) versus $(\varphi_1 + \varphi_2)/2\pi$ with $\beta = 0.5$, and $(\varphi_1 - \varphi_2)/2 = 0$ and $\varphi_\mathrm{ext} = 0$. $j = I_\mathrm{b}/(2I_\mathrm{c})$. j is increased until all the local minima disappear, and this j is the normalized dc-SQUID critical current $j_\mathrm{c} = I_\mathrm{squid}/(2I_\mathrm{c})$.

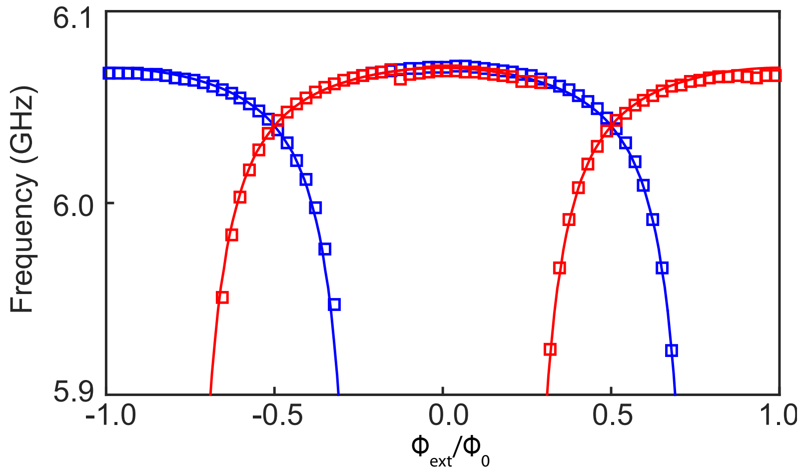

Figure 5.5: Fitting results of resonance frequency versus external magnetic flux $\Phi_{\mathrm{ext}}/\Phi_0$ for Q600 JPA. Blue color denotes a flux up-sweep. Red color denotes a flux down-sweep. The lines show theory fits according to Eq. (5.9). The squares depict experimental data (Fig. 5.2).

5.1.2 Multi-wave mixing

Parametric amplification can be viewed as a three-wave mixing process [90]. The interaction between a signal mode and a pump mode causes the splitting of a pump photon into a signal photon and an idler photon. During this process, energy and momentum are conserved. Energy conservation requires $f_{\mathrm{pump}} = f_{\mathrm{signal}} + f_{\mathrm{idler}}$. Momentum conservation means that the phases of signal, idler and pump modes have a well defined relation. When $f_{\mathrm{signal}} \neq f_{\mathrm{idler}}$, which is the non-degenerate case, the JPA is a phase-insensitive amplifier, which means signals with arbitrary phase are equally amplified. For an ideal JPA without losses, the noise added to the signal mode is a thermal state corresponding to the JPA physical temperature. When $f_{\mathrm{signal}} = f_{\mathrm{idler}}$, the JPA is in the degenerate mode and it acts as a phase-sensitive amplifier, which means that the anti-squeezed quadrature gets amplified. In this case, for an ideal JPA without losses, the added noise is zero. If the pump power is further increased, the situation gets complicated and additional phenomena, such as multi-wave mixing, appear [91, 92]. Fig. 5.6(a) is a color map of power spectra detected with a spectrum analyzer at different pump powers, where a spectrum with zero pump power is used as a reference. The pump tone has a fixed frequency. Fig. 5.6(b) shows four horizontal cuts of Fig. 5.6(a). The input signal, which is marked by a red tick in Fig. 5.6(a) and at mode 2 in Fig. 5.6(b), has a power of about $-133\,\mathrm{dBm}$ estimated at the sample box input. An idler mode (mode 4) is generated at $f_{\mathrm{idler}} = f_{\mathrm{pump}} - f_{\mathrm{signal}}$. When the pump power is below the bifurca-

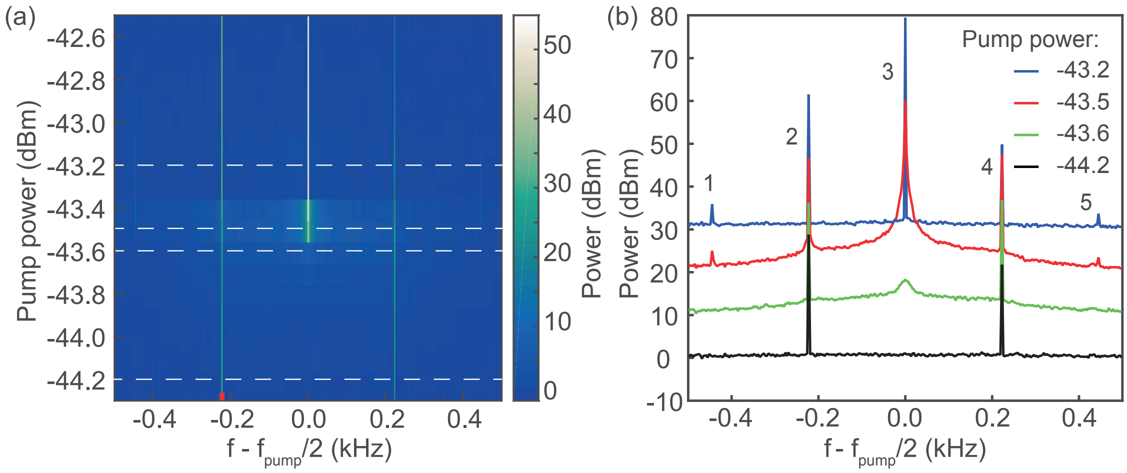

Figure 5.6: (a) Power spectra detected with a spectrum analyzer at different pump powers. The noise background is subtracted from the spectra. The pump power is estimated at the JPA box input. The red tick marks the input signal frequency. The power of the input signal is about $-133\,\mathrm{dBm}$ referred to the JPA box input. (b) Horizontal cuts of (a) whose positions are marked by dashed white lines. The green, red and blue spectra are shifted by $10, 20, 30\,\mathrm{dB}$, respectively for clarity.

tion point [93, 94], the signal and idler modes grow with increasing pump power. Across the bifurcation point, the process changes from parametric amplification to parametric oscillation [95, 96]. Meanwhile, multi-wave mixing occurs. For example, for mode 5, $2f_5 = 3f_{\mathrm{pump}} - 4f_{\mathrm{signal}}$, three pump photons and four signal photons generate two photons of mode 5.

5.2 Q200 JPA

5.2.1 Flux dependence of the resonance frequency

The flux dependence of the Q200 JPA resonance frequency measured with VNA does not show hysteretic behavior. Based on the model discussed in Sec. 5.1.1, for small β, the jumps of the JPA resonance frequency f_0 appear close to $\Phi_{\mathrm{ext}} = (n + 1/2)\Phi_0$ with $n \in \mathbb{Z}$. At these positions, the cavity is very sensitive to flux fluctuations. Therefore, it is much more difficult to observe the hysteretic behavior experimentally. The same approach as discussed in Sec. 5.1.1 is used to fit the flux dependence of the JPA resonance frequency for the Q200 sample. The results are shown in Fig 5.7. From the fit, we can estimate $\beta = 0.24$ and the critical current of one junction $I_{\mathrm{c}} = 6\,\mu\mathrm{A}$ which gives a Josephson coupling energy $E_{\mathrm{J}} = h \times 3 \times 10^3\,\mathrm{GHz}$.

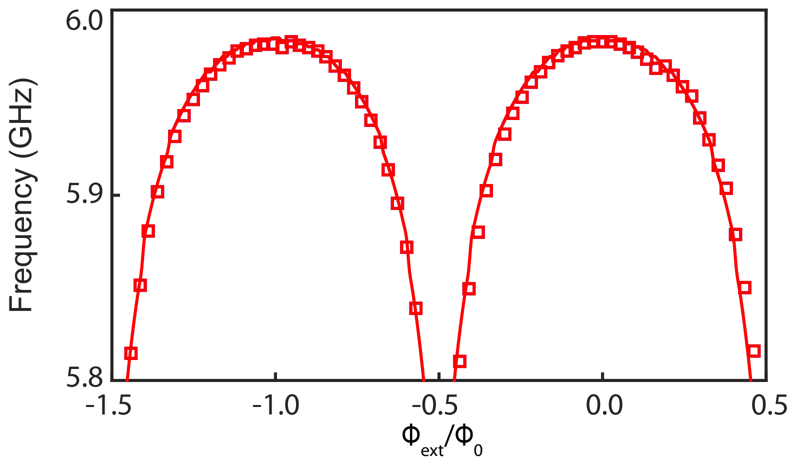

Figure 5.7: Flux dependence of the resonance frequency for Q200 JPA. The lines are fits of the experimental data (squares) according to Eq. (5.9) for flux up-sweep and down-sweep.

5.2.2 Non-degenerate gain

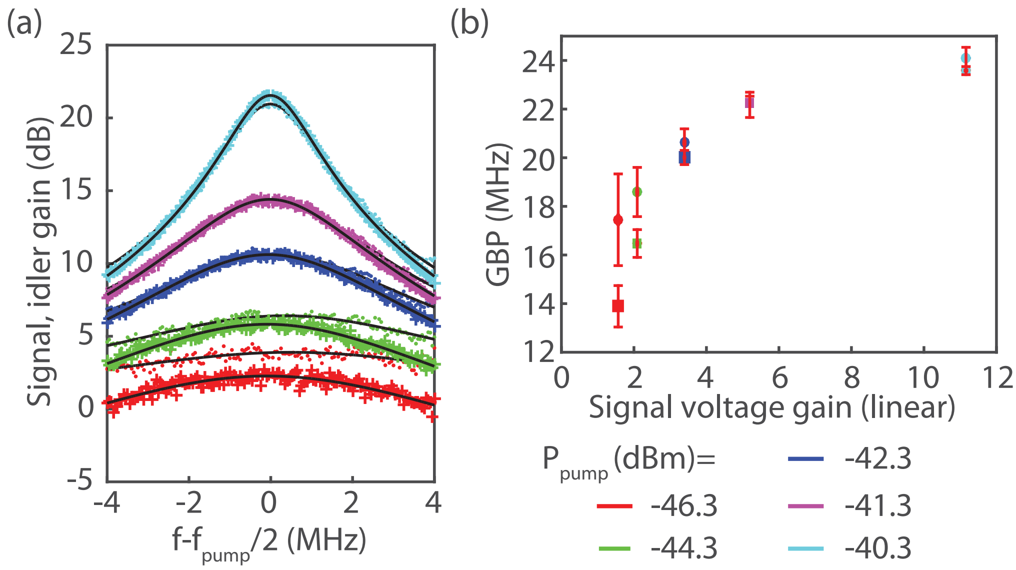

Figure 5.8: (a) Signal (dots) and idler (crosses) gains measured with a spectrum analyzer at different pump powers. Lines depict Lorentzian fits. (b) GBP as a function of the signal voltage gain in linear units. Error bars show 95% confidence bounds from fittings. GBP: product of the voltage gain in linear units and the bandwidth in MHz. The cavity frequency without a pump tone is $f_0 = 5.8545\,\mathrm{GHz}$. The power of the input signal is about $-160\,\mathrm{dBm}$.

When a JPA is operated in the non-degenerate mode, which means the signal frequency is detuned from half the pump frequency, signal and idler modes have different frequencies. In this case, both modes can be observed individually. When the pump power is increased, signal and idler gains grow until they converge. In Fig. 5.8(a), the signal and idler gain measured with a spectrum analyzer are shown. For these measurements, the flux is set to a value corresponding to $f_0 = 5.8545\,\mathrm{GHz}$ and the pump frequency is set to $2f_0$.

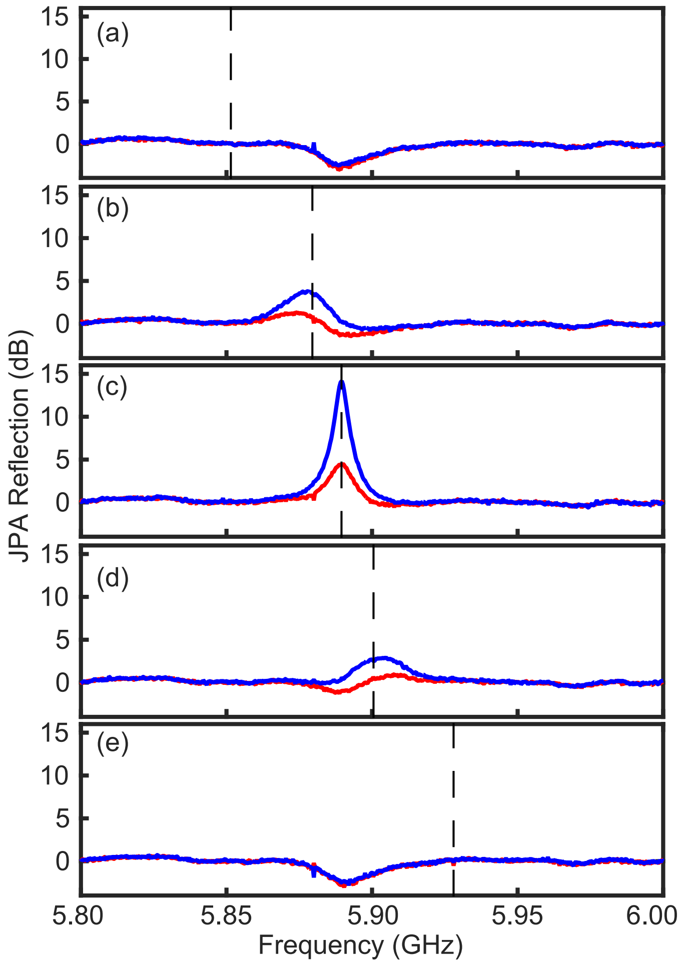

Figure 5.9: Reflection of Q200 JPA measured with a VNA with different pump frequencies (a)-(e). The cavity resonance frequency with the pump switched off is $5.8895\,\mathrm{GHz}$. Vertical dashed lines mark half of the pump frequency. Red (blue) lines depict measurements for a pump power of $-42\,\mathrm{dBm}$ ($-39\,\mathrm{dBm}$).

The bandwidth decreases, if the gain increases. In the high-gain limit, the measured gain-bandwidth-product (GBP) (Fig. 5.8(b)), which is the product of the voltage gain in linear units and the bandwidth, approaches a constant value, f_0/Q_{ext}. However, in the low-gain limit, the measurements deviate from theory. Since the signal gain is calibrated against a pump-off condition, theoretically the signal gain is expected to approach $0\,\mathrm{dB}$, the signal bandwidth goes to infinite, and the idler gain

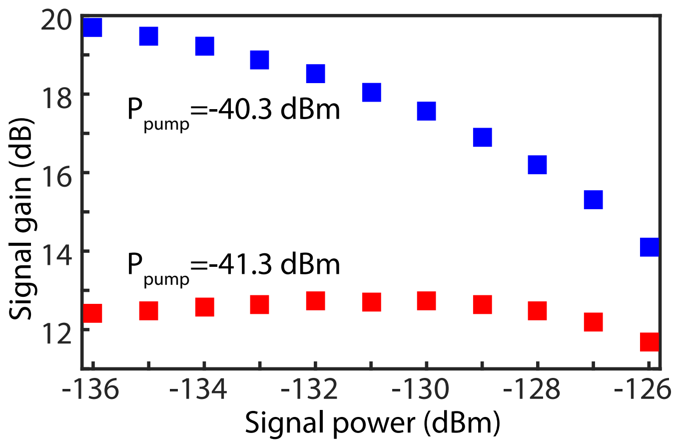

Figure 5.10: Signal gain versus JPA input signal power measured with a VNA. The input signal power and pump power are estimated at the JPA sample-box. Cavity frequency without a pump tone $f_0 = 5.8545\,\mathrm{GHz}$. The pump frequency is $f_{\mathrm{pump}} = 2f_0$.

vanishes. Therefore, we expect an increase of the signal GBP and a decrease of the idler GBP. The deviation between experiments and theory is due to the fact that the measurements are very sensitive to the calibration data in the low-gain limit.

The previous discussion in this section was based on a fixed pump frequency. Next, we discuss the response of the JPA to pump frequency. Fig. 5.10 shows Q200 JPA reflection measurements with a VNA for different pump frequencies. $f_{\mathrm{pump}}/2$ is marked by vertical dashed lines. When $f_{\mathrm{pump}}/2$ is far from the cavity frequency f_0 (Fig. 5.10(a)(e)), the JPA reflection shows a Lorentzian dip. The JPA shows signal gain when $f_{\mathrm{pump}} = 2f_0$ (Fig. 5.10(c)). When f_{pump} approaches $2f_0$, the JPA reflection shows a peak and dip structure (Fig. 5.10(b)(d)). For different pump powers (red and blue lines), the response of the JPA to the pump frequency is similar.

5.2.3 1 dB-compression point

The 1 dB-compression point is an important parameter for a JPA used as an amplifier [31]. Input signals with power below the compression point get amplified with a constant gain. The gain of input signals with power above the compression point starts to decrease as the input signals' power increases. Fig. 5.10 shows the signal gain as a function of input signal power for two pump powers. The pump frequency is set to $2f_0$. For a pump power of $P_{\mathrm{pump}} = -41.3\,\mathrm{dBm}$, the 1 dB-compression point is estimated to be $-127\,\mathrm{dBm}$. When $P_{\mathrm{pump}} = -40.3\,\mathrm{dBm}$, it is difficult to get the maximal gain from this measurement. From the figure, it is clear that the

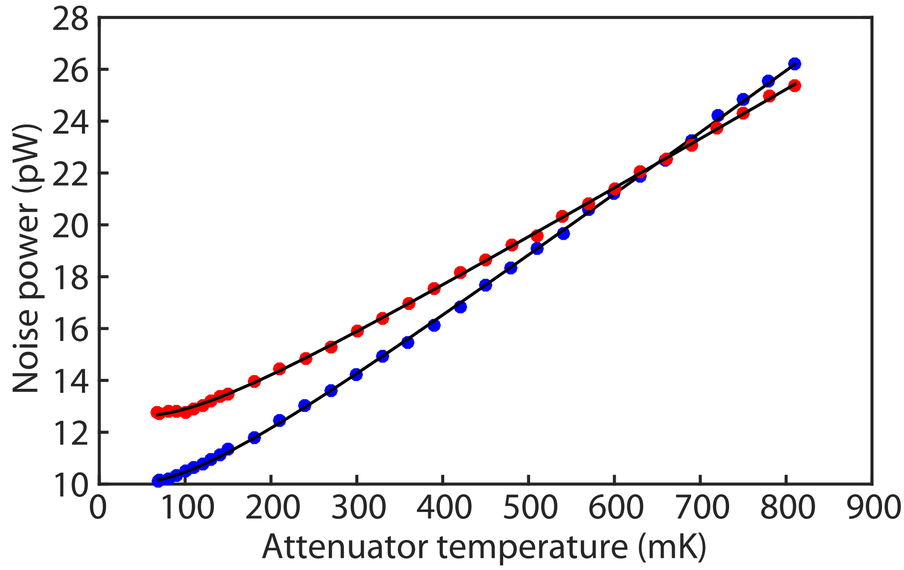

Figure 5.11: Power detected by a spectrum analyzer as a function of the noise source temperature. Black lines denote theoretical fits according to Eq. (5.10). Blue dots represent experimental data for chain 1 which corresponds to the fridge output 1. Red dots are experimental data for chain 2 which corresponds to the fridge output 5. The resolution bandwidth is $200\,\mathrm{kHz}$, and the video bandwidth is $500\,\mathrm{kHz}$. The JPA temperature is stabilized at $50.45\,\mathrm{mK}$.

1dB-compression point is lower if the JPA is operated with a higher pump power.

5.2.4 Noise properties in the non-degenerate mode

A low noise temperature is essential for quantum limited amplification. We have used spectrum analyzer based measurements to estimate the noise temperature of the Q200 JPA operating in the non-degenerate mode. The JPA pump power is set to a value which gives 10.7 dB signal gain. The JPA resonance frequency with pump off is $f_0 = 5.894\,\mathrm{GHz}$. The temperature of the 30 dB-attenuator, which is connected to the input of the JPA measurement circulator via a short coaxial cable [1] (see Fig. 4.2), is varied from 50 to $800\,\mathrm{mK}$. This attenuator emits a thermal state corresponding to its temperature. This thermal state gets amplified by the JPA and the detection chain. The total noise power P detected by a spectrum analyzer at

[1]The coaxial cable in these measurements is a 17 mm stainless steel cable, not a NbTi/NbTi superconducting cable as indicated in Fig. 4.2. The total cable and connector loss is estimated to 1.5 dB.

room temperature is

$$P(T_{\mathrm{att}}) = GB\left\{\frac{hf_0}{2}\coth\left[\frac{hf_0}{2k_{\mathrm{B}}\left(T_{\mathrm{att}}+\delta T\right)}\right] + k_{\mathrm{B}}T_{\mathrm{total}}\right\}, \tag{5.10}$$

where G denotes the total gain, B is the detection bandwidth, $h = 6.626\times10^{-34}\,\mathrm{J\cdot s}$ is the Planck constant, $k_{\mathrm{B}} = 1.38\times10^{-23}\,\mathrm{J/K}$ is the Boltzmann constant and T_{total} is the total noise temperature of the complete detection chain, which includes the measurement circulator, the JPA, the hybrid ring and the detection chain. The first term in Eq. (5.10) represents thermal fluctuations and vacuum fluctuations according to Ref. [97]. δT denotes a possible deviation between the electronic temperature of the attenuator and the measured temperature (the phononic temperature). The cable and connector losses of the attenuator and the measurement circulator are considered with the beam splitter model. By fitting our experimental data with Eq. (5.10) (Fig. 5.11), we estimate $T_{\mathrm{total1}} = 232\pm5\,\mathrm{mK}$ and $T_{\mathrm{total2}} = 446\pm6\,\mathrm{mK}$, which correspond to $n_{\mathrm{total1}} = 0.82\pm0.02$ and $n_{\mathrm{total2}} = 1.58\pm0.02$ for chain 1 and chain 2, respectively. The uncertainties are derived from 95% confidence bounds of the fits. These values are close to the standard quantum limit for phase-insensitive amplifiers of 0.5 photons. The deviation of the number of noise photons in the whole detection chains from the standard quantum limit has mainly two reasons. First, JPA noise contributes to additional noise photons. Second, the detection chains without the JPA, including the hybrid ring, HEMT amplifiers, circulators and room temperature amplifiers, add additional noise photons. We also notice that the number of noise photons in chain 2, n_{total2}, is twice that of chain 1, n_{total1}. The reason is that the detection chain 2 without the JPA adds more noise photons than chain 1.

Chapter 6

Displacement

A linear transformation is an important building block in remote state preparation, quantum teleportation, quantum state engineering, etc. In phase space, it corresponds to a displacement operation. In this chapter, we study the displacement of microwave states in the context of squeezed coherent states and coherent squeezed states. In Sec. 2.4.2, we have discussed two ways to generate a squeezed coherent state. Depending on the order of the squeeze operator $\hat{S}(\xi)$ and the displacement operator $\hat{D}(\alpha)$ applied on a vacuum state, the final states $\hat{S}(\xi)\hat{D}(\alpha)|0\rangle$ and $\hat{D}(\alpha)\hat{S}(\xi)|0\rangle$ can be different. To distinguish between them, we call the former a squeezed coherent state, and the latter a coherent squeezed state.

Experimentally, a squeezed coherent state can be generated by sending a coherent signal into a JPA. In this case, in order to get a squeezed coherent state the number of photons in the coherent signal is limited by the JPA compression. A coherent squeezed state can be generated by sending a squeezed state generated by a JPA into a directional coupler (Sec. 2.3), whose coupled port is biased with a coherent signal. The directional coupler applies a displacement operation on the squeezed state. In principle, this displacement operation can be applied to any quantum state incident at the input port. In this case, the maximal displacement that could be achieved is not limited by the JPA compression. In this chapter, both situations are discussed in detail.

Squeezed coherent states are investigated with Q300 JPA. The measurements have been performed with an FPGA-based dual-path setup (Appendix A). To be more specific, both I and Q outputs of the IQ-mixers are digitized with ADCs at a sampling rate of 150 MHz. Digital down-conversion, Cascaded Integrator Comb (CIC) and Finite Impulse Response (FIR) digital filters and the calculation of the moments are performed in real time. All the measurements with the Q300 JPA have been performed at an operation point frequency $f_0 = 5.637\,\mathrm{GHz}$. Coherent squeezed state experiments are performed with the Q200 JPA. The Acqiris card based dual-path setup (Sec.4.2) has been used. This means only one output of each IQ mixer is digitized with an ADC (Appendix B). I and Q calculations, FIR digital filters and the calculation of the moments are performed on a CPU. Because of the limited acquisition memory and data transfer rate, this setup is about a factor of 70 less efficient compared with the FPGA based setup. At the end of this chapter, main results of a following up project on coherent squeezed states performed with a “new JPA” sample are briefly presented.

6.1 Squeezed coherent states (Q300 JPA)

6.1.1 Photon number conversion factor (PNCF) calibration

The quadrature moments $\langle I_1^{j'} I_2^{k'} Q_1^{m'} Q_2^{n'} \rangle$ with $0 < j' + k' + m' + n' \leq 4$, and $j', k', m', n' \in \mathbb{N}_0$, detected either using an FPGA or an Acqiris card based dual-path receiver have a unit of V^2. While the signal moments referred to the hybrid ring input, $\langle (\hat{a}^\dagger)^l \hat{a}^m \rangle$ with $0 < l + m \leq 4$ and $l, m \in \mathbb{N}_0$, from the dual-path state reconstruction (Appendix D) have a unit of photon number. Before Wigner function reconstruction, the Photon Number Conversion Factors (PNCFs), which relate the measured autocorrelations $\langle I_{1,2}^2 \rangle$ and $\langle Q_{1,2}^2 \rangle$ to the number of photons at frequency f_0 at the hybrid ring input, are needed. With a thermal state at the hybrid ring input, the total power of each detection chain detected at the ADCs is

$$\begin{aligned} P_{1,2}(T_{\mathrm{att}}) &= \frac{\langle I_{1,2}^2 \rangle + \langle Q_{1,2}^2 \rangle}{R} \\ &= \frac{\kappa G_{1,2}}{R} \left[\frac{1}{2} \coth\left(\frac{h f_0}{2 k_{\mathrm{B}} T_{\mathrm{att}}} \right) + n_{1,2} \right], \end{aligned} \tag{6.1}$$

where $R = 50\,\Omega$ is the input resistance of the ADCs, $h = 6.626 \times 10^{-34}\,\mathrm{J \cdot s}$ is the Planck constant and $k_{\mathrm{B}} = 1.38 \times 10^{-23}\,\mathrm{J/K}$ is the Boltzmann constant. The products of the gains $G_{1,2}$ and κ, $\kappa \equiv R \times 2 \times B \times h f_0 = 1.83 \times 10^{-16}\,\mathrm{V}^2$, are the PNCFs of the whole detection chains from the hybrid ring inputs to the ADCs with B as the detection bandwidth. $n_{1,2}$ is the number of noise photons in the corresponding detection chain. By sending thermal states of different temperatures to the hybrid ring and detecting $\langle I_{1,2}^2 \rangle$ and $\langle Q_{1,2}^2 \rangle$, we can evaluate the PNCFs and $n_{1,2}$. For PNCF measurement, the pump of the JPA is off.

Experimentally, a 30 dB-attenuator is used as a broadband microwave blackbody emitter. However, this attenuator is not directly installed at the hybrid ring input. Instead it is connected at the JPA measurement circulator input with a short coaxial cable. The connection losses, including cable losses, connector losses, JPA insertion loss, circulator losses, etc., between the attenuator and the input of the hybrid are considered using a beam splitter model. The temperature gradient between the 30 dB-attenuator and the measurement circulator is also considered by dividing the cable into 100 pieces with 100 temperatures.

Fig. 6.1 shows a PNCF measurement for channel I_1. The measurements for Q_1, I_2 and Q_2 are similar. From the PNCF fitting, the number of noise photons in two detection chains can be determined. The results are shown in Tab. 6.1. A dual-path reconstruction [39, 43] (Appendix D) of the noise moments of two detection chains also provide the information of the number of noise photons. Both methods show consistent results.

Table 6.1: Number of noise photons in the two detection chains calculated from PNCF fitting and dual-path reconstruction. The uncertainties from PNCF fitting are 95% confidence bounds. The uncertainties from dual-path reconstruction are based on the statistics of 32 measurements. Each measurement is averaged over 5×10^5 traces. One trace contains 512 samples after digital filters in the FPGA logic. The measurement bandwidth is 978 kHz.

		Number of noise photons	
		PNCF fitting	Dual-path reconstruction
Chain 1	I_1 channel	24.22 ± 0.23	24.54 ± 0.02
	Q_1 channel	24.24 ± 0.23	
Chain 2	I_2 channel	27.08 ± 0.17	27.27 ± 0.02
	Q_2 channel	27.07 ± 0.18	

6.1.2 Measurement sequence

Fig. 6.2 shows typical averaged time traces of selected first and second moments from a single measurement, which corresponds to the situation in Fig. 2.3(c). Four Wigner function reconstructions are placed on top of the time trace. When both the JPA pump and the coherent signal at the JPA input are off, we can clearly identify the Wigner function of a vacuum state with its maximum centered at the origin of phase space. Once we turn on the coherent signal at the JPA input, which corresponds to a displacement operation, the vacuum state is equally displaced along the p- and q-quadratures and becomes a coherent state with a phase $\Theta = 45°$ referred to the hybrid ring input. Next, keeping the coherent signal on, we turn on the JPA

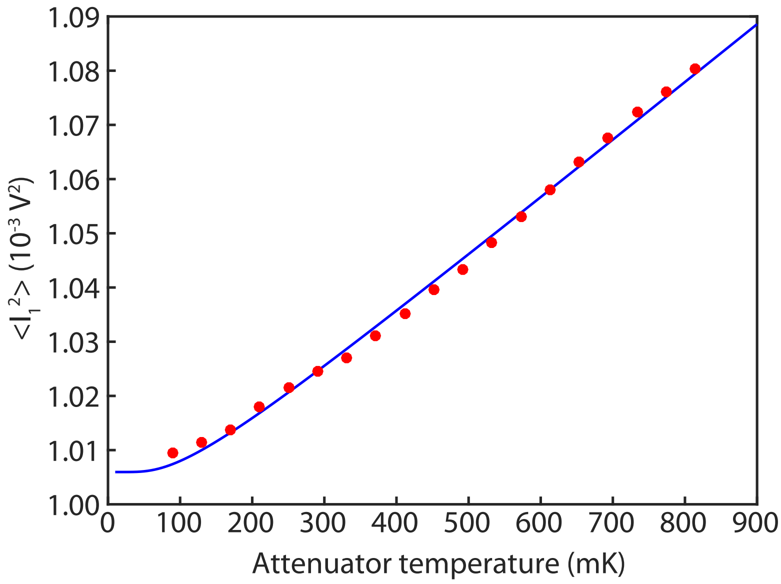

Figure 6.1: PNCF measurements for channel I_1. $\langle I_1^2 \rangle$ is plotted versus the temperature of the $30\,\mathrm{dB}$-attenuator. Red dots denote experimental data. Blue line indicates a theoretical fit. For each temperature value, $(5 \times 10^6$ traces$) \times$ (512 samples) are measured. The JPA temperature is stabilized at $60\,\mathrm{mK}$.

pump which squeezes the p-quadrature and anti-squeezes the q-quadrature ($\gamma = 90°$). This results in a suppression of the displacement of the state along the p-quadrature and a corresponding amplification of the displacement along the q-quadrature. Also the p-quadrature variance is squeezed and the q-quadrature variance is amplified, turning the circular profile of the Wigner functions of the vacuum and coherent states into an elliptic profile. Thus, the state becomes a squeezed coherent state with a squeezing level $\mathcal{S} = 4.3\,\mathrm{dB}$ below vacuum. Finally, keeping the pump on, we turn off the coherent signal to generate a squeezed vacuum state with a squeezing level $\mathcal{S} = 4.7\,\mathrm{dB}$.

6.1.3 Displacement of squeezed coherent states

In this context, we would like to point out the following experimental aspect. For the phase of a coherent state, both Θ and θ are defined as the angle between the displacement direction and the p-axis. Θ is the phase of a coherent state referred to the hybrid ring input. θ is the phase of the coherent state before applying the squeeze operator, which means θ is referred to the JPA input. During the propagation of the coherent state from the input of the JPA to the input of the hybrid ring, the phase of the coherent state evolves. We account for this effect by considering a constant

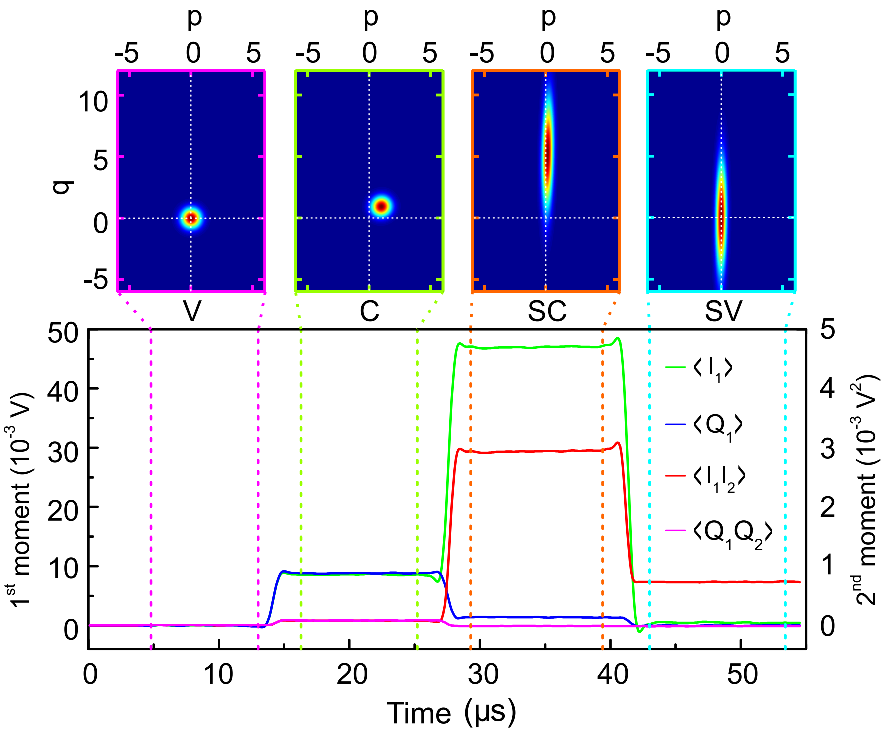

Figure 6.2: Average over 5×10^5 traces of selected first and second moments from a squeezed coherent state measurement. The phase of the coherent state is $\Theta = 45°$, and the anti-squeezed angle of the squeezed vacuum state is $\gamma = 90°$. The four color maps above the time traces are the Wigner function reconstructions of the vacuum, coherent, squeezed coherent and squeezed vacuum states referred to the input of the hybrid ring. p and q are dimensionless quadrature variables spanning the phase space. Reprinted figure from Ref. [32].

phase difference $\Delta\Theta \equiv \Theta - \theta$. For a squeezed state, $\gamma = -\tilde{\varphi}/2$ is the angle between the anti-squeezed quadrature and the p-axis, where $\tilde{\varphi}/2$ is the angle between the squeezed quadrature and q-axis. From theory [98], we expect the displacement of a squeezed coherent state after the squeeze operation to depend on the angles as Eq. (2.32), $\langle\hat{a}\rangle = \alpha\cosh r - \alpha^{\star}e^{\mathrm{i}\tilde{\varphi}}\sinh r$. Here, $\alpha = |\alpha|\exp\left[\mathrm{i}\pi\left(90° - \theta\right)/180°\right]$ is the complex amplitude of the coherent state before the squeeze operation and $\tilde{\varphi} = -2\gamma$ is the angle of the complex squeeze parameter.

By fixing the anti-squeezing angle of squeezed vacuum states γ at 0°, 45°, 90°, and 135° and rotating the phase Θ of the coherent signal, we map out the dependence of the displacement of a squeezed coherent state on γ and θ. In Fig. 6.3, we display the displacement, which is the center of the individual states in phase space given by their first moment $\langle\hat{a}\rangle$ for various values of Θ and γ. The squeezed vacuum states are centered at the origin, and the coherent states are located on a circle around

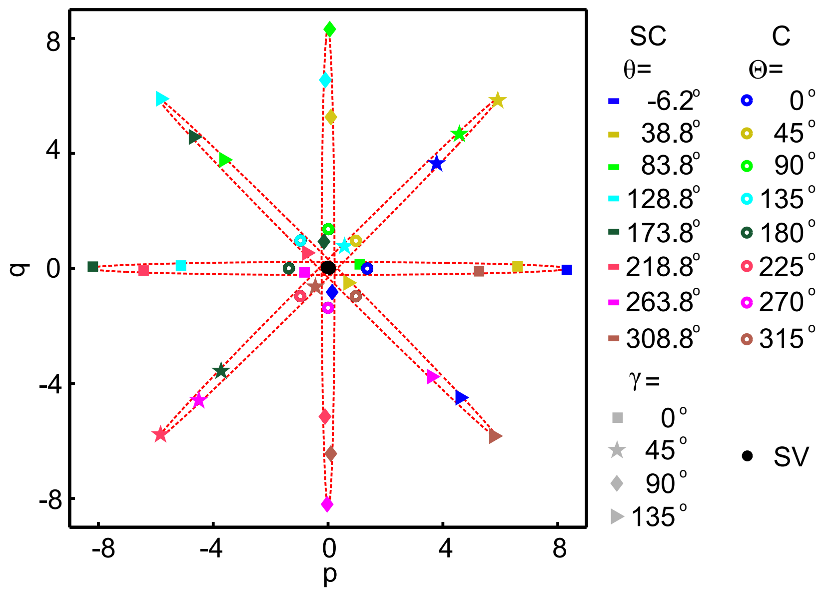

Figure 6.3: Experimental displacement for Squeezed Vacuum (SV), Coherent (C) and Squeezed Coherent (SC) states. The dashed red curves are fits of Eq. (2.32) to the squeezed coherent states (SC) data. For each of the 32 Θ- and γ-combinations, 2×10^6 traces are measured. Reprinted figure from Ref. [32].

the origin. If we turn on the JPA pump and rotate the phase of the coherent signal at the JPA input, the squeezed coherent state moves mainly along the γ direction. The displacement of the squeezed coherent states reaches its maximum when γ and θ fulfill $\gamma = \theta + 2n \times 90°$, where $n \in \mathbb{Z}$. Geometrically, this means that the anti-squeezed direction is collinear to the displacement vector pointing from the origin to the center of the state. For our choice of γ, we obtain a characteristic star-shaped pattern.

6.1.4 Photon numbers of squeezed coherent states

Similar to the center of the Wigner function, which represents the displacement, the photon number of a squeezed coherent state varies when we rotate the phase of the coherent signal Θ while keeping the anti-squeezed angle γ constant. Eq. (2.34) assumes a perfect vacuum state before applying the operations. Here we include the possible thermal photons present in the vacuum state at the JPA input with δN. Then, the photon number of a squeezed coherent state becomes

$$\begin{aligned}\langle a^\dagger a\rangle = \left(|\alpha|^2 + \delta N\right)\left(\cosh^2 r + \sinh^2 r\right) - (\alpha^*)^2 e^{i\tilde{\varphi}} \cosh r \sinh r \\ - \alpha^2 e^{-i\tilde{\varphi}} \cosh r \sinh r + \sinh^2 r,\end{aligned} \tag{6.2}$$

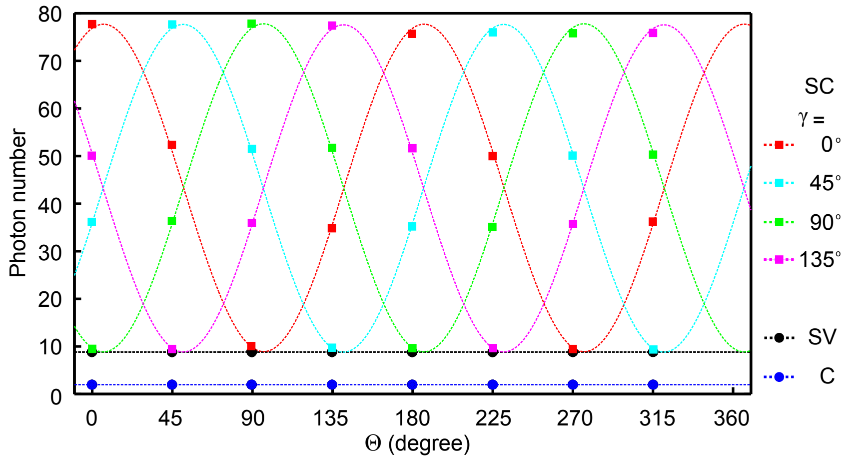

Figure 6.4: Experimentally obtained photon numbers for Coherent states (C), Squeezed Vacuum states (SV) and Squeezed Coherent states (SC) as a function of the coherent state phase Θ. The statistical uncertainty is smaller than the symbol size. The dashed curves are fits using Eq. (6.2). We note that the thermal contribution $\delta N \approx 0.005$ is vanishingly small. Furthermore, although this fit is performed independently from the one in Fig. 6.3, the obtained fit parameters are consistent. The data are from the same measurements as shown in Fig. 6.3. Reprinted figure from Ref. [32].

where $|\alpha|^2$ is the number of photons in the coherent state. As we see from Fig. 6.4, the photon number oscillates and reaches a maximum when γ and θ fulfill $\gamma = \theta + 2n \times 90°$, $n \in \mathbb{Z}$. Thus, the photon number is maximal when the displacement of the squeezed coherent state is maximal. We emphasize that the various states detected in our experiments are referred to the input of the hybrid ring. To fit to theory (Eq. (6.2)), we need to shift the reference plane of the coherent state from the hybrid ring input with phase Θ to the JPA input with phase θ. Fitting the experimental data, we retrieve $\Delta\Theta = 6.2 \pm 0.2°$ and a squeezing factor $r = 1.8 \pm 0.1$. This r value equals the value $r_{\mathrm{DP}} = 1.81 \pm 0.01$ from dual-path reconstruction for individual states.

6.1.5 State statistics

From theory, we expect that the only difference between a squeezed coherent state and the corresponding squeezed vacuum state is a displacement in phase space without any rotation or deformation. Therefore, we analyze the statistics of the variances $(\Delta X_{\mathrm{anti}})^2$ and $(\Delta X_{\mathrm{sq}})^2$ of the anti-squeezed and squeezed quadratures and that of the angle γ for the squeezed coherent states and squeezed vacuum states. As displayed in Tab. 6.2, our data show that no significant rotations or deformations are

Table 6.2: Comparison between Squeezed Coherent states (SC) and Squeezed Vacuum states (SV). The quantities B are obtained by pre-averaging over four values taken from moment reconstructions in the corresponding regions of 5×10^5 traces each. The statistics is performed over the 32 Θ- and γ-combinations shown in Fig. 6.3 and 6.4. Reprinted from Ref. [32].

B	$\mathrm{rms}(B_{\mathrm{SC}} - B_{\mathrm{SV}})$	$\mathrm{mean}(B_{\mathrm{SC}}) \pm \mathrm{std}(B_{\mathrm{SC}})$	$\mathrm{mean}(B_{\mathrm{SV}}) \pm \mathrm{std}(B_{\mathrm{SV}})$
$(\Delta X_{\mathrm{anti}})^2$	0.21	9.1 ± 0.1	9.2 ± 0.03
$(\Delta X_{\mathrm{sq}})^2$	0.007	0.095 ± 0.004	0.089 ± 0.002
γ	0.87°	–	–

present.

6.2 Coherent squeezed states (Q200 JPA)

6.2.1 PNCF calibration

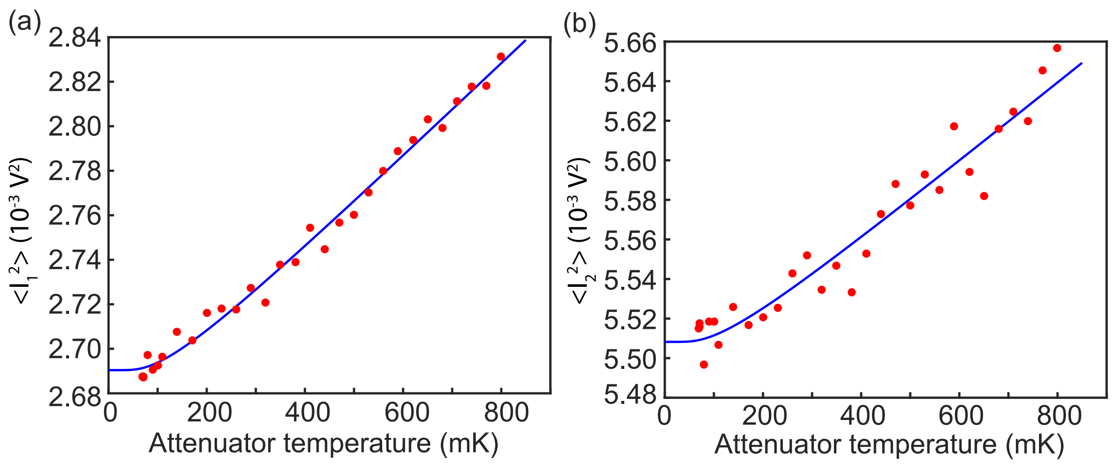

Figure 6.5: PNCF calibration for the channels I_1 and I_2. Detected $\langle I_1^2 \rangle$ (a) and $\langle I_2^2 \rangle$ (b) versus temperature of the $30\,\mathrm{dB}$-attenuator. Red dots denote experimental data. Blue lines indicate theoretical fits. A data point at each temperature represents an average over 4×10^8 samples. The JPA temperature is stabilized at $50.45\,\mathrm{mK}$.

The same method as described in Sec. 6.1.1 is used to calibrate the PNCFs of the setup for coherent squeezed state measurements. The experimental results and theoretical fits for the channels I_1 and I_2 are shown in Fig. 6.5 [1]. The number of noise photons in the two detection chains from PNCF fitting and dual-path reconstruction

[1]The loss from the 30-dB attenuator to the measurement circulator is estimated as $1.5\,\mathrm{dB}$. The loss from the measurement circulator to the input of the hybrid ring, including the JPA insertion loss, is estimated as $3\,\mathrm{dB}$.

is shown in Tab. 6.3. In Sec. 5.2.4, we already find out that chain 2 has twice the noise temperature as chain 1 when the JPA is operating in the non-degenerate mode. It is not surprising that chain 2 is more noisy than chain 1 from PNCF calibration. Later, we have found out that the main reason for this observation is the bad thermalization of the output cables inside the cryostat.

Table 6.3: Number of noise photons in two detection chains calculated from PNCF fitting and dual-path reconstruction. The uncertainties from PNCF fitting are 95% confidence bounds. The uncertainties from dual-path reconstruction are based on statistics of 400 measurements. One measurement is averaged over 4×10^8 samples. The measurement bandwidth is about $500\,\mathrm{kHz}$.

		Number of noise photons	
		PNCF fitting	Dual-path reconstruction
Chain 1	I_1 channel	19.76 ± 0.83	20.33 ± 0.06
	Q_1 channel	19.99 ± 0.74	
Chain 2	I_2 channel	43.1 ± 4.4	45.26 ± 0.14
	Q_2 channel	46.6 ± 5.3	

6.2.2 Squeezed vacuum states

The Q200 JPA is operated in the degenerate mode with an operation point $f_0 = 5.932\,\mathrm{GHz}$ and a pump power $P_\mathrm{pump} = -47.5\,\mathrm{dBm}$ which is estimated at the JPA sample box input. The pump is operated in a pulsed regime so that around half of the sample numbers in a segment correspond to the pump-on region. Both the JPA input signal and the displacement signal are off. The phase stabilization protocol described in Sec. 4.3 is implemented for the measurements. One iteration of phase stabilization, including measurements, state reconstruction and phase correction, takes about one minute. In total 400 measurements are performed for statistics. In Fig. 6.6 (a), a histogram of anti-squeezed phase of the 400 measurements is shown. Even with the phase stabilization protocol, the standard deviation of the anti-squeezed phase is 3.6° . Later we have performed some tests, and found out that phase fluctuations are mainly trigger problems with the Acqiris card. Therefore, this type of phase fluctuations in the two detection chains are correlated, and the dual-path method assumes the correlations arise from the state at the hybrid ring input. When the input state is a vacuum or thermal state, the phase fluctuations do not affect the state reconstruction. However, when the input state is a squeezed state, the effect of phase fluctuations can be modeled as thermal photons added to the input state from a single dual-path reconstruction. We denote the number of

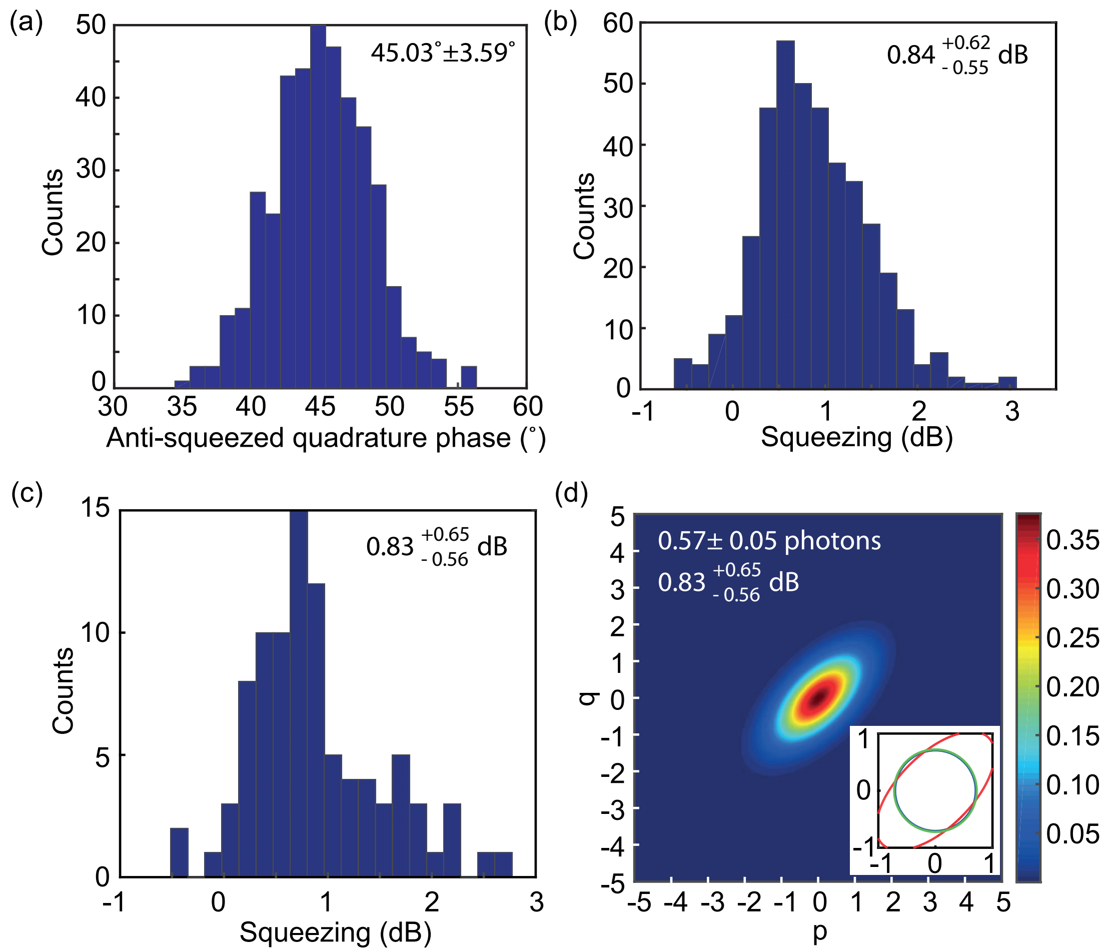

Figure 6.6: (a) Histogram of the anti-squeezed phase of 400 measurements. One measurement contains an average over 4×10^8 samples. The pump tone is operated in a pulsed mode. The pump-on region corresponds to about half of the samples in a segment. (b) Histogram of the squeezing level of 400 measurements. (c) Histogram of the squeezing level for measurements with the anti-squeezed phase in the range of $44° - 46°$. Numbers in (a)-(c) show the statistics of the corresponding quantity. Statistics of the squeezing level is taken on a linear scale and converted into a logarithm scale. (d) Wigner function based on dual-path reconstruction from the selected measurements in (c). The inset shows the $1/\mathrm{e}$ contour of the Wigner functions for an ideal vacuum state (blue), experimental vacuum state (green), and squeezed vacuum state (red). The numbers show the statistics of the squeezing level and number of photons in the state. p and q are dimensionless quadrature variables spanning the phase space. The JPA temperature is stabilized at $50.45\,\mathrm{mK}$.

thermal photons as n_{th} for later discussions. Here we point out that the thermal photons n_{th} are added to the hybrid ring input state, not to the JPA input state.

A histogram of the squeezing level for these 400 measurements is shown in Fig. 6.6. Due to the instability of the setup, the squeezing level also fluctuates. Nevertheless from statistics it is clear that the state is squeezed below vacuum. The average squeezing level is $\mathcal{S} = 0.84^{+0.62}_{-0.55}\,\mathrm{dB}$. Here, the statistics is performed on a linear scale and converted into a logarithm scale. To reconstruct a Wigner function, we select the measurements with the anti-squeezed phase within one degree offset from the set value. A histogram of the squeezing level for selected measurements is shown in Fig. 6.6(c). The reconstructed Wigner function averaged over selected measurements is shown in Fig. 6.6(d). A squeezed vacuum state with anti-squeezed phase $\gamma = 45°$ is obtained. If we model the experimental squeezed vacuum state with a thermal squeezed state [2], including the phase fluctuations of the anti-squeezed quadrature as Gaussian noise, we find the number of thermal photons [3] $n_{\mathrm{th}} = 0.24$, and the squeeze factor $r = 0.55$. These thermal photons n_{th} mainly come from the phase fluctuations in measurements for a single dual-path reconstruction. They are also partially from the JPA losses, the connection losses between the JPA and hybrid ring, the spurious correlations in the detection setup and phase fluctuations in multi dual-path reconstructions used for averaging. When $n_{\mathrm{th}} \approx 0$, $r = 0.55$ gives a squeezing level of $4.8\,\mathrm{dB}$.

6.2.3 Displaced squeezed vacuum states

The Q200 JPA is operated at the same operation point and pump power as in Sec. 6.2.2, and the pump power is still operated in a pulsed mode. Now a coherent signal is supplied at the coupled port of the directional coupler, which is installed at the hybrid ring input. When the pump is off, a coherent signal is present at the hybrid ring input. When the pump is on, a squeezed vacuum state generated by the JPA is displaced by the coherent signal from the directional coupler, and a coherent squeezed state is obtained. In Fig. 6.7, reconstructed Wigner functions of experimental coherent squeezed state displaced in the direction of $\theta = 45°$ (a) and $\theta = 135°$ (b) are presented. Sketches of 1/e contours of the coherent states

[2] A thermal squeezed state means that thermal photons are added to a squeezed state after the squeeze operator. A squeezed thermal state means that the squeeze operator is applied to a thermal state. For the former, thermal photons are added to the hybrid ring input (JPA output). In contrast, for the latter thermal photons are added to the JPA input.

[3] For comparison, with the FPGA based dual-path setup for the squeezed state detection in Sec. 6.1 the number of thermal photons is obtained to $n_{\mathrm{th}} = 0.12$.

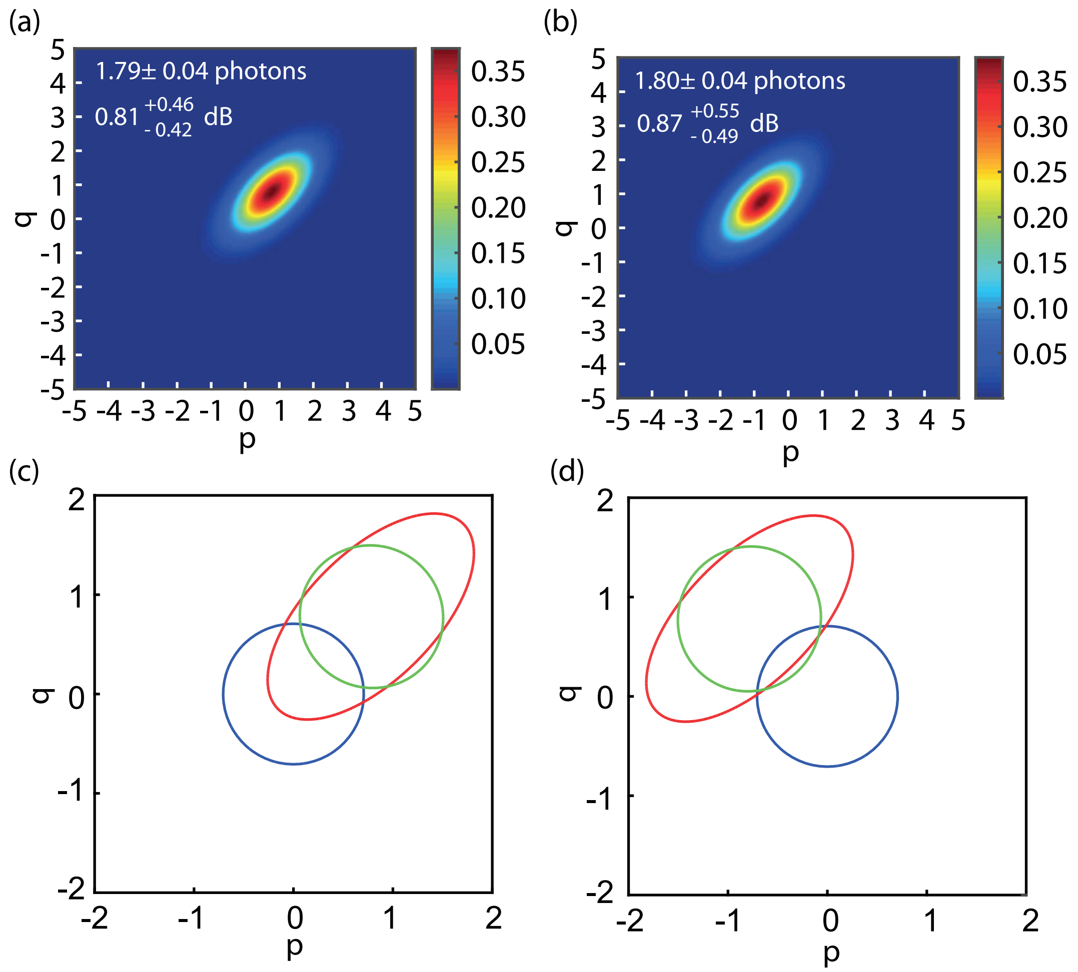

Figure 6.7: (a)-(b), Reconstructed Wigner functions of coherent squeezed states averaged over selected measurements out of 400 measurements. Each measurement is averaged over 4×10^8 samples. A measurement is selected if $44 < \theta < 46°$ and $44° < \gamma < 46°$ for (a), $134 < \theta < 136°$ and $44° < \gamma < 46°$ for (b). The numbers show the statistics of squeezing level and number of photons in the states. (c)-(d), Sketch of $1/\mathrm{e}$ contours of ideal vacuum states (blue), experimental coherent states (green), experimental coherent squeezed states (red) in (a) and (b). The photon number in the coherent state (green) is $n_\mathrm{C} = 1.24 \pm 0.04$ for (c), $n_\mathrm{C} = 1.25 \pm 0.04$ for (d). p and q are dimensionless quadrature variables spanning the phase space. n, r, θ and ϕ are from Eqs. (2.32)-(2.42). Statistics of the squeezing level is taken on a linear scale and converted into a logarithm scale. The JPA temperature is stabilized at $50.45\,\mathrm{mK}$.

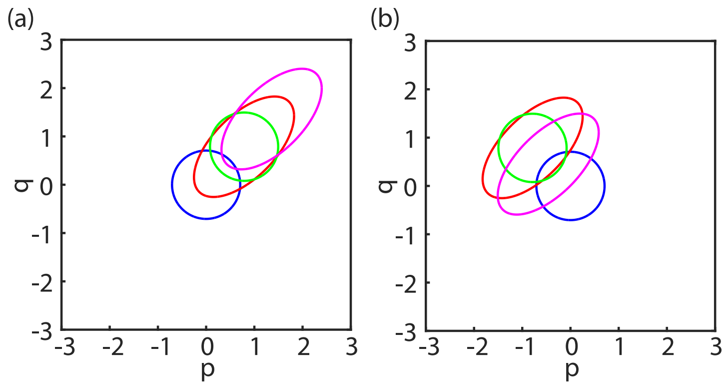

Figure 6.8: Sketch of $1/\mathrm{e}$ contours of ideal vacuum states (blue), ideal coherent states (green), coherent thermal squeezed states (red) and squeezed coherent thermal states (magenta). $r = 0.55$ corresponds to $4.8\,\mathrm{dB}$ of squeezing without phase fluctuations. The displacement photon number is $n = 1.24$, and the thermal photon number is $n_{\mathrm{th}} = 0.24$. $\gamma = 45$. $\theta = 45$ for (a) and $\theta = 135$ for (b). Phase fluctuations with a standard derivation of $3.6°$ for the anti-squeezed angle and displacement angle of coherent thermal squeezed states and squeezed coherent thermal states are taken into account by Gaussian noise. p and q are dimensionless quadrature variables spanning the phase space.

(green) and coherent squeezed states (red) are shown in (c) and (d). Blue circles denote theoretical vacuum states. With different displacement angles ($\theta = 45°$ for (a) and (c), and $\theta = 135°$ for (b) and (d)), the shape of the coherent squeezed state remains the same as the squeezed vacuum state in Fig. 6.6(d). Now a coherent thermal squeezed state, which is a displaced thermal squeezed state, is used to model the experimental data (Fig. 6.7(a), (b)). This gives the number of thermal photon $n_{\mathrm{th}} = 0.24$ and squeeze factor $r = 0.55$, which corresponds to $4.8\,\mathrm{dB}$ of squeezing with $n_{\mathrm{th}} = 0$. These results are the same as for the experimental squeezed vacuum state in Sec. 6.2.2.

In Fig. 6.8 we compare the difference between a thermal coherent squeezed state and a thermal squeezed coherent state [4] with $n_{\mathrm{th}} = 0.24$ and $r = 0.55$. The final states in both cases have the same shape, but different locations in phase space. The differences are also easy to understand from state moments in Eqs. (2.32)-(2.42).

6.2.4 Squeezing versus displacement

To understand how a coherent squeezed state depends on displacement including the effect of phase noise, we have performed the simulations shown in Fig. 6.9. In

[4] For the former, thermal photons are added to a coherent squeezed state. For the latter, thermal photons are added to a squeezed coherent state.

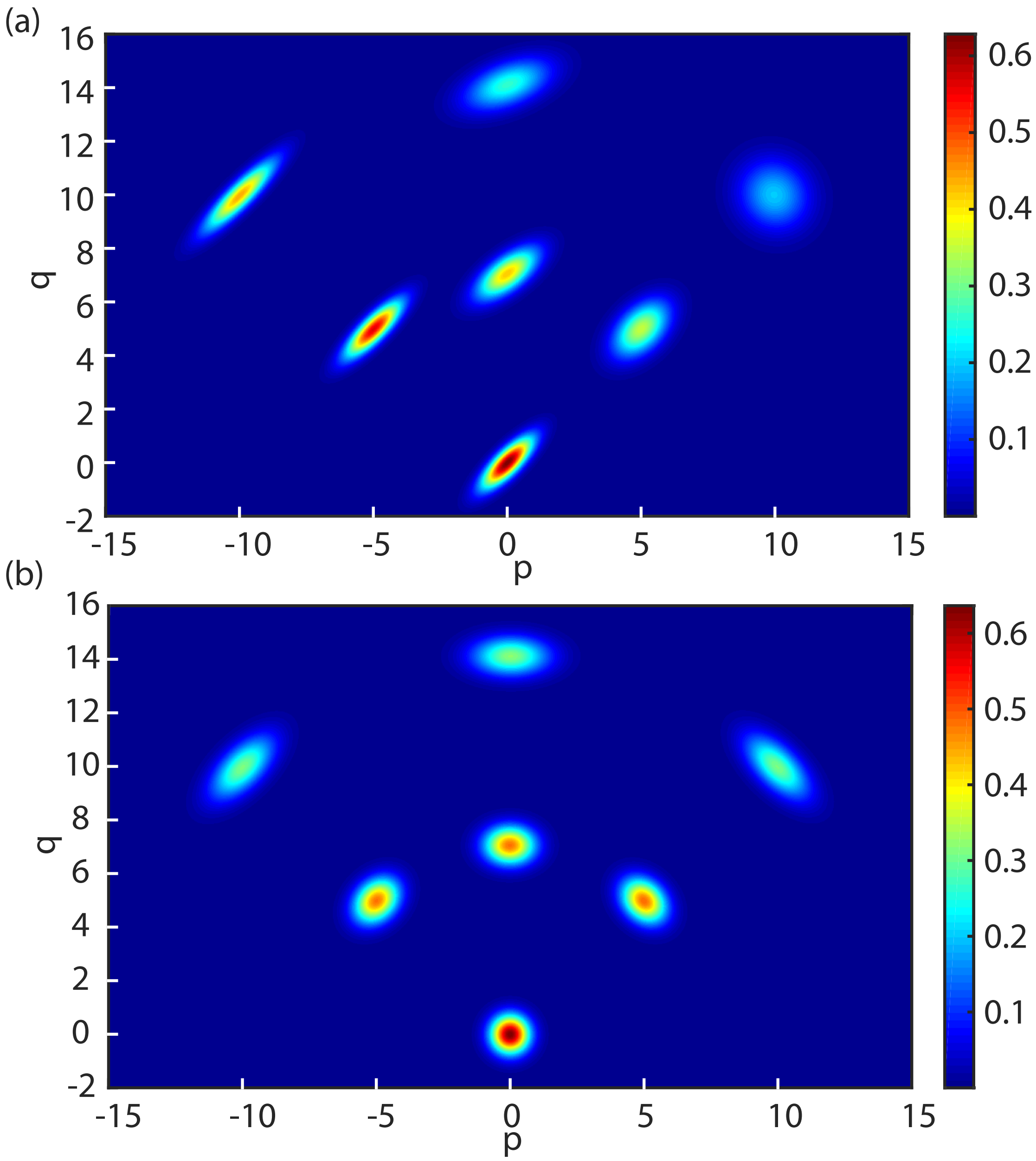

Figure 6.9: Simulations of coherent squeezed states (a) and coherent states (b) as a function of displacement in the presence of phase noise. (a) Superposition of 7 Wigner functions of coherent squeezed states. Each state has $\gamma = 45°$ and $r = 0.55$. The displacement directions are $\theta = 45°$, $90°$, and $135°$ with the amount of displacement in photon number $n = 0$, 50 and 200. (b) Superposition of 7 Wigner functions of coherent states with $n = 0$, 50 and 200. Gaussian noise is added to γ and θ with a standard deviation of $3.6°$. For each state, 2000 averages are performed. Thermal photons during a single dual-path reconstruction are ignored, $n_{\text{th}} = 0$.

Fig. 6.9(a), a squeezed vacuum state with $r = 0.55$ and $\gamma = 45$ is displaced in directions of $\theta = 45°$, $90°$, and $135°$ with an amount of displacement $n = 0$, 50 and 200. Gaussian noise with a standard derivation of 3.6° has been added to γ and θ. Similarly, different coherent states with $n = 0$, 50 and 200, and $\theta = 45°$, $90°$, and 135° including Gaussian noise added to θ are shown in Fig. 6.9(b). The corresponding squeezing levels are listed in Tab. 6.4. The displacement phase noise becomes more prominent at larger displacement. This leads to a decrease of the squeezing level versus displacement.

Now we repeat the measurements in Fig. 6.7(b) with different powers of the displacement signal. For each displacement power, 400 measurements are performed and measurements that fulfill the conditions $134 < \theta < 136°$ and $44° < \gamma < 46°$ are selected to calculate the squeezing level. The squeezing level versus displacement for experimental coherent squeezed states and coherent states is presented in Fig. 6.10(a) and (b), respectively. In contradiction to theory, the experiments show an increase of the squeezing level versus displacement for both the coherent squeezed states (Fig. 6.10(a)) and the coherent states (Fig. 6.10(b)).

Table 6.4: Simulations of the squeezing level (dB) of coherent squeezed states and coherent states as a function of the displacement in the presence of phase noise. Gaussian noise with a standard derivation of 3.6° is added to γ and θ. The displacement in photon number is represented by n. Phase noise in a single measurement effectively adds thermal photons to the input state based on the dual-path method. This effect is considered through the number of thermal photons n_{th}. For coherent squeezed states, $\gamma = 45°$, $r = 0.55$, which gives a squeezing level of 4.78 dB with $n_{\mathrm{th}} = 0$.

		Coherent squeezed states			Coherent states		
		n=0	n=50	n=100	n=0	n=50	n=100
$\mathcal{S}$(dB)	$\theta = 45°$	4.65	-0.37	-4.77	0	-0.006	-0.02
with	$\theta = 90°$	4.65	1.69	-0.69	0	-0.006	-0.02
$n_{\mathrm{th}} = 0$	$\theta = 135°$	4.65	4.63	4.59	0	-0.006	-0.02
$\mathcal{S}$(dB)	$\theta = 45°$	0.85	-2.04	-5.4	-1.703	-1.707	-1.72
with	$\theta = 90°$	0.85	-0.64	-2.2	-1.703	-1.707	-1.72
$n_{\mathrm{th}} = 0.24$	$\theta = 135°$	0.85	0.84	0.81	-1.703	-1.707	-1.72

We expect this contradiction to arise from errors in the estimation of the PNCFs. In Fig. 6.11, we scale the PNCF of chain 2 with a factor y. We have found out that when $y > 1.2$ or $y < 0.95$, the reconstructed Wigner functions of a squeezed coherent state is unphysical. When y increases from 0.95 to 1.08, the slope of the squeezing level versus displacement curve decreases. For $y = 1.08$ the curve shows

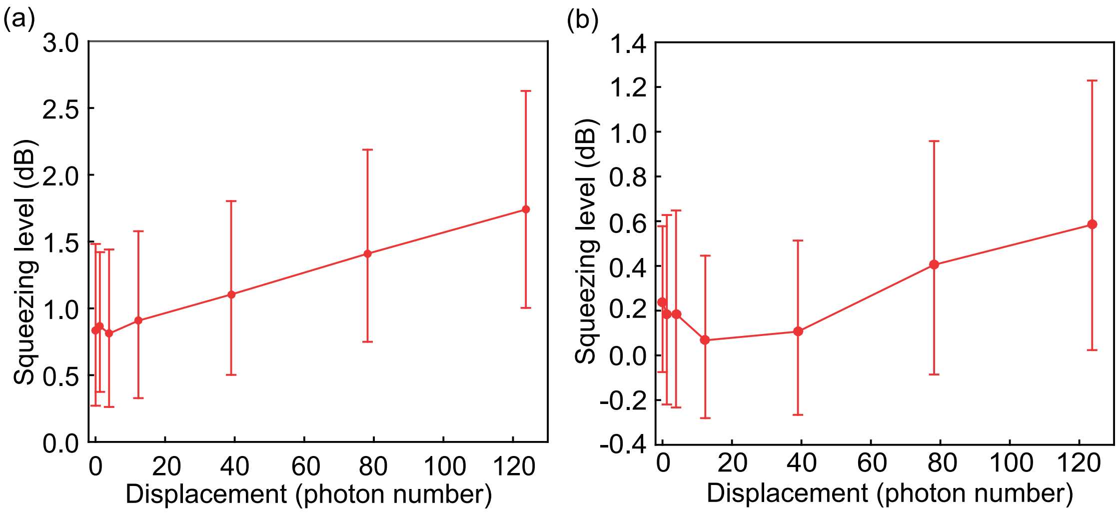

Figure 6.10: Squeezing level versus displacement for experimental coherent squeezed states (a) and coherent states (b). Each data point is averaged over selected measurements out of 400 measurements. Each measurement is averaged over 4×10^8 samples. A measurement is selected if $134 < \theta < 136°$ and $44° < \gamma < 46°$. The pump is pulsed. Half of each measurement corresponds to a coherent squeezed state and the other half corresponds to a coherent state. The lines are guides to the eye. The JPA temperature is stabilized at $50.45\,\mathrm{mK}$.

a slow decrease of the squeezing level depending on the displacement in agreement with theory. When y increases from 1.08 to 1.2, the slope of the squeezing level versus displacement curve again increases. At zero displacement, the experimental coherent state is slightly squeezed below vacuum. This is mainly due to the spurious correlations in the setup. The dual-path method assumes perfect uncorrelated noises, and considers that any spurious correlations in the setup originate from the signal.

6.3 Coherent squeezed states (new JPA)

In this section, some of the main results of a follow up project with another JPA sample (new JPA) are presented. The data presented here is discussed in detail in the upcoming master thesis of Stefan Pogorzalek. The cryogenic setup is the same as depicted in Fig. 4.2, except for a larger number of silver wires are used to thermalize the output cables. A few modifications have been made to the room temperature setups in Fig. 4.11. First, the minicircuit type room temperature amplifiers have been replaced with Miteq type amplifiers and their temperatures are also PID controlled. A bandpass filter ($11.3 - 11.7\,\mathrm{MHz}$) is installed at each ADC input.

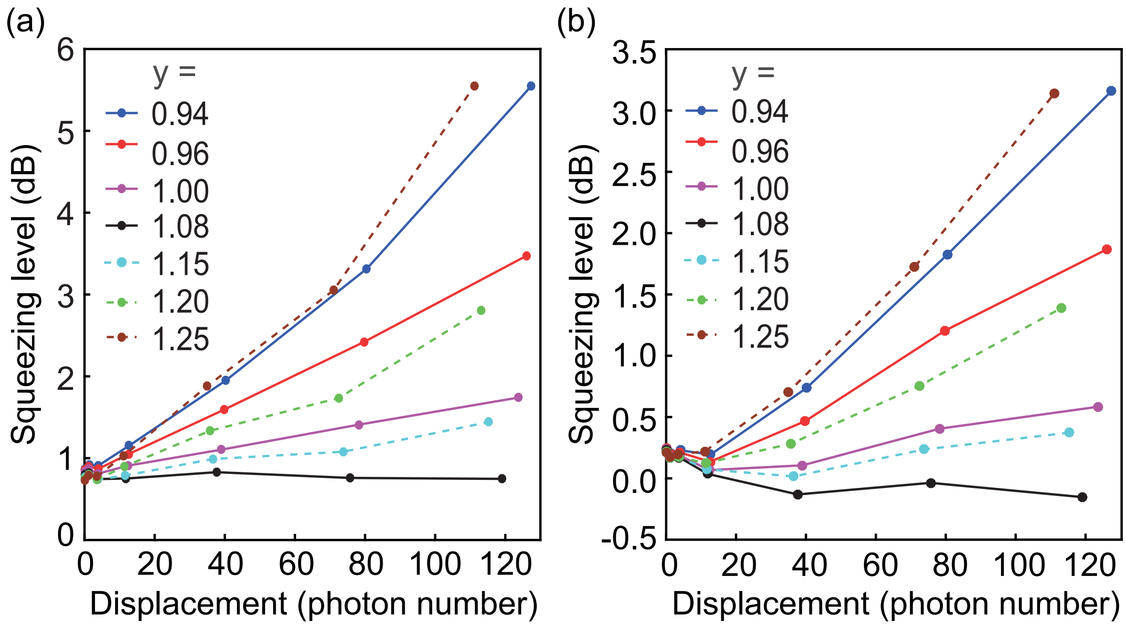

Figure 6.11: Squeezing level versus displacement for experimental coherent squeezed states (a) and coherent states (b) with different scaling factors y for PNCFs of chain 2. $y = 1$ gives the curves in Fig. 6.10. Error bars have similar scales as in Fig. 6.10. They are omitted for clarity. The lines are guides to the eye.

After thermalizing the output cables with more silver wires, we could obtain more reliable PNCF measurements. From the PNCF measurements [5] (Fig. 6.12), we determine the number of noise photons added by the detection chains, including the hybrid ring, HEMT amplifier, circulators, room temperature components, etc., is about 29.1 ± 1.2 for chain 1, and 27.9 ± 0.9 for chain 2 within a measurement bandwidth of 800 kHz. The uncertainties are 95% confidence bounds from fitting.

Next we stabilize the 30-dB attenuator at 60 mK, and turn on the JPA pump signal while keeping the displacement signal off. This measurement is performed at different signal gains. At each signal gain, 150 measurements have been taken. The measurements fulfilling $44^\circ < \gamma < 46^\circ$ are selected to calculate the statistics of the squeezing level and photon number in the state. As shown in Fig. 6.13(a), the increase of signal gain, which corresponds to an increase of pump power, causes an increase of the squeezing level. At 1 dB of signal gain, we achieve a maximum squeezing level of $1.43^{+0.77}_{-0.65}$ below vacuum. However, if we further increase the signal gain, the state is more sensitive to phase noise and the squeezing level decreases again. The dependence of the number of photons in the state on the signal gain

[5] The loss from the 30-dB attenuator to the measurement circulator is estimated as 0.15 dB. The loss from the measurement circulator to the input of the hybrid ring, including the JPA insertion loss, is estimated as 0.98 dB.

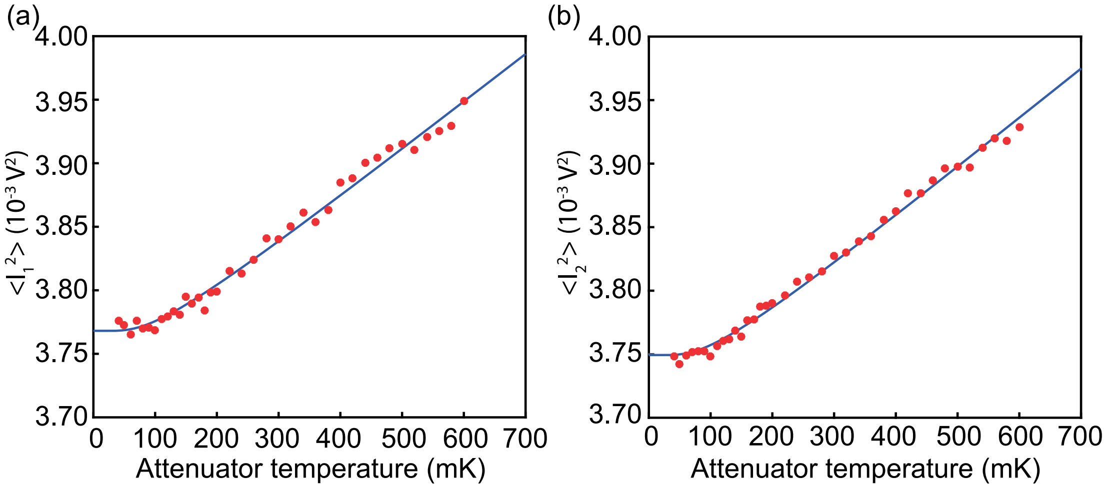

Figure 6.12: PNCF calibration for new JPA measurement setup. Detected $\langle I_1^2 \rangle$ (a) and $\langle I_2^2 \rangle$ (b) versus the temperature of the $30\,\mathrm{dB}$-attenuator. Red dots denote experimental data. Blue lines indicate theoretical fits. Every data point at constant temperature represents an average of 1.12×10^9 samples. FIR digital filters are not used. The measurement bandwidth is about $800\,\mathrm{kHz}$. The JPA working point is $f_0 = 5.51\,\mathrm{GHz}$. The JPA temperature is stabilized at $40\,\mathrm{mK}$.

shows a continuous increase (Fig. 6.13(b)).

Next the pump power is set to a value which corresponds to a 1 dB signal gain. A displacement signal with $\theta = 135°$ is turned on. Therefore, a squeezed vacuum state or a vacuum is displaced in the direction of $\theta = 135°$. The squeezing level of the experimental coherent squeezed states (Fig. 6.14(a)) stays almost constant up to a displacement of 33 photons. The squeezing level of the experimental coherent states (Fig. 6.14(b)) shows a slow decrease for increasing displacement. This means that the quadrature variance of the coherent state increases for increasing displacement due to phase fluctuations.

According to our previous studies [39, 40], sending a squeezed state into a beam splitter, the output state of the beam splitter contains path entanglement. Based on the beam splitter relations (Eqs. (3.7)-(3.8)) and the signal moments reconstructed with the dual-path method, the moments of the hybrid output state can be evaluated. Therefore, the negativity kernel $\tilde{\mathcal{N}}$ as a witness for arbitrary bipartite entanglement (Appendix E) could be calculated. We calculate the corresponding negativity kernel for the datasets in Fig 6.14(a), and plot the results in Fig. 6.15. As expected, the output state of the hybrid ring shows path entanglement. Up to a displacement of 33 photons of the coherent squeezed states, which is the hybrid ring input state, the negativity kernel is almost constant.

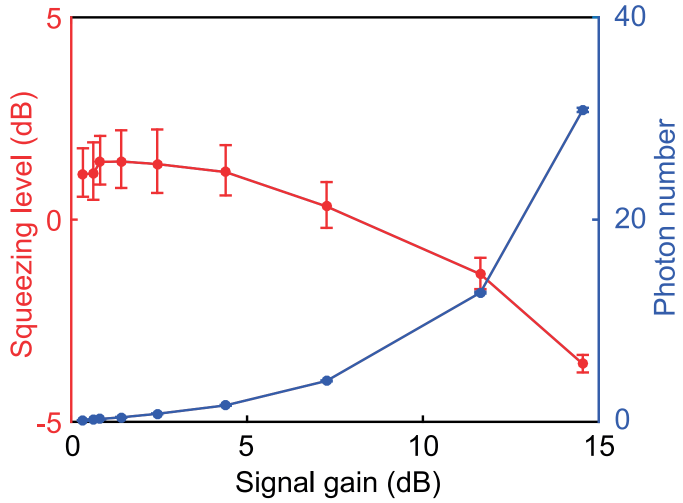

Figure 6.13: Experimental squeezing level (red) and photon number (blue) as a function of the signal gain with the $30\,\mathrm{dB}$-attenuator temperature at $60\,\mathrm{mK}$. One data point (dots) is averaged over 1.12×10^9 samples. The JPA working point is $f_0 = 5.51\,\mathrm{GHz}$. The The lines are guides to the eye. The error bars are of a statistical nature. The JPA temperature is stabilized at $40\,\mathrm{mK}$.

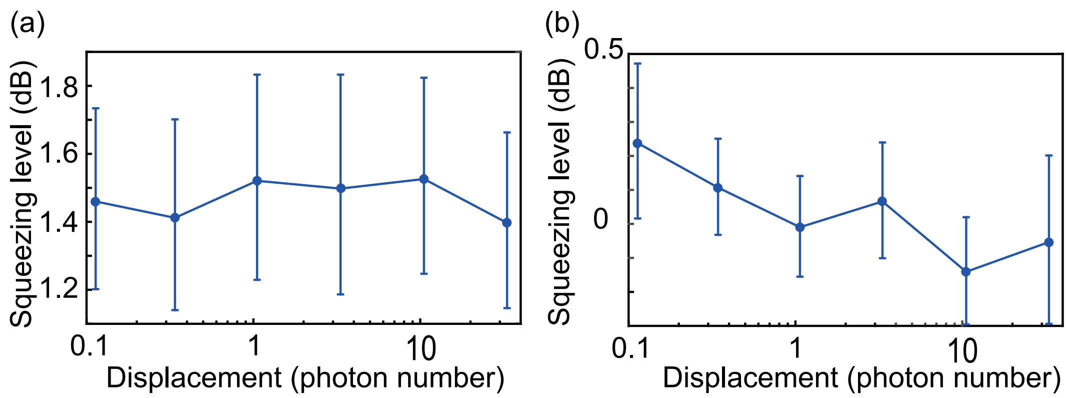

Figure 6.14: Squeezing level of experimental coherent squeezed states (a) and coherent states (b) as a function of displacement. The $30\,\mathrm{dB}$-attenuator temperature is at $60\,\mathrm{mK}$. One data point (dots) is an average over 1.12×10^9 samples. The JPA working point is $f_0 = 5.537\,\mathrm{GHz}$. The The lines are guides to the eye. The error bars are of a statistical nature. The JPA temperature is stabilized at $40\,\mathrm{mK}$.

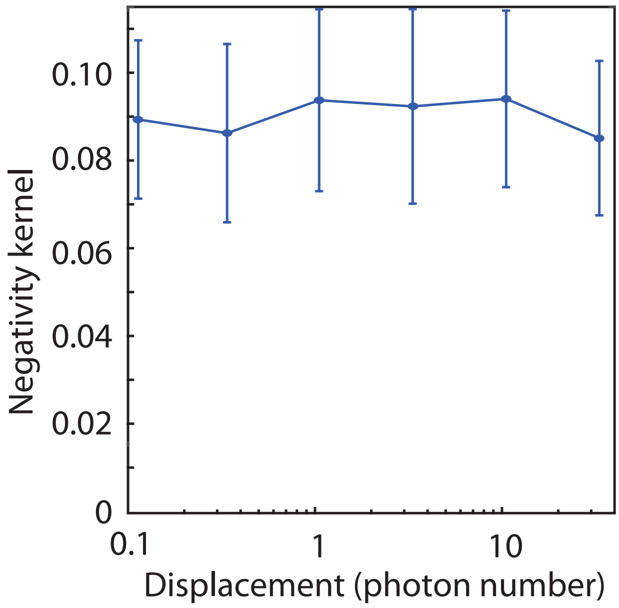

Figure 6.15: Negativity kernel of the hybrid output state as a function of displacement based on the dual-path method for the new JPA sample. The datasets in Fig 6.14(a) are used for the calculations. The lines are guides to the eye. The error bars are of a statistical nature.

Chapter 7

Summary and outlook

Quantum teleportation with propagating microwave signals is an important application in the scope of quantum communication and computation in the microwave domain. In this work, we have investigated the displacement operation, which is widely used in quantum teleportation, remote state preparation, etc., in the context of squeezed coherent states and coherent squeezed states.

For the generation of squeezed states we have used flux-driven JPAs. Therefore, we have carefully characterized two flux-driven JPAs, Q600 JPA and Q200 JPA. Interestingly, the flux dependence of the resonance frequency for Q600 JPA shows a hysteretic behavior. To explain this phenomenon, a method to determine the JPA resonance frequency from an evaluation of the flux dependence of the dc-SQUID critical current has been developed.

With an FPGA based dual-path setup, which splits a signal into two detection chains, we can reconstruct the moment matrix of the signal and the noise added by the two detection chains. By sending coherent states into a JPA (Q300 JPA) operating in the degenerate mode, squeezed coherent states are obtained. The final displacement and photon number of the squeezed coherent states depend on both the anti-squeezed phase and displacement direction. When the anti-squeezed phase is parallel to the displacement direction, the final displacement and photon number are maximal. When the anti-squeezed phase is perpendicular to the displacement direction, the final displacement and photon number are minimal. The squeezed coherent states with different displacements and anti-squeezed phases have an average squeezing level of 4.2 dB below vacuum.

With an Acqiris card based dual-path setup, we have investigated the displacement operation applied with a directional coupler, whose coupled port is biased with a coherent signal. A squeezed state, generated with a JPA (Q200 JPA), gets displaced after passing through the directional coupler. Although with experimental imperfections, such as the additional noise photons in chain 2, phase fluctuations, and the limited detection efficiency, a squeezed vacuum state with $\mathcal{S} = 0.83^{+0.65}_{-0.56}$dB gets displaced, and the squeezing level of the final coherent squeezed state becomes $\mathcal{S} = 0.81^{+0.46}_{-0.42}$ dB with $\theta = 45°$ and displacement $n = 1.24$, and $\mathcal{S} = 0.87^{+0.55}_{-0.49}$ dB with $\theta = 135°$ and displacement $n = 1.25$. For the Q200 JPA, we have observed an increase of the squeezing level as a function of displacement due to an incorrect estimate of the PNCFs. After improving the setups, more reliable PNCF measurements can be obtained. With another JPA sample (new JPA), the squeezing level of coherent squeezed states stays almost constant up to a displacement of 33 photons, with $\gamma = 45°$ and $\theta = 135°$.

Due to setup imperfections, such as some spurious correlations of the two dual-path detection chains, the quadrature variances of our experimental coherent states do not equal 0.25. At zero displacement $n = 0$, experimental coherent states show a squeezing level of $\mathcal{S} = 0.25$ dB. The squeezing level of experimental coherent states decreases as a function of displacement, which means the quadrature variances increase with increasing displacement, due to the fact that at larger displacement, the state gets more sensitive to phase noise.

In circuit-QED systems, 10 dB of squeezing level [29] has been achieved by using a SQUID-array in a cavity consisting of 480 Josephson junctions. Also, 12 dB of squeezing level [34] has been realized with coupled nonlinear resonators. In our case, one limiting factor of the detected squeezing level is the detection efficiency. For the Acqiris card based dual-path setup, which is used for the Q200 JPA measurements, the trigger problems with the Acqiris card lead to phase fluctuations with a standard deviation of 3.6°. The phase fluctuations within a single dual-path reconstruction can be modeled as thermal photons added to the squeezed states and significantly reduce the squeezing level. At the same time, the phase fluctuations between different dual-path reconstructions which are used for averaging further reduce the squeezing level. To improve the detection efficiency, first, the trigger problems need to be solved. Second, FPGA instead of the Acqiris card can be used to process the data in real time. Third, by reducing the losses of the output lines, such as reducing the cable and connector losses, the detection efficiency can be improved. Fourth, reducing the thermal photons added by the detection chains, such as using a low noise JPA as the pre-amplifier of the HEMT amplifier, is another solution. Meanwhile, both the cryogenic and room temperature setups have to be stabilized. For example, more stable microwave sources can reduce the phase fluctuations and improve the detected squeezing level.

Another limiting factor of the detected squeezing level is the JPA sample. First, reducing the internal losses of the JPA can increase the squeezing level. Second, SQUID-arrays [34, 99] can be used to increase the maximum allowed input power, and therefore increase the squeezing level.

In this work, the displacement operation, which is one of the building blocks for quantum teleportation with propagating microwaves, has been studied. As the next step, another building block for quantum teleportation namely the two-mode squeezed state as EPR pair is highly interesting to be investigated. By sending two squeezed states with orthogonal anti-squeezed quadratures into a 50/50 beam splitter, a two-mode squeezed state can be generated. Quantum correlations exist between the two modes propagating along the beam splitter outputs. The correlation properties of the two-mode squeezed state for different time lags between the two modes determine the configuration of a delay line for the application in quantum teleportation and remote state preparation protocols.

Next, the classical communication from Alice to Bob could be investigated with the remote state preparation protocol, which is described in this thesis. This protocol also provides a method to remotely prepare a squeezed state. The squeezing level of the squeezed state prepared with this protocol is determined by the squeezing level of the input state and the setup configuration, such as the setup losses, noise photons and temporal mode matching. A higher squeezing level of the input state can in turn allows for larger setup losses and an increased number of thermal photons. Finally, by combining all the building blocks — two-mode squeezed state generation, JPA based low noise detection, classical communication and displacement operation with a directional coupler — quantum teleportation with propagating microwaves could come into experimental reach.

Appendix A

FPGA based dual-path setup

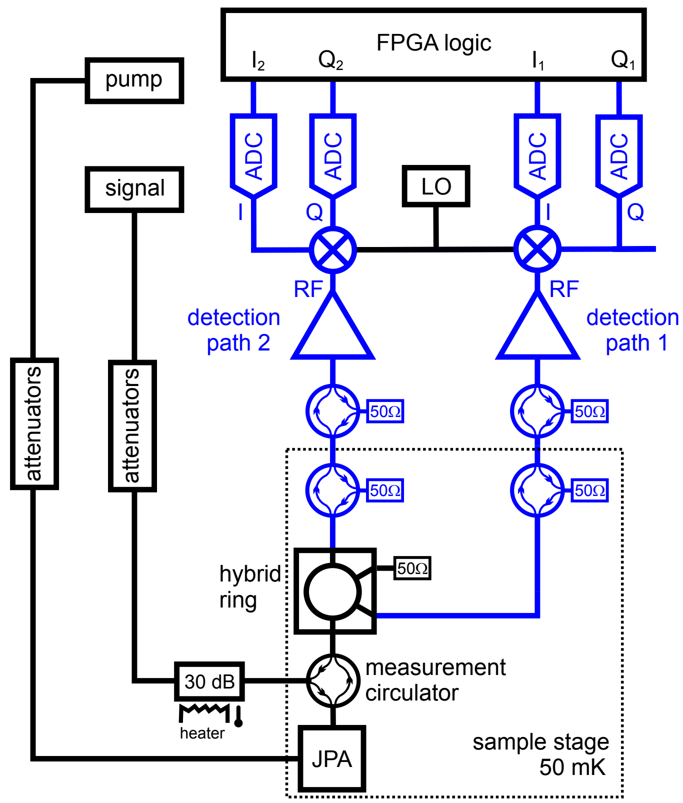

Figure A.1: Simplified schematic of the dual path setup for Q300 JPA. The triangular symbols denote the detection chains, the circles with crosses are IQ-mixers and the boxes labeled ADC are analog-to-digital converters. LO, pump, and signal denote the microwave sources for local oscillator, pump, and signal frequency. The heatable $30\,\mathrm{dB}$-attenuator is thermally weakly coupled to the sample stage. In addition to the temperature control of this attenuator, the JPA sample temperature can be stabilized independently. For simplicity, isolators, IF amplifiers and filters are omitted in the sketch. Reprinted figure from Ref. [32].

Appendix B

Acqiris card based dual-path receiver

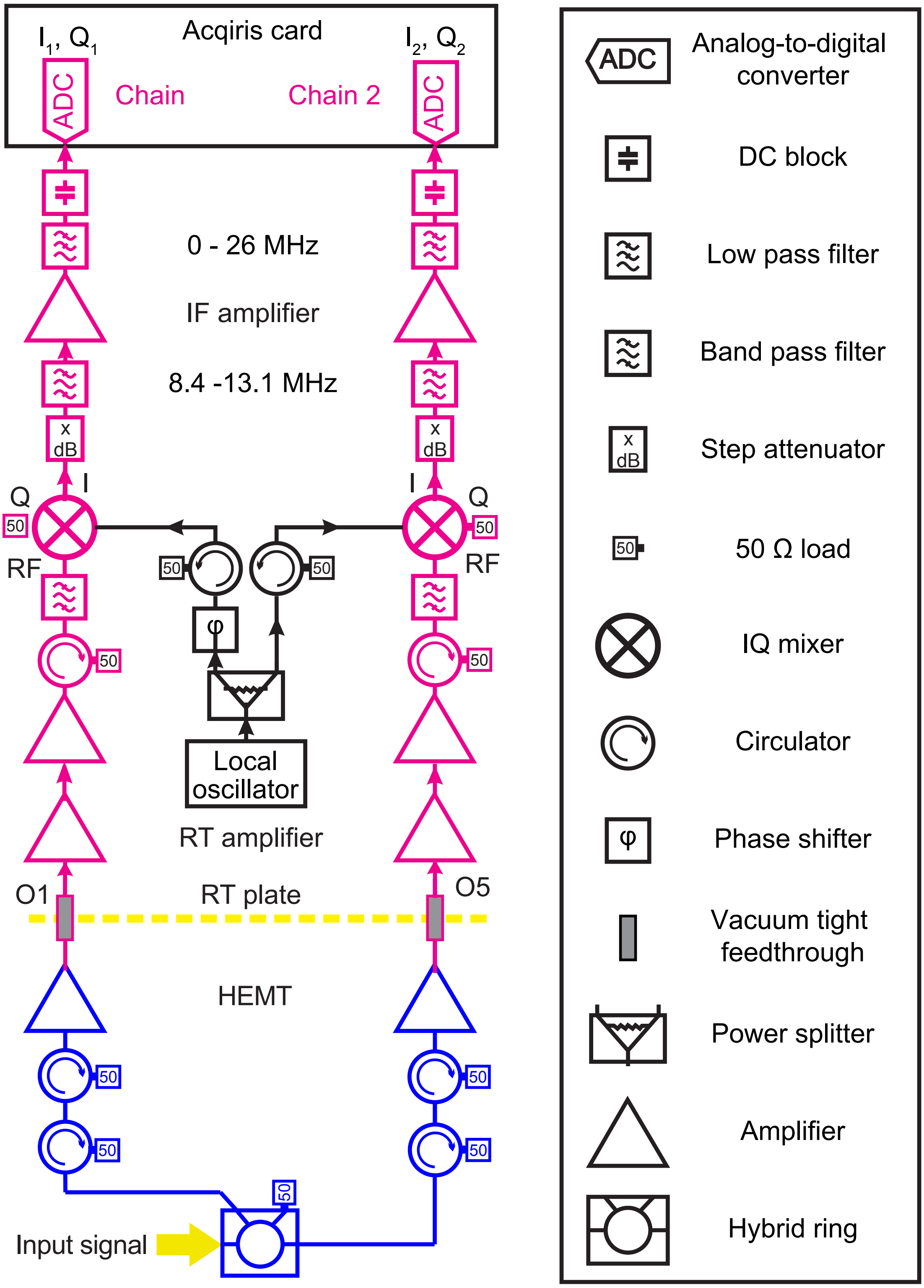

Figure B.1: Schematic of the Acqiris card based dual-path receiver for measurements with Q200 JPA. Blue color indicates the cryogenic part, and magenta color indicates the room temperature part.

Appendix C

Gaussianity and higher order cumulants

The discussions in this section are based on the supplementary material from Ref. [39]. In order to check whether the states we reconstruct are consistent with Gaussian states, we evaluate the $(l+m)^{\text{th}}$ order cumulants $\langle\langle(\hat{a}^\dagger)^l\hat{a}^m\rangle\rangle$ for $l+m\leq 4$ and $l,m\in\mathbb{N}_0$. Equivalently to the moments, the cumulants describe a probability distribution. The definition of cumulant for a quantum state with density matrix ρ can be written as [85, 86]

$$\begin{aligned}&\langle\langle(\hat{a}^\dagger)^l\hat{a}^m\rangle\rangle \equiv\\ &\frac{\partial^l}{\partial(i\beta^*)^l}\frac{\partial^m}{\partial(i\beta)^m}\left[\frac{\beta\beta^*}{2}+\ln\mathrm{Tr}\left(e^{(i\beta^*\hat{a}^\dagger+i\beta\hat{a})}\rho\right)\right]_{\beta,\beta^*=0}.\end{aligned} \tag{C.1}$$

Only Gaussian states have a finite number of nonzero cumulants. More specifically, all their cumulants vanish for $l+m>2$. In other words, finding a nonzero cumulant of 3^{rd} or higher order implies that the state is not Gaussian. Despite not being a strict proof, the fact that the 3^{rd} and 4^{th} order cumulant are very small or vanish in an experimental reconstruction constitutes a reasonable indication that the reconstructed state is Gaussian.

Appendix D

Dual-path state reconstruction

The discussions in this section are based on the supplementary material from Ref. [39]. Based on the recorded noisy quadrature moments $\langle I_1^j I_2^k Q_1^m Q_2^n \rangle$, where $j, k, m, n \in \mathbb{N}_0$, the reconstructed signal moments are

$$
\begin{aligned}
&\big\langle (\hat{a}^\dagger)^l \hat{a}^m \big\rangle_{l_1,m_1} = (-1)^{l-l_1+m-m_1} \big\langle (\hat{S}_1^\dagger)^{l_1} (\hat{S}_2^\dagger)^{l-l_1} \hat{S}_1^{m_1} \hat{S}_2^{m-m_1} \big\rangle \\
&- \sum_{k_1=0}^{l_1} \sum_{k_2=0}^{l-l_1} \sum_{j_1=0}^{m_1} \sum_{j_2=0}^{m-m_1-1} \sum_{k_1'=0}^{l_1-k_1} \sum_{k_2'=0}^{l-l_1-k_2} \sum_{j_1'=0}^{m_1-j_1} \sum_{j_2'=0}^{m-m_1-j_2} \binom{l_1}{k_1} \binom{l-l_1}{k_2} \binom{m_1}{j_1} \binom{m-m_1}{j_2} \\
&\quad \times \binom{l_1-k_1}{k_1'} \binom{l-l_1-k_2}{k_2'} \binom{m_1-j_1}{j_1'} \binom{m-m_1-j_2}{j_2'} (-1)^{l-l_1+m-m_1+j_2+k_2} \\
&\quad \times \big\langle (\hat{a}^\dagger)^{k_1+k_2}\, \hat{a}^{j_1+j_2} \big\rangle \big\langle (\hat{v}^\dagger)^{k_1'+k_2'}\, \hat{v}^{j_2'+j_1'} \big\rangle \big\langle \hat{V}_1^{l_1-k_1-k_1'}\, (\hat{V}_1^\dagger)^{m_1-j_1-j_1'} \big\rangle \big\langle \hat{V}_2^{l-l_1-k_2-k_2'} (\hat{V}_2^\dagger)^{m-m_1-j_2-j_2'} \big\rangle \\
&- \sum_{k_1=0}^{l_1} \sum_{k_2=0}^{l-l_1} \sum_{j_1=0}^{m_1-1} \sum_{k_1'=0}^{l_1-k_1} \sum_{k_2'=0}^{l-l_1-k_2} \sum_{j_1'=0}^{m_1-j_1} \binom{l_1}{k_1} \binom{l-l_1}{k_2} \binom{m_1}{j_1} \binom{l_1-k_1}{k_1'} \binom{l-l_1-k_2}{k_2'} \binom{m_1-j_1}{j_1'} \\
&\quad \times (-1)^{l-l_1+k_2} \big\langle (\hat{a}^\dagger)^{k_1+k_2}\, \hat{a}^{j_1+m-m_1} \big\rangle \big\langle (\hat{v}^\dagger)^{k_1'+k_2'}\, \hat{v}^{j_1'} \big\rangle \big\langle \hat{V}_1^{l_1-k_1-k_1'}\, (\hat{V}_1^\dagger)^{m_1-j_1-j_1'} \big\rangle \big\langle \hat{V}_2^{l-l_1-k_2-k_2'} \big\rangle \\
&- \sum_{k_1=0}^{l_1} \sum_{k_2=0}^{l-l_1-1} \binom{l_1}{k_1} \binom{l-l_1}{k_2} (-1)^{l-l_1+k_2} \big\langle (\hat{a}^\dagger)^{k_1+k_2}\, \hat{a}^m \big\rangle \big\langle \hat{V}_1^{l_1-k_1} \big\rangle \big\langle \hat{V}_2^{l-l_1-k_2} \big\rangle \\
&- \sum_{k_1=0}^{l_1-1} \binom{l_1}{k_1} \big\langle (\hat{a}^\dagger)^{k_1+l-l_1}\, \hat{a}^m \big\rangle \big\langle \hat{V}_1^{l_1-k_1} \big\rangle ,
\end{aligned}
\tag{D.1}
$$

where $l, m, l_1, m_1 \in \mathbb{N}_0$.

The noise moments for both chains are

$$
\begin{aligned}
&\big\langle \hat{V}_1^r(\hat{V}_1^\dagger)^s\big\rangle = \big\langle(\hat{S}_1^\dagger)^r\hat{S}_1^s\big\rangle - \\
&\sum_{k_1=0}^{r}\sum_{j_1=0}^{s-1}\sum_{k_1'=0}^{r-k_1}\sum_{j_1'=0}^{s-j_1}\binom{r}{k_1}\binom{s}{j_1}\binom{r-k_1}{k_1'}\binom{s-j_1}{j_1'}\big\langle(\hat{a}^\dagger)^{k_1'}\,\hat{a}^{j_1'}\big\rangle\big\langle(\hat{v}^\dagger)^{r-k_1-k_1'}\,\hat{v}^{s-j_1-j_1'}\big\rangle\big\langle\hat{V}_1^{k_1}(\hat{V}_1^\dagger)^{j_1}\big\rangle \\
&-\sum_{k_1=0}^{r-1}\binom{r}{k_1}\big\langle(\hat{a}^\dagger)^{r-k_1}\big\rangle\big\langle\hat{V}_1^{k_1}(\hat{V}_1^\dagger)^s\big\rangle, \qquad \text{(D.2)}\\
&\big\langle \hat{V}_2^r(\hat{V}_2^\dagger)^s\big\rangle = \big\langle(\hat{S}_2^\dagger)^r\hat{S}_2^s\big\rangle - \\
&\sum_{k_1=0}^{r}\sum_{j_1=0}^{s-1}\sum_{k_1'=0}^{r-k_1}\sum_{j_1'=0}^{s-j_1}\binom{r}{k_1}\binom{s}{j_1}\binom{r-k_1}{k_1'}\binom{s-j_1}{j_1'}(-1)^{k_1'+j_1'}\big\langle(\hat{a}^\dagger)^{k_1'}\,\hat{a}^{j_1'}\big\rangle\big\langle(\hat{v}^\dagger)^{r-k_1-k_1'}\,\hat{v}^{s-j_1-j_1'}\big\rangle\times \\
&\big\langle\hat{V}_2^{k_1}(\hat{V}_2^\dagger)^{j_1}\big\rangle-\sum_{k_1=0}^{r-1}\binom{r}{k_1}(-1)^{r-k_1}\big\langle(\hat{a}^\dagger)^{r-k_1}\big\rangle\big\langle\hat{V}_2^{k_1}(\hat{V}_2^\dagger)^s\big\rangle\,, \qquad \text{(D.3)}
\end{aligned}
$$

where $r+s>1$ and $r,s\in\mathbb{N}_0$.

The squeezing below the vacuum in decibel is written as

$$
\begin{aligned}
\mathcal{S} = -10\log_{10}\big(&-\langle\hat{a}^2\rangle\mathrm{e}^{-i\phi}-\langle(\hat{a}^\dagger)^2\rangle\mathrm{e}^{i\phi}+2\langle\hat{a}^\dagger\hat{a}\rangle+1\\
&+\langle\hat{a}\rangle^2\mathrm{e}^{-i\phi}+\langle\hat{a}^\dagger\rangle^2\mathrm{e}^{i\phi}-2\langle\hat{a}^\dagger\rangle\langle\hat{a}\rangle\big)\,. \qquad \text{(D.4)}
\end{aligned}
$$

Here, the angle ϕ is defined via the relation $\langle\hat{a}^2\rangle-\langle\hat{a}\rangle^2=|\langle\hat{a}^2\rangle-\langle\hat{a}\rangle^2|\mathrm{e}^{i\phi}$. The argument of the logarithm is the ratio between the variance of the squeezed quadrature and the vacuum variance, $(\Delta X_{\mathrm{sq}})^2/0.25$.

In the case of infinitely many reconstructed moments $\langle(\hat{a}^\dagger)^l\hat{a}^m\rangle$, the Wigner function $W(q,p)$ of an arbitrary state can be completely reconstructed. For Gaussian states, we are allowed to restrict ourselves to moments with $l+m\leq 2$. This enables us to use an analytical approach [100, 101], which yields

$$
\begin{aligned}
&W(q,p)=\\
&\frac{1}{\pi\sqrt{(\nu+1/2)^2-|\mu|^2}}\exp\left[-\frac{(\nu+1/2)|\zeta-\langle\hat{a}\rangle|^2-(\mu^*/2)(\zeta-\langle\hat{a}\rangle)^2-(\mu/2)(\zeta^*-\langle\hat{a}^\dagger\rangle)^2}{(\nu+1/2)^2-|\mu|^2}\right], \qquad \text{(D.5)}
\end{aligned}
$$

with $\zeta\equiv q+ip$, $\mu\equiv\langle\hat{a}^2\rangle-\langle\hat{a}\rangle^2$, and $\nu\equiv\langle\hat{a}^\dagger\hat{a}\rangle-|\langle\hat{a}\rangle|^2$.

Appendix E

Negativity

The discussions in this section are based on the supplementary material from Ref. [39]. For a bipartite system, the amount of entanglement between the subsystems A and B can be quantified by means of the negativity

$$\mathcal{N}(\rho) \equiv \frac{||\rho^{T_B}||_1 - 1}{2}, \tag{E.1}$$

where ρ is the density matrix of the total system, and $||\rho^{T_B}||_1 = Tr|\rho^{T_B}|$ is the trace norm of the partial transpose of ρ with respect to subsystem B, ρ^{T_B}. If $\mathcal{N}(\rho) > 0$, the state is entangled. For a maximally entangled state, $\mathcal{N}(\rho) \to \infty$.

In the case of Gaussian states, all measures of entanglement are equivalent, and they are defined by the covariance matrix

$$\boldsymbol{\sigma} = \begin{pmatrix} \boldsymbol{\alpha} & \boldsymbol{\gamma} \\ \boldsymbol{\gamma}^T & \boldsymbol{\beta} \end{pmatrix}. \tag{E.2}$$

Annihilation and creation operators, $s_{1,2}$ and $s_{1,2}^\dagger$, are used to represent the two subsystems. We define the matrices

$$\boldsymbol{\alpha} \equiv \begin{pmatrix} \alpha_1 & \alpha_3 \\ \alpha_3 & \alpha_2 \end{pmatrix}, \boldsymbol{\beta} \equiv \begin{pmatrix} \beta_1 & \beta_3 \\ \beta_3 & \beta_2 \end{pmatrix}, \boldsymbol{\gamma} \equiv \begin{pmatrix} \gamma_{11} & \gamma_{12} \\ \gamma_{21} & \gamma_{22} \end{pmatrix} \tag{E.3}$$

with

$$\alpha_1 = \langle \hat{s}_1^2 \rangle + \langle (\hat{s}_1^\dagger)^2 \rangle + 2\langle \hat{s}_1^\dagger \hat{s}_1 \rangle - \langle \hat{s}_1 + \hat{s}_1^\dagger \rangle^2 + 1 \tag{E.4}$$

$$\alpha_2 = -\langle \hat{s}_1^2 \rangle - \langle (\hat{s}_1^\dagger)^2 \rangle + 2\langle \hat{s}_1^\dagger \hat{s}_1 \rangle + \langle \hat{s}_1 - \hat{s}_1^\dagger \rangle^2 + 1 \tag{E.5}$$

$$\alpha_3 = i\big(- \langle \hat{s}_1^2 \rangle + \langle (\hat{s}_1^\dagger)^2 \rangle + \langle \hat{s}_1 \rangle^2 - \langle \hat{s}_1^\dagger \rangle^2 \big) \tag{E.6}$$

$$\beta_1 = \langle \hat{s}_2^2 \rangle + \langle (\hat{s}_2^\dagger)^2 \rangle + 2\langle \hat{s}_2^\dagger \hat{s}_2 \rangle - \langle \hat{s}_2 + \hat{s}_2^\dagger \rangle^2 + 1 \tag{E.7}$$

$$\beta_2 = -\langle \hat{s}_2^2 \rangle - \langle (\hat{s}_2^\dagger)^2 \rangle + 2\langle \hat{s}_2^\dagger \hat{s}_2 \rangle + \langle \hat{s}_2 - \hat{s}_2^\dagger \rangle^2 + 1 \tag{E.8}$$

$$\beta_3 = i\big(- \langle \hat{s}_2^2 \rangle + \langle (\hat{s}_2^\dagger)^2 \rangle + \langle \hat{s}_2 \rangle^2 - \langle \hat{s}_2^\dagger \rangle^2 \big) \tag{E.9}$$

$$\begin{aligned}\gamma_{11} = &\langle \hat{s}_1 \hat{s}_2 + \hat{s}_1 \hat{s}_2^\dagger + \hat{s}_1^\dagger \hat{s}_2 + \hat{s}_1^\dagger \hat{s}_2^\dagger \rangle/2 \\ &+ \langle \hat{s}_2 \hat{s}_1 + \hat{s}_2 \hat{s}_1^\dagger + \hat{s}_2^\dagger \hat{s}_1 + \hat{s}_2^\dagger \hat{s}_1^\dagger \rangle/2 \\ &- \langle \hat{s}_1 + \hat{s}_1^\dagger \rangle \langle \hat{s}_2 + \hat{s}_2^\dagger \rangle \end{aligned} \tag{E.10}$$

$$\begin{aligned}\gamma_{12} = &\langle \hat{s}_1 \hat{s}_2 - \hat{s}_1 \hat{s}_2^\dagger + \hat{s}_1^\dagger \hat{s}_2 - \hat{s}_1^\dagger \hat{s}_2^\dagger \rangle/2i \\ &+ \langle \hat{s}_2 \hat{s}_1 + \hat{s}_2 \hat{s}_1^\dagger - \hat{s}_2^\dagger \hat{s}_1 - \hat{s}_2^\dagger \hat{s}_1^\dagger \rangle/2i \\ &+ i\langle \hat{s}_1 + \hat{s}_1^\dagger \rangle \langle \hat{s}_2 - \hat{s}_2^\dagger \rangle \end{aligned} \tag{E.11}$$

$$\begin{aligned}\gamma_{21} = &\langle \hat{s}_1 \hat{s}_2 + \hat{s}_1 \hat{s}_2^\dagger - \hat{s}_1^\dagger \hat{s}_2 - \hat{s}_1^\dagger \hat{s}_2^\dagger \rangle/2i \\ &+ \langle \hat{s}_2 \hat{s}_1 - \hat{s}_2 \hat{s}_1^\dagger + \hat{s}_2^\dagger \hat{s}_1 - \hat{s}_2^\dagger \hat{s}_1^\dagger \rangle/2i \\ &+ i\langle \hat{s}_1 - \hat{s}_1^\dagger \rangle \langle \hat{s}_2 + \hat{s}_2^\dagger \rangle \end{aligned} \tag{E.12}$$

$$\begin{aligned}\gamma_{22} = &\langle -\hat{s}_1 \hat{s}_2 + \hat{s}_1 \hat{s}_2^\dagger + \hat{s}_1^\dagger \hat{s}_2 - \hat{s}_1^\dagger \hat{s}_2^\dagger \rangle/2 \\ &+ \langle -\hat{s}_2 \hat{s}_1 + \hat{s}_2 \hat{s}_1^\dagger + \hat{s}_2^\dagger \hat{s}_1 - \hat{s}_2^\dagger \hat{s}_1^\dagger \rangle/2 \\ &+ \langle \hat{s}_1 - \hat{s}_1^\dagger \rangle \langle \hat{s}_2 - \hat{s}_2^\dagger \rangle \end{aligned} \tag{E.13}$$

and $\boldsymbol{\gamma}^T$ being the transpose of $\boldsymbol{\gamma}$. Finally, the negativity becomes [102]

$$\mathcal{N} = \max\left\{0, \frac{1-\nu}{2\nu}\right\} \equiv \max\left\{0, \tilde{\mathcal{N}}\right\}, \tag{E.14}$$

where $\nu \equiv \sqrt{\left(\Delta(\boldsymbol{\sigma}) - \sqrt{\Delta^2(\boldsymbol{\sigma}) - 4\det\boldsymbol{\sigma}}\right)/2}$ and $\Delta(\boldsymbol{\sigma}) \equiv \det\boldsymbol{\alpha} + \det\boldsymbol{\beta} - 2\det\boldsymbol{\gamma}$. Note that, despite not being a measure, the negativity kernel $\tilde{\mathcal{N}}$ is a witness for arbitrary bipartite entanglement. In fact, if a non-Gaussian state has the same first and second moments as an entangled Gaussian state, it is entangled [103]. Consequently, $\tilde{\mathcal{N}} > 0$ implies entanglement for any bipartite state.

Bibliography

[1] D. Deutsch. Quantum theory, the Church-Turing principle and the universal quantum computer. *Proc. R. Soc. Lond. A* **400**, 97–117 (1985).

[2] D. Deutsch & R. Jozsa. Rapid solution of problems by quantum computation. *Proc. R. Soc. Lond. A* **439**, 553–558 (1992).

[3] P. W. Shor. Algorithms for quantum computation: discrete logarithms and factoring. *Proc. 37th Ann. Symp. on the Foundations of Comp. Sci. (FOCS)* 124–134 (1994).

[4] J. P. Gordon. Quantum effects in communications systems. *Proc. IRE* **50**, 1898–1908 (1962).

[5] D. S. Lebedev & L. B. Levitin. Information transmission by electromagnetic field. *Info. and Cont.* **9**, 1–22 (1966).

[6] M. A. Sillanpää, J. I. Park & R. W. Simmonds. Coherent quantum state storage and transfer between two phase qubits via a resonant cavity. *Nature* **449**, 438–442 (2007).

[7] J. I. Cirac, P. Zoller, H. J. Kimble & H. Mabuchi. Quantum state transfer and entanglement distribution among distant nodes in a quantum network. *Phys. Rev. Lett.* **78**, 3221–3224 (1997).

[8] C. H. Bennett, G. Brassard, C. Crépeau, R. Jozsa, A. Peres & W. K. Wootters. Teleporting an unknown quantum state via dual classical and Einstein-Podolsky-Rosen Channels. *Phys. Rev. Lett.* **70**, 1895–1899 (1993).

[9] A. Einstein, B. Podolsky & N. Rosen. Can quantum-mechanical description of physical reality be considered complete? *Phys. Rev.* **47**, 777–780 (1935).

[10] D. Bouwmeester, J.-W. Pan, K. Mattle, M. Eibl, H. Weinfurter & A. Zeilinger. Experimental quantum teleportation. *Nature* **390**, 575–579 (1997).

[11] D. Boschi, S. Branca, F. De Martini, L. Hardy & S. Popescu. Experimental realization of teleporting an unknown pure quantum state via dual classical and Einstein-Podolsky-Rosen channels. *Phys. Rev. Lett.* **80**, 1121–1125 (1998).

[12] L. Vaidman. Teleportation of quantum states. *Phys. Rev. A* **49**, 1473–1476 (1994).

[13] S. L. Braunstein & H. J. Kimble. Teleportation of continuous quantum variables. *Phys. Rev. Lett.* **80**, 869–872 (1998).

[14] A. Furusawa, J. L. Sørensen, S. L. Braunstein, C. A. Fuchs, H. J. Kimble & E. S. Polzik. Unconditional quantum teleportation. *Science* **282**, 706–709 (1998).

[15] N. Lee, H. Benichi, Y. Takeno, S. Takeda, J. Webb, E. Huntington & A. Furusawa. Teleportation of nonclassical wave packets of light. *Science* **332**, 330–333 (2011).

[16] X.-M. Jin, J.-G. Ren, B. Yang, Z.-H. Yi, F. Zhou, X.-F. Xu, S.-K. Wang, D. Yang, Y.-F. Hu, S. Jiang, T. Yang, H. Yin, K. Chen, C.-Z. Peng & J.-W. Pan. Experimental free-space quantum teleportation. *Nature Phot.* **4**, 376–381 (2010).

[17] J. Yin, J.-G. Ren, H. Lu, Y. Cao, H.-L. Yong, Y.-P. Wu, C. Liu, S.-K. Liao, F. Zhou, Y. Jiang, X.-D. Cai, P. Xu, G.-S. Pan, J.-J. Jia, Y.-M. Huang, H. Yin, J.-Y. Wang, Y.-A. Chen, C.-Z. Peng & J.-W. Pan. Quantum teleportation and entanglement distribution over 100-kilometre free-space channels. *Nature* **488**, 185–188 (2012).

[18] X.-S. Ma, T. Herbst, T. Scheidl, D. Wang, S. Kropatschek, W. Naylor, B. Wittmann, A. Mech, J. Kofler, E. Anisimova, V. Makarov, T. Jennewein, R. Ursin & A. Zeilinger. Quantum teleportation over 143 kilometres using active feed-forward. *Nature* **489**, 269–273 (2012).

[19] A. Wallraff, D. I. Schuster, A. Blais, L. Frunzio, R.-S. Huang, J. Majer, S. Kumar, S. M. Girvin & R. J. Schoelkopf. Strong coupling of a single photon to a superconducting qubit using circuit quantum electrodynamics. *Nature* **431**, 162–167 (2004).

[20] A. Blais, R.-S. Huang, A. Wallraff, S. M. Girvin & R. J. Schoelkopf. Cavity quantum electrodynamics for superconducting electrical circuits: An architecture for quantum computation. *Phys. Rev. A* **69**, 062320 (2004).

[21] T. Niemczyk, F. Deppe, H. Huebl, E. P. Menzel, F. Hocke, M. J. Schwarz, J. J. Garcia-Ripoll, D. Zueco, T. Hümmer, E. Solano, A. Marx & R. Gross. Circuit quantum electrodynamics in the ultrastrong-coupling regime. *Nature Phys.* **6**, 772–776 (2010).

[22] C. M. Caves. Quantum limits on noise in linear amplifiers. *Phys. Rev. D* **26**, 1817–1839 (1982).

[23] A. A. Clerk, M. H. Devoret, S. M. Girvin, F. Marquardt & R. J. Schoelkopf. Introduction to quantum noise, measurement, and amplification. *Rev. Mod. Phys.* **82**, 1155–1208 (2010).

[24] B. Yurke, L. W. Rupp & P. G. Kaminsky. Use of the Josephson junction in fundamental quantum electronics experiments. *IEEE Trans. Magn.* **23**, 458–464 (1987).

[25] B. Yurke, L. R. Corruccini, P. G. Kaminisky, L. W. Rupp, A. D. Smith, A. H. Silver, R. W. Simon & E. A. Whittaker. Observation of parametric amplification and deamplification in a Josephson parametric amplifier. *Phys. Rev. A* **39**, 2519–2533 (1989).

[26] B. Yurke, M. L. Roukes, R. Movshovich & A. N. Pargellis. A low-noise series-array Josephson junction parametric amplifier. *Appl. Phys. Lett.* **69**, 3078–3080 (1996).

[27] E. A. Tholén, A. Ergül, E. M. Doherty, F. M. Weber, F. Grégis & D. B. Haviland. Nonlinearities and parametric amplification in superconducting coplanar waveguide resonators. *Appl. Phys. Lett.* **90**, 253509 (2007).

[28] M. A. Castellanos-Beltran & K. W. Lehnert. Widely tunable parametric amplifier based on a superconducting quantum interference device array resonator. *Appl. Phys. Lett.* **91**, 083509 (2007).

[29] M. A. Castellanos-Beltran, K. D. Irwin, G. C. Hilton, L. R. Vale & K. W. Lehnert. Amplification and squeezing of quantum noise with a tunable Josephson metamaterial. *Nature Phys.* **4**, 929–931 (2008).

[30] T. Yamamoto, K. Inomata, M. Watanabe, K. Matsuba, T. Miyazaki, W. D. Oliver, Y. Nakamura & J. S. Tsai. Flux-driven Josephson parametric amplifier. *Appl. Phys. Lett.* **93**, 042510 (2008).

[31] C. Eichler & A. Wallraff. Controlling the dynamic range of a Josephson parametric amplifier. *EPJ Quan. Tech.* **1**, 1–19 (2014).

[32] L. Zhong, E. P. Menzel, R. Di Candia, P. Eder, M. Ihmig, A. Baust, M. Haeberlein, E. Hoffmann, K. Inomata, T. Yamamoto, Y. Nakamura, E. Solano, F. Deppe, A. Marx & R. Gross. Squeezing with a flux-driven Josephson parametric amplifier. *New J. Phys.* **15**, 125013 (2013).

[33] I. Siddiqi, R. Vijay, F. Pierre, C. M. Wilson, M. Metcalfe, C. Rigetti, L. Frunzio & M. H. Devoret. RF-Driven Josephson bifurcation amplifier for quantum measurement. *Phys. Rev. Lett.* **93**, 207002 (2004).

[34] C. Eichler, Y. Salathe, J. Mlynek, S. Schmidt & A. Wallraff. Quantum-Limited amplification and entanglement in coupled nonlinear resonators. *Phys. Rev. Lett.* **113**, 110502 (2014).

[35] F. Mallet, M. A. Castellanos-Beltran, H. S. Ku, S. Glancy, E. Knill, K. D. Irwin, G. C. Hilton, L. R. Vale & K. W. Lehnert. Quantum state tomography of an itinerant squeezed microwave field. *Phys. Rev. Lett.* **106**, 220502 (2011).

[36] C. Eichler, D. Bozyigit, C. Lang, M. Baur, L. Steffen, J. M. Fink, S. Filipp & A. Wallraff. Observation of two-mode squeezing in the microwave frequency domain. *Phys. Rev. Lett.* **107**, 113601 (2011).

[37] R. Movshovich, B. Yurke, P. G. Kaminsky, A. D. Smith, A. H. Silver, R. W. Simon & M. V. Schneider. Observation of zero-point noise squeezing via a Josephson-parametric amplifier. *Phys. Rev. Lett.* **65**, 1419–1422 (1990).

[38] L. Steffen, Y. Salathe, M. Oppliger, P. Kurpiers, M. Baur, C. Lang, C. Eichler, G. Puebla-Hellmann, A. Fedorov & A. Wallraff. Deterministic quantum teleportation with feed-forward in a solid state system. *Nature* **500**, 319–322 (2013).

[39] E. P. Menzel, R. Di Candia, F. Deppe, P. Eder, L. Zhong, M. Ihmig, M. Haeberlein, A. Baust, E. Hoffmann, D. Ballester, K. Inomata, T. Yamamoto, Y. Nakamura, E. Solano, A. Marx & R. Gross. Path entanglement of continuous-variable quantum microwaves. *Phys. Rev. Lett.* **109**, 250502 (2012).

[40] E. P. Menzel. *Propagating quantum microwaves: dual-path state reconstruction and path entanglement*. Phd thesis, Technische Universität München (2013). URL `http://www.wmi.badw.de/publications/theses/Menzel_Doktorarbeit_2013.pdf`.

[41] E. P. Menzel, F. Deppe, M. Mariantoni, M. Á. Araque Caballero, A. Baust, T. Niemczyk, E. Hoffmann, A. Marx, E. Solano & R. Gross. Dual-path state reconstruction scheme for propagating quantum microwaves and detector noise tomography. *Phys. Rev. Lett.* **105**, 100401 (2010).

[42] P. Eder. *Dual-path receiver for state reconstruction of propagating quantum microwaves*. Diploma thesis, Technische Universität München (2012). URL `http://www.wmi.badw-muenchen.de/publications/theses/Eder,Peter_Diplomarbeit_2012.pdf`.

[43] R. Di Candia, E. P. Menzel, L. Zhong, F. Deppe, A. Marx, R. Gross & E. Solano. Dual-path methods for propagating quantum microwaves. *New J. Phys.* **16**, 015001 (2014).

[44] D. M. Pozar. *Microwave Engineering* (John Wiley & Sons, Inc., New York, 2005).

[45] R. J. Glauber. Coherent and incoherent states of the radiation field. *Phys. Rev.* **131**, 2766–2788 (1963).

[46] E. C. G. Sudarshan. Equivalence of semiclassical and quantum mechanical descriptions of statistical light beams. *Phys. Rev. Lett.* **10**, 277–279 (1963).

[47] D. F. Walls & G. J. Milburn. *Quantum Optics* (Springer, Berlin, 2008).

[48] E. Wigner. On the quantum correction for thermodynamic equilibrium. *Phys. Rev.* **40**, 749–759 (1932).

[49] S. N. Filippov & V. I. Man'ko. Evolution of microwave quantum states in terms of measurable ordered moments of creation and annihilation operators. *Opt. Spectrosc.* **112**, 365–372 (2012).

[50] S. N. Filippov & V. I. Man'ko. Measuring microwave quantum states: Tomogram and moments. *Phys. Rev. A* **84**, 033827 (2011).

[51] A. Bednorz & W. Belzig. Fourth moments reveal the negativity of the Wigner function. *Phys. Rev. A* **83**, 052113 (2011).

[52] H. Weyl. *The theory of groups and quantum mechanics* (Courier Corporation, 1950).

[53] M. Hillery, R. F. O'Connell, M. O. Scully & E. P. Wigner. Distribution functions in physics: fundamentals. *Phys. Rep.* **106**, 121–167 (1984).

[54] M. G. A. Paris. Displacement operator by beam splitter. *Phys. Lett. A* **217**, 78–80 (1996).

[55] B. Yurke. Squeezed-state generation using a Josephson parametric amplifier. *J. Opt. Soc. Am. B* **4**, 1551–1557 (1987).

[56] L.-A. Wu, H. J. Kimble, J. L. Hall & H. Wu. Generation of squeezed states by parametric down conversion. *Phys. Rev. Lett.* **57**, 2520 (1986).

[57] R. Dong, J. Heersink, J. F. Corney, P. D. Drummond, U. L. Andersen & G. Leuchs. Experimental evidence for Raman-induced limits to efficient squeezing in optical fibers. *Opt. Lett.* **33**, 116–118 (2008).

[58] Z. Y. Ou, S. F. Pereira, H. J. Kimble & K. C. Peng. Realization of the Einstein-Podolsky-Rosen paradox for continuous variables. *Phys. Rev. Lett.* **68**, 3663–3666 (1992).

[59] R. E. Slusher, L. W. Hollberg, B. Yurke, J. C. Mertz & J. F. Valley. Observation of squeezed states generated by four-wave mixing in an optical cavity. *Phys. Rev. Lett.* **55**, 2409–2412 (1986).

[60] M. Schwarz. *Gradiometric tunable-gap flux qubits in a circuit QED architecture*. Phd thesis, Technische Universität München (2014). URL `http://www.wmi.badw.de/publications/theses/Schwarz,Manuel_Doktorarbeit.pdf`.

[61] G. J. Dolan. Offset masks for lift-off photoprocessing. *Appl. Phys. Lett.* **31**, 337–339 (1977).

[62] R. Gross & A. Marx. *Applied superconductivity: Josephson effect and Superconducting electronics*. Lecture notes, Technische Universität München (2005). URL `http://www.wmi.badw.de/teaching/Lecturenotes/AS/AS_Chapter3.pdf`.

[63] M. Wallquist, V. S. Shumeiko & G. Wendin. Selective coupling of superconducting charge qubits mediated by a tunable stripline cavity. *Phys. Rev. B* **74**, 224506 (2006).

[64] A. Baust. *Characterization of flux-driven Josephson parametric amplifiers.* Diploma thesis, Technische Universität München (2010). URL `http://www.wmi.badw-muenchen.de/publications/theses/Baust,Alexander_Diplomarbeit_2012.pdf`.

[65] S. M. Barnett & P. L. Knight. Squeezing in correlated quantum systems. *J. Mod. Opt .* **34**, 841–853 (1987).

[66] M. P. da Silva, D. Bozyigit, A. Wallraff & A. Blais. Schemes for the observation of photon correlation functions in circuit QED with linear detectors. *Phys. Rev. A* **82**, 043804 (2010).

[67] R. J. Glauber. Photon correlations. *Phys. Rev. Lett.* **10**, 84–86 (1963).

[68] D. Bozyigit, C. Lang, L. Steffen, J. M. Fink, C. Eichler, M. Baur, R. Bianchetti, P. J. Leek, S. Filipp, M. P. da Silva, A. Blais & A. Wallraff. Antibunching of microwave-frequency photons observed in correlation measurements using linear detectors. *Nature Phys.* **7**, 154–158 (2011).

[69] P. Van Loock, S. L. Braunstein & H. J. Kimble. Broadband teleportation. *Phys. Rev. A* **62**, 022309 (2000).

[70] H. Yonezawa, T. Aoki & A. Furusawa. Demonstration of a quantum teleportation network for continuous variables. *Nature* **431**, 430–433 (2004).

[71] M. Riebe, H. Häffner, C. F. Roos, W. Hänsel, J. Benhelm, G. P. T. Lancaster, T. W. Körber, C. Becher, F. Schmidt-Kaler, D. F. V. James & R. Blatt. Deterministic quantum teleportation with atoms. *Nature* **429**, 734–737 (2004).

[72] M. D. Barrett, J. Chiaverini, T. Schaetz, J. Britton, W. M. Itano, J. D. Jost, E. Knill, C. Langer, D. Leibfried, R. Ozeri & D. J. Wineland. Deterministic quantum teleportation of atomic qubits. *Nature* **429**, 737–739 (2004).

[73] S. Olmschenk, D. N. Matsukevich, P. Maunz, D. Hayes, L.-M. Duan & C. Monroe. Quantum teleportation between distant matter qubits. *Science* **323**, 486–489 (2009).

[74] R. Di Candia, K. G. Fedorov, L. Zhong, S. Felicetti, E. P. Menzel, M. Sanz, F. Deppe, A. Marx, R. Gross & E. Solano. Quantum teleportation of propagating quantum microwaves. *arXiv preprint arXiv:1506.06701* (2015). URL `http://arxiv.org/abs/1506.06701`.

[75] B. Schumacher & M. A. Nielsen. Quantum data processing and error correction. *Phys. Rev. A* **54**, 2629–2635 (1996).

[76] S. L. Braunstein, C. A. Fuchs & H. J. Kimble. Criteria for continuous-variable quantum teleportation. *J. Mod. Opt.* **47**, 267–278 (2000).

[77] C. H. Bennett, D. P. DiVincenzo, P. W. Shor, J. A. Smolin, B. M. Terhal & W. K. Wootters. Remote state preparation. *Phys. Rev. Lett.* **87**, 077902 (2002).

[78] A. K. Pati. Minimum classical bit for remote preparation and measurement of a qubit. *Phys. Rev. A* **63**, 014302 (2000).

[79] Z. Kurucz, P. Adam, Z. Kis & J. Janszky. Continuous variable remote state preparation. *Phys. Rev. A* **72**, 052315 (2005).

[80] Z. Kurucz, P. Adam & J. Janszky. Remote state preparation in quadrature basis. *Quantum Elec.* **26**, 319–326 (2006).

[81] M. G. A. Paris, M. Cola & R. Bonifacio. Remote state preparation and teleportation in phase space. *J. Opt. B: Quantum Semiclass. Opt.* **5**, S360–S364 (2003).

[82] A. Marx, J. Hoess & K. Uhlig. Dry dilution refrigerator for experiments on quantum effects in the microwave regime. *arXiv preprint arXiv:1412.3619* (2014). URL `http://arxiv.org/abs/1412.3619`.

[83] K. Uhlig. Dry dilution refrigerator with He-4 precool loop. *arXiv preprint arXiv:1412.3665* (2014). URL `http://arxiv.org/abs/1412.3665`.

[84] E. Hoffmann, F. Deppe, T. Niemczyk, T. Wirth, E. P. Menzel, G. Wild, H. Huebl, M. Mariantoni, T. Weißl, A. Lukashenko, A. P. Zhuravel, A. V. Ustinov, A. Marx & R. Gross. A superconducting 180° hybrid ring coupler for circuit quantum electrodynamics. *Appl. Phys. Lett.* **97**, 222508 (2010).

[85] R. Schack & A. Schenzle. Moment hierarchies and cumulants in quantum optics. *Phys. Rev. A* **41**, 3847–3852 (1990).

[86] L.-Z. Jiang. The cumulants of bosonic quantum states. *Proc. SPIE* **7846**, 784612 (2010).

[87] S. Sabah & R. Lorenz. Design and calibration of IQ-mixers. *EPAC* **98**, 1589–1591 (1998). URL `https://accelconf.web.cern.ch/AccelConf/e98/PAPERS/WEP09A.PDF`.

[88] J. Fischer. *High-precision phase stabilization between microwave generators.* Bachelor thesis, Technische Universität München (2014). URL `http://www.wmi.badw.de/publications/theses/Fischer,Johanna%20Bachelor%20Thesis%202014.pdf`.

[89] S. Butz, A. K. Feofanov, K. G. Fedorov, H. Rotzinger, A. U. Thomann, B. Mackrodt, R. Dolata, V. B. Geshkenbein, G. Blatter & A. V. Ustinov. Flux-dependent crossover between quantum and classical behavior in a dc SQUID. *Phys. Rev. Lett.* **113**, 247005 (2014).

[90] R. W. Boyd. *Nonlinear optics* (Academic press, 2008).

[91] R. Movshovich, B. Yurke, A. D. Smith & A. H. Silver. Subharmonic pumping and noise properites of the Josephson parametric amplifier. *Springer Proc. Phys.* **64**, 415–418 (1992).

[92] F. X. Kaertner & P. Russer. Generation of squeezed microwave states by a dc-pumped degenerate parametric Josephson junction oscillator. *Phys. Rev. A* **42**, 5601–5612 (1990).

[93] V. E. Manucharyan, E. Boaknin, M. Metcalfe, R. Vijay, I. Siddiqi & M. Devoret. Microwave bifurcation of a Josephson junction: Embedding-circuit requirements. *Phys. Rev. B* **76**, 014524 (2007).

[94] K. Wiesenfeld & B. McNamara. Small-signal amplification in bifurcating dynamical systems. *Phys. Rev. A* **33**, 629–642 (1986).

[95] C. M. Wilson, T. Duty, M. Sandberg, F. Persson, V. Shumeiko & P. Delsing. Photon generation in an electromagnetic cavity with a time-dependent boundary. *Phys. Rev. Lett.* **105**, 233907 (2010).

[96] N. F. Pedersen, O. H. Soerensen, B. Dueholm & J. Mygind. Half-harmonic parametric oscillations in Josephson junctions. *J. Low Temp. Phys* **38**, 1–23 (1980).

[97] H. B. Callen & T. A. Welton. Irreversibility and generalized noise. *Phys. Rev.* **83**, 34–40 (1951).

[98] M. O. Scully & M. S. Zubairy. *Quantum optics* (Cambridge University Press, Cambridge, 1997).

[99] X. Zhou, V. Schmitt, P. Bertet, D. Vion, W. Wustmann, V. Shumeiko & D. Esteve. High-gain weakly nonlinear flux-modulated Josephson parametric amplifier using a SQUID array. *Phys. Rev. B* **89**, 214517 (2014).

[100] V. Bužek, G. Adam & G. Drobný. Quantum state reconstruction and detection of quantum coherences on different observation levels. *Phys. Rev. A* **54**, 804–820 (1996).

[101] V. Bužek, G. Adam & G. Drobný. Reconstruction of Wigner functions on different observation levels. *Ann. Phys.* **245**, 37–97 (1996).

[102] G. Adesso & F. Illuminati. Gaussian measures of entanglement versus negativities: Ordering of two-mode Gaussian states. *Phys. Rev. A* **72**, 032334 (2005).

[103] P. Hyllus & J. Eisert. Optimal entanglement witnesses for continuous-variable systems. *New J. Phys.* **8**, 51 (2006).

List of publications

- R. Di Candia, K. G. Fedorov, **L. Zhong**, S. Felicetti, E. P. Menzel, M. Sanz, F. Deppe, A. Marx, R. Gross, E. Solano, *Quantum Teleportation of Propagating Quantum Microwaves*, arXiv:1506.06701, submitted for publication (2015)
- A. Baust, E. Hoffmann, M. Haeberlein, M. J. Schwarz, P. Eder, J. Goetz, F. Wulschner, E. Xie, **L. Zhong**, F. Quijandría, B. Peropadre, D. Zueco, J.-J. García Ripoll, E. Solano, K. Fedorov, E. P. Menzel, F. Deppe, A. Marx, and R. Gross, *Tunable and Switchable Coupling Between Two Superconducting Resonators*, Phys. Rev. B **91**, 014515 (2015)
- A. Baust, E. Hoffmann, M. Haeberlein, M. J. Schwarz, P. Eder, J. Goetz, F. Wulschner, E. Xie, **L. Zhong**, F. Quijandría, D. Zueco, J.-J. García Ripoll, L. García-Álvarez, G. Romero, E. Solano, K. G. Fedorov, E. P. Menzel, F. Deppe, A. Marx, and R. Gross, *Ultrastrong Coupling in Two-Resonator Circuit QED*, arXiv:1412.7372, submitted for publication (2014)
- R. Di Candia, E. P. Menzel, **L. Zhong**, F. Deppe, A. Marx, R. Gross & E. Solano. *Dual-Path Methods for Propagating Quantum Microwaves*, New. J. Phys. **16**, 015001 (2014)
- **L. Zhong**, E. P. Menzel, R. Di Candia, P. Eder, M. Ihmig, A. Baust, M. Haeberlein, E. Hoffmann, K. Inomata, T. Yamamoto, Y. Nakamura, E. Solano, F. Deppe, A. Marx, and R. Gross, *Squeezing With a Flux-driven Josephson Parametric Amplifier*, New. J. Phys. **15**, 125013 (2013)
- E. P. Menzel, R. Di Candia, F. Deppe, P. Eder, **L. Zhong**, M. Ihmig, M. Haeberlein, A. Baust, E. Hoffmann, D. Ballester, K. Inomata, T. Yamamoto, Y. Nakamura, E. Solano, A. Marx, and R. Gross, *Path Entanglement of Continuous-Variable Quantum Microwaves*, Phys. Rev. Lett. **109**, 250502 (2012)

Acknowledgement

This thesis is the product of the work done not only by the author, but by a large number of colleagues. I would like to sincerely thank everyone for the great help and support.

First, I would like to thank my advisor Prof. Dr. Rudolf Gross. Prof. Gross, I am grateful that you gave me this valuable opportunity to work on this project and get to know this research area. You have been constant source of encouragement for me to overcome all the obstacles during my PhD life. Although you had very tight schedule everyday, you were always happy to discuss about my research progress, difficulties, future plans, etc. I will never forget your kindness, friendliness, and you research attitude as an institute director and a scientist.

Also, I want to thank my supervisors Dr. Achim Marx, Dr. Frank Deppe, and Dr. Kirill Fedorov. Achim, and Frank, thank you for the supervision and assistant in all my PhD life. Thank you for the help with any kind of scientific questions, and also the problems in daily life, such as housing, visa, etc. With such friendly, helpful and enthusiastic supervisors as you, my stay at WMI became very comfortable and joyful. Kirill, thank you for the great support in the last two years of my PhD life. You were always available to listen to any complain, discuss about any problem, and give suggestions. You helped me to sort out a lot of technical details and theoretical obstacles. You crazy ideals and enthusiasm for research inspired me.

I can not forget the supervision and support from Dr. Edwin Menzel. Edwin, first thanks for introducing me to microwave techniques and getting me involved in this project. Whenever I had any problem in the night or on the weekend, you were always available at the institute or on the phone to help. Your attitude and methods of doing research influenced me.

In addition, I am grateful for the work have been done by two master students, Stefan Pogorzalek and Martin Betzenbichler. Stefan, thank you for the great Labview programs, Matlab codes, simulations and measurements. Thank you for the useful discussions and ideas. Thank you for understanding my “half a sentence”. Martin, your contribution to the fridge work is valuable for this project. I wish you good luck with your future careers.

One person I can not afford to forget is Roberto Di Candia, our theoretical support. Whenever I had any theoretical question, you were always on gmail or Skype to answer my questions. During my visits to Bilbao, I was very happy to sit next to you and to ask questions at any time. Of course, I will not forget the wonderful party evening with you, Simone and other friends, and the Chinese new year day in Bilbao. Also, Prof. Dr. Enrique Solano, thanks for your hospitality, which made my stays in Bilbao very enjoyable.

The JPA samples, which have been the key ingredients in this work, have been provided by our Japanese collaborators, Tsuyoshi Yamamoto, Kunihiro Inomata and Prof. Yasunobu Nakamura. I was really glad to meet you in the APS meeting. Thank you for the nice JPA samples, the fruitful discussions in Baltimore and the numerous communications via email.

I want to thank all the members of qubit group. Dr. Alexander Baust, Dr. Elisabeth Hoffmann, Max Haeberlein, your introduction to sample fabrication, measurement techniques and cryogenics has been very helpful for my PhD research. Your help with writing German letters, making phone calls, and translating German documents made my stay in Munich much easier. Dr. Manuel Schwarz, Peter Eder, Friedrich Wulschner, Jan Goetz, Edwar Xie, Michael Fischer, Dr. Hans Huebl, etc. I am grateful for interesting discussions, friendly working atmosphere and funny barbecue time.

Thanks also to my office colleagues Michael Kunz, Toni Helm and Thomas Böhm. Without you help with translations, probably I needed to type the lengthy documents by hand in order to understand them. I am thankful for your kindness, for the interesting discussions on non-scientific topics, and for the board games on the weekend. Michael, special thanks to your father for the delicious lunch.

Ms. Emel Dönertas and Mr. Ludwig Ossiander deserve a special thank for the help with administrative tasks and all the tiny things in my daily life, such as health insurance, bank account, etc. Whatever kind of problems, you were always trying to help me to sort out.

Matthias Opel, Thomas Brenninger and Dieter Guratzsch, thank you for the technical support with computers and equipments. Also the great workshop team deserves a special mention. I am thankful for your patience to understand my bad German, and your suggestions for the design of sample boxes, sample holders, etc.

Sybilla Plöderl and Maria Botta, small conversations with you made my life at WMI much more interesting. Thanks you for keeping the institute clean and in order. Thanks for your patience to teach me German.

I want to thank all the members of WMI for the nice and friendly working atmosphere.

I was very lucky to join this CCQED network and got to know the CCQED fellows. I am grateful for the help from Maria Bernard-Schwarz with Labviews. I will always remember the CCQED fellows' days, the fellows' workshops, the weeks we spent together, the scientific and non-scientific discussions.

Finally, I must thank my friends and my family. The friendship gave me a lot of happiness. I am grateful for the love from my family, my parents, my grandparents, etc. Although during my PhD life, there were hundreds of kilometers between us, the love and support from you were always there. You gave me power, courage and motivation for today and for the future.